



AGH UNIVERSITY OF SCIENCE AND TECHNOLOGY

FIELD OF SCIENCE: Natural sciences

SCIENTIFIC DISCIPLINE: Physical sciences

DOCTORAL THESIS

Towards first observation of the $B_s^0 \rightarrow D_s^{*\mp} K^{*\pm}$ decay
and calibration of the Upstream Tracker detector.

Author: Wojciech Artur Krupa

First supervisor: dr hab. inż. Tomasz Szumlak - prof. AGH

Assisting supervisor: dr hab. inż. Agnieszka Obłąkowska-Mucha - prof. AGH

Completed in: AGH University of Science and Technology, Department of
Particle Interactions and Detection Techniques, Krakow, 2022

Declaration of the author of this dissertation

Aware of legal responsibility for making untrue statements I hereby declare that I have written this dissertation myself and all the contents of the dissertation have been obtained by legal means.

signature date

Declaration of the thesis Supervisors

This dissertation is ready to be reviewed.

signature of thesis Supervisor date

signature of assistant thesis Supervisor date

Contents

Streszczenie	5
Abstract	7
Acknowledgements	9
Author's contribution	10
1 Introduction	13
1.1 The Standard Model	13
1.2 The CKM matrix	18
1.3 Limitation of the Standard Model	18
1.4 CPV	19
1.4.1 The Gronau, London and Wyler method	22
1.4.2 The Atwood, Dunietz and Soni method	25
1.4.3 The Giri, Grossman, Soffer, and Zupan method	26
1.4.4 Time-dependent method	26
1.5 Motivation for searching for new $B \rightarrow DK$ channels	27
2 LHCb experiment	28
2.1 CERN	28
2.2 LHC	29
2.3 Description of LHCb detector	33
2.3.1 LHC and LHCb performance	34
2.3.2 LHCb's subsystems	36
2.3.3 Modernisation of tracking system during LS2	47
3 Upstream Tracker	52
3.1 Motivation and requirements	52
3.2 SALT	54
3.3 Stave	54
3.4 Sensor	56
3.5 Hybrid	57

3.6	Stave cooling system	58
4	Monitoring and calibration of UT detector	60
4.1	Radiation damage	60
4.2	Gaudi framework	61
4.3	General concept of monitoring and calibration software for UT	63
4.4	Introduction to Vetra package	63
4.5	Data signal processing	64
4.6	Vetra - UT package description	68
4.7	UT operation example	72
4.8	Interfaces for UT monitoring system	77
5	Analysis of $B_s^0 \rightarrow D_s^{*\mp} K^{*\pm}$ decay	84
5.1	Preliminary remarks	84
5.2	Introduction	84
5.3	Analysis strategy	86
5.4	Data samples	87
5.5	Simulated events	87
5.6	Selection	88
5.6.1	Stripping selection	89
5.6.2	Trigger selection	89
5.6.3	Offline Selection	89
5.7	Multivariate analysis	99
5.7.1	Introduction to MVA methods	99
5.7.2	Boosted Decision Tree	100
5.7.3	Multivariate analysis in $B_s^0 \rightarrow D_s^{*\mp} K^{*\pm}$ studies	101
5.7.4	Configuration of the algorithm and studies of matrices	102
5.8	Post-BDT studies	108
5.8.1	Studies of $D_s^{*\mp}$ and D_s^+	108
5.8.2	Studies of $K^{*\pm}$	111
5.9	Towards branching fraction measurement	114
6	Conclusions	119
6.1	Summary	119
6.2	Future outlook	120
A		121

Streszczenie

Badania zawarte w niniejszej pracy doktorskiej dotyczą dwóch obszarów badawczych: analizy rozpadu mezonu pięknego i rozwoju platformy do monitoringu i kalibracji jednego z detektorów śladowych. Prace wykonane zostały w ramach współpracy LHCb przy Wielkim Zderzaczu Hadronów - LHC.

Pierwsza część badań dotyczy selekcji rzadkiego i dotychczas nieobserwowanego rozpadu mezonu B_s^0 na dwa mezony wektorowe $D_s^{*\mp}$ i $K^{*\pm}$ w danych zebranych przez spektrometr LHCb w latach 2015-2018 (Run 2). Rozpad ten należy do rodziny rozpadów $B \rightarrow DK$, gdzie interferencja pomiędzy amplitudami przejść kwarkowych $b \rightarrow c$ i $b \rightarrow u$ zachodząca właśnie w tych rozpadach, umożliwia precyzyjne pomiary jednego z parametrów macierzy Cabibbo-Kobayashi-Maskawy (CKM) - kąta γ . Liczba spodziewanych przypadków rozpadu $B \rightarrow DK$ rejestrowanych w LHCb jest ograniczona niskim współczynnikiem rozgałęzienia tych rozpadów (rzędu 10^{-4} lub mniejszy) i koniecznością rekonstrukcji rezonansowych stanów pośrednich o bardzo krótkim czasie życia. Dodanie nowych procesów, jak np. omawiany $B_s^0 \rightarrow D_s^{*\mp} K^{*\pm}$, jest zatem korzystne i poprawi precyzję pomiaru. Skomplikowana topologia rozpadu $B_s^0 \rightarrow D_s^{*\mp} K^{*\pm}$ oraz duża (7) liczba stanów końcowych, zawierająca także cząstki neutralne, skutkuje bardzo małą spodziewaną liczbą obserwowanych przypadków rozpadu, która ukryta jest w ogromnej liczbie przypadków tła fizycznego i kombinatorycznego. Zadaniem badawczym było opracowanie kryteriów selekcji przypadków $B_s^0 \rightarrow D_s^{*\mp} K^{*\pm}$ z uwzględnieniem metod inteligencji obliczeniowej, w tym algorytmów takich jak BDT (Wzmocnione Drzewa Decyzyjne, ang. Boosted Decision Tree), a następnie zweryfikowanie ich skuteczności. Topologia rozpadu, skutkuje występowaniem szeregu stanów rezonansowych i pośrednich, które powinny zostać zaobserwowane i poddane analizie. Studia te poprzedzają dyskusję o kandydatach na kanał kontrolny, względem którego dokonywany jest pomiar współczynnika rozgałęzienia nieobserwowanego dotąd rozpadu.

Druga część pracy badawczej dotyczy rozwoju detektora UT (ang. Upstream Tracker),

który stanowi część układu rekonstrukcji śladów cząstek w zmodernizowanym detektorze LHCb. Częścią aktywną detektora są planarne sensory krzemowe. Detektor UT będzie mieć znaczący udział w rekonstrukcji śladów cząstek naładowanych w obszarze przed magnesem spektrometru i w wyznaczeniu wierzchołka produkcji i rozpadu cząstek długożyciowych, jak K_s^0 i Λ^0 . Sygnały z UT są także kluczowe dla systemu wyzwalania zapisu przypadku, który powinien w czasie rzeczywistym (ang. online) rekonstruować ślady z efektywnością bliską efektywności rekonstrukcji typu offline (wykonywanej już na przypadkach zapisanych na dyskach, używanej podczas Run 1 i 2 w latach 2010 - 2018). Zadaniem badawczym było opracowanie autonomicznej platformy - Vetra, mającej na celu kontrolę jakości danych rejestrowanych przez detektor i jego kalibrację. Platforma ta przetwarza dedykowany odczyt z detektora, w celu wyznaczenia parametrów opisujących jego stan, a także ma podejmować w sposób autonomiczny część decyzji dotyczących jego pracy. Dodatkowym elementem systemu, jest aplikacja Titania, która została rozwinięta w celu zapewnienia monitoringu dla detektora UT na podstawie parametrów pracy sensorów detektora UT, wyznaczonych przez Vetrę.

Abstract

The research covered in this dissertation addresses two areas: the analysis of the decay of beauty meson, B_s^0 , and the development of a platform for the monitoring and calibration of one of the tracking detectors. This work was carried out in cooperation with the LHCb collaboration.

The first part of the study concerns the selection of a rare and so far unobserved decay of the meson B_s^0 to two vector mesons $D_s^{*\mp}$ and $K^{*\pm}$ in data collected by the LHCb spectrometer in 2015-2018 (Run 2). This decay belongs to the $B \rightarrow DK$ decay family, where the interference between the amplitudes of the $b \rightarrow c$ and $b \rightarrow u$ quark transitions, which occur in these decays, allows precise measurements of one of the parameters of the Cabibbo-Kobayashi-Maskawa (CKM) matrix - the CKM angle γ . The low branching ratio (of the order of 10^{-4} or smaller) limits the number of expected $B \rightarrow DK$ decay events recorded at the LHCb. The introduction of new processes, such as the discussed $B_s^0 \rightarrow D_s^{*\mp} K^{*\pm}$, is therefore beneficial and will improve the precision of the measurement.

The complicated decay topology of $B_s^0 \rightarrow D_s^{*\mp} K^{*\pm}$ and the large (7) number of final states, including neutral particles, results in a very small expected number of observed decay events, which are hidden in the huge number of physical and combinatorial background events. The research task was to develop selection criteria for $B_s^0 \rightarrow D_s^{*\mp} K^{*\pm}$ candidates, including methods of computational intelligence, such as BDT (Boosted Decision Trees), which improve the separation of the decay events from the background and then verify their effectiveness. Decay dynamics, results in a number of resonance and intermediate states that should be observed and analysed. This study is followed by a discussion on candidates for the control channel, with respect to which the branching fraction of unobserved decay is measured.

The second part of the research work concerns the development of the software for the Upstream Tracker (UT) detector, which will be a part of the particle's tracks

reconstruction system in the upgraded LHCb detector (from 2022). The active part of the detector consists of silicon sensors. Its purpose is to reconstruct the tracks of charged particles before the LHCb dipole magnet and enables secondary vertices reconstruction of long-lived particles like K_s^0 and Λ^0 . This information is also crucial for the LHCb trigger system, which is expected to reconstruct particle's tracks in real-time (online) with an efficiency close to that of the offline type reconstruction (already performed on events stored on disks, this system was used during Run 1 and 2 in 2010 - 2018). The research task was to develop an autonomous platform, Vetra, to control the quality of the data recorded by the detector and its calibrations. This platform uses a dedicated RAW data stream to monitor the detector's status and, in future, make autonomous decisions regarding its operation. An additional component of the system, the Titania application was developed to provide monitoring for the UT detector based on the performance of the UT detector's sensors, determined by Vetra.

Acknowledgements

Serdecznie dziękuję Agnieszce Obłąkowskiej-Musze za wiedzę, którą mi cierpliwie przekazywała w czasie naszej wieloletniej współpracy, za jej stałą gotowość do pomocy, w szczególności przy pracy nad niniejszym opracowaniem.

Pragnę złożyć serdeczne podziękowania Promotorowi niniejszej pracy dr hab. Tomaszowi Szumlakowi za umożliwienie mi pracy w zespole LHCb-AGH oraz w CERNie, opiekę naukową i wszystkie cenne wskazówki.

Dziękuję kolegom z zespołu, Bartkowi, Karolowi, Maćkowi, Adamowi i Mateuszowi a w szczególności Pawłowi, z którym przeszedłem przez te 5 lat doktoratu.

Dziękuję Bartłomiejowi Rzeszotarskiemu za inspiracje i impulsy do działania, Mateuszowi Kowalskiemu za czas wspólnie spędzony w CERNie oraz poza nim, a także Annie Zarzeckiej za wspólne przewyżczanie problemów związanych ze studiami doktorskimi.

Dziękuję moim nauczycielom fizyki, Pani Barbarze Dzierżak oraz Panu Zbigniewowi Pigule, za rozpoczęcie przygody z fizyką.

Dziękuję przyjaciołom (a w szczególności Michałowi, Emilii, Paulinie i Wiktorowi), pracownikom KOiDC AGH i WFiIS AGH i całej społeczności WCS.

Na końcu chciałbym podziękować moim rodzicom, siostrze i dziadkom. Tylko dzięki Waszemu wsparciu wszystko to było możliwe.

Author's contribution

The author was the principal investigator of the following projects funded by the National Science Centre (NCN) in Poland:

- *First observation of the $B_s^0 \rightarrow D_s^{*+} K^{*-}$ decay and calibration of the Upstream Tracker detector*, project number: 2020/36/T/ST2/00168, project type: ETIUDA 8, the amount awarded: 106 632 PLN, project start date: 15 August 2020, project end date: 01 January 2023, ongoing project;
- *Innovative application of computational intelligence techniques for analysis of the $B_s^0 \rightarrow D_s^{*+} K^{*-}$ decay and autonomous data quality monitoring for silicon UT tracker of the upgraded LHCb experiment*, project number: 2018/31/N/ST2/01471, project type: PRELUDIUM 16, the amount awarded: 85 400 PLN, project start date: 26 July 2019, project end date: 25 April 2023, ongoing project.

Talks given by the author and posters presented at the international and national conferences:

- W. Krupa (et al. LHCb), *Selected results on the CKM angle γ measurement at LHCb*, 2nd Jagiellonian Symposium on Fundamental and Applied Subatomic Physics, Krakow, Poland, 4–9, July 2017, poster;
- W. Krupa (et al. LHCb), *Analysis of multibody beauty to open-charm decays at LHCb*, XXIV Cracow Epiphany Conference on Advances in Heavy Flavour Physics, Krakow, Poland, 9-12, January 2018, talk;
- W. Krupa (et al. LHCb), *Measurements of CPV in b and c decays at LHC*, QCD18 - 21th High-Energy Physics International Conference in Quantum Chromodynamics, Montpellier, France, 02-06, July 2018, talk, plenary;

- W. Krupa (et al. LHCb), *Recent results on the CKM angle γ measurement at LHCb and prospect for Run III and IV*, 3rd Jagiellonian Symposium on Fundamental and Applied Subatomic Physics, Krakow, Poland, 23-28, June 2019, poster;
- W. Krupa (et al. LHCb), *Beauty to open charm final states at LHCb*, video, ICHEP 2020, 40th International Conference on High Energy Physics, Prague, Czech Republic, 06-08, August 2020, talk, virtual;
- W. Krupa (et al. LHCb), *Recent results of measurement of CKM angle γ and CPV in the beauty sector at LHCb*, 19th International Conference on Hadron Spectroscopy and Structure in memoriam Simon Eidelman, 26-21, July 2021, talk, virtual;
- W. Krupa (et al. LHCb), *Measurements of the CKM angle γ at LHCb*, XIV International Conference on Beauty, Charm and Hyperon Hadrons, 5-11, June 2022, Kraków, Poland, talk, plenary;
- K. Sowa, W. Krupa, *Multiplication of simulated events using Machine Learning Technique*, XIV International Conference on Beauty, Charm and Hyperon Hadrons, 5-11 June 2022, Kraków, Poland, poster.

As a member of the LHCb collaboration, the author published the following proceedings:

- W. Krupa (et al. LHCb) *Selected results on the CKM angle γ measurement at LHCb*, Acta Phys. Pol. B, 48 (2017) 1989;
- W. Krupa (et al. LHCb) *Analysis of Multibody Beauty to Open-charm Decays at LHCb*, Acta Phys. Pol. B, 49 (2018) 1177-1183;
- P. Kopciwicz, T. Szumlak, W. Krupa (et al. LHCb) *Software Platform for the Monitoring and Calibration of the LHCb Upgrade I Silicon Detectors*, Acta Phys. Pol. B, 50, (2019);
- W. Krupa (et al. LHCb) *Recent results of the CKM angle γ measurement at the LHCb and prospects for Run III and Run IV*, Acta Phys. Pol. B, 51, 351 (2020);
- W. Krupa (et al. LHCb) *Measurements of CPV in b and c decays at LHC*, Nuclear and Particle Physics Proceedings(2018) 300-302, 145-152;

- M. Majewski, T. Szumlak, J. Kowalski, D. Wadowski, P. Kopciewicz, W. Krupa
Calibration software platform for LHCb upgrade silicon detectors: STORCK and TITANIA, Technical Note, CERN-LHCb-PUB-2021-007, (2021).

Important seminar talk :

- Measurements of the CKM angle γ at LHCb, 19 January 2017, Faculty of Physics and Applied Computer Science, AGH University of Science and Technology, Kraków, Poland.

Participation in important schools:

- 41st CERN School of Computing (CSC 2018), 1-14, October, 2018, Tel Aviv University, Tel Aviv, Israel;
- 7th Summer School on Machine Learning in High Energy Physics (MLHEP 2021), July 15-30, 2021, Online.

Other important activities (including international cooperations):

- The University of Cincinnati mentoring programme, *Development of software for UT detector*, supervision of two graduate students, coordinators: Tomasz Szumlak PhD (AGH), Michael Sokoloff PhD (UoC), January-October 2021;
- XIV International Conference on Beauty, Charm and Hyperon Hadrons, 5-11, June 2022, Kraków, Poland, Organising Committee;
- Krakow Applied Physics and Computer Science Summer School (2020, 2021), June-August, Organising Committee, Lecturer, Tutor.

Additionally, the author contributed to the LHCb collaboration in the following activities:

- UT testbeam (2016-2017), early tests of UT components on SPS at CERN;
- Commissioning of the UT detector (2021-ongoing), installation of A frame of UT detector and work on software for monitoring and calibration of the detector;
- Shift leader (2022), Data Quality Computing Simulation shifter (2022), Data Quality shifter (2018), Data Manager (2017, 2018), supervision of the LHCb spectrometer during commissioning and data taking.

Chapter 1

Introduction

The chapter provides a short overview of physical background related to the topic of studies on CP violation in the beauty and charm sector and basics principles of the Standard Model of particles.

1.1 The Standard Model

The Standard Model (SM), which was developed over a few decades of twentieth century, is based on the quantum field theory and is parameterised under the local gauge symmetry $SU(3)_C \times SU(2)_L \times U(1)_Y$ ¹.

The SM of particle physics is the theory that describes the fundamental particles called fermions, bosons and their interactions. The SM describes three of the four fundamental forces:

- The electromagnetic force - is responsible for interaction between electrically charged particles. The weak force and electromagnetic force are unified as a single electroweak force at high energy scales. The messenger of the electromagnetic interaction is the photon;
- The weak force - is responsible for decays of unstable nuclei through the transition of a neutron into proton, electron and neutrinos as well as other particles: pions, beauty and charm mesons and others. The messenger of the weak interaction is the W^\pm/Z^0 boson;

¹This overall symmetry pertains to the interactions without accounting for the spontaneous symmetry breaking leading to massive vector intermediate bosons and BEH mechanism.

- The strong force - binds quarks in hadrons and the protons and neutrons in nuclei. It is a strong, attractive source at short distances that overcome electric repulsion caused by the same charge of protons and some quarks. The messenger of strong interaction is gluon which carries a colour charge.

The SM describes 12 fermions which are grouped into three families (generations). Each group contain an up- and a down-type quark (Fig. 1.1). Particles from the first group have been known to humankind for the longest time. Protons and neutrons are made from quarks from the first generation and, together with electrons from the first generation of leptons, form atoms. Additionally, all known fermions have antimatter counterparts. Quarks take part in all known interactions (Fig. 1.2).

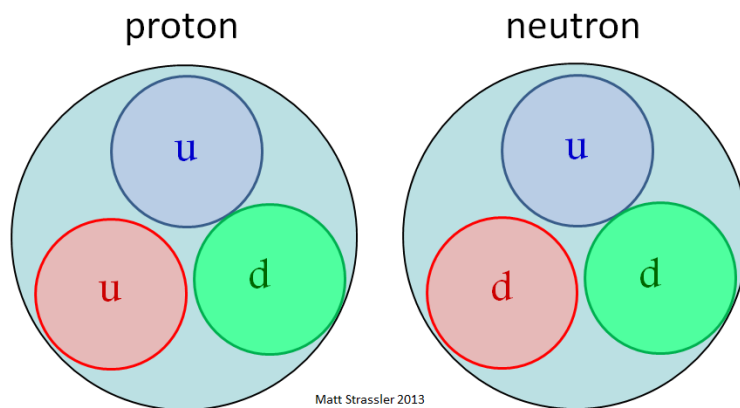


Figure 1.1: Visualisation of the content of the proton and neutron [1].

There are six known flavours of quarks: up, down, charm, strange, bottom and top. The Standard Model does not exclude the possibility of further generation and flavours, but strong evidence supporting this has not been presented until this day. Quarks carry an electric charge, which is of $+\frac{2}{3}$ of the elementary charge for up type quarks (up, charm and bottom) and $-\frac{1}{3}$ for down type quarks (down, strange, top). The quarks also carry a colour charge (red, green, blue) which defines their interaction under the strong force. Mesons are composed of quarks and anti-quarks. Barions are composed of 3 quarks of a different colour.

Leptons are also grouped into generations consisting of charged particles and corresponding neutrinos. Charged electrons, muons and taons can interact through electromagnetic and weak interactions, while the neutral neutrinos interact only through weak interactions. Neutrinos are massless within the Standard Model; however, the recent observation of neutrinos and their oscillations provide evidence of their non-zero mass [2].

Quarks and leptons can be organised in a three-fold family structure (a similar structure can also be created for antiparticles):

$$\begin{bmatrix} \nu_e & u \\ e^- & d \end{bmatrix}, \quad \begin{bmatrix} \nu_\mu & c \\ \mu^- & s \end{bmatrix}, \quad \begin{bmatrix} \nu_\tau & t \\ \tau^- & b \end{bmatrix}, \quad (1.1)$$

where one can find:

- left-handed quark doublet: $Q_{Li} = \begin{pmatrix} u_L \\ d_L \end{pmatrix}_i$,
- right-handed quark singlet: u_{Ri}, d_{Ri} ,
- left-handed lepton doublet: $L_{Li} = \begin{pmatrix} \nu_l \\ e_l^- \end{pmatrix}_i$,
- right-handed lepton singlet: l_{Ri} .

There are no right-handed neutrinos in the SM.

The Standard Model is a local gauge theory described within the quantum mechanics and relativity framework called the quantum field theory. Each particle is interpreted as a quantum (point-like) of a respective field and appropriate transformation properties under the Lorentz group. The local gauge group of symmetry of the SM is defined as:

$$SU(3)_C \times SU(2)_L \times U(1)_Y, \quad (1.2)$$

where $SU(3)_C$ describes the symmetry of the strong force theory (QCD), and C is the field's colour charge.

The group $SU(2)_L \times U(1)_Y$ represents the symmetry group of the electroweak interactions, and L and Y refer to the weak interaction's chirality and to the hypercharge.

The Standard Model Lagrangian describes the evolution of a system of discrete particles, each with a finite number of degrees of freedom. There are several components of SM Lagrangian:

$$\mathcal{L}_{SM} = \mathcal{L}_{Kin} + \mathcal{L}_{Gauge} + \mathcal{L}_{Higgs} + \mathcal{L}_{Yukawa}. \quad (1.3)$$

The \mathcal{L}_{Kin} introduce the massless fermion fields. The \mathcal{L}_{Kin} is defined as:

$$\mathcal{L}_{Kin} = i\bar{\psi}\gamma^\mu\mathcal{D}_\mu\psi, \quad (1.4)$$

where \mathcal{D}_μ is the covariant derivative that replaced the standard in order to maintain the gauge invariance defined as:

$$\mathcal{D}_\mu = \partial^\mu + ig_s G_a^\mu \mathcal{L}_a + ig W_b^\mu T_b + ig' B^\mu Y, \quad (1.5)$$

and G_a^μ stands for eight gluons, W_b^μ are W bosons, \mathcal{L}_a are the $SU(3)_C$ group generators (Gell-Mann matrices), T_b are the $SU(2)_L$ group generators (Pauli matrices), Y is the $U(1)_Y$ charge and B^μ is hypercharge boson.

\mathcal{L}_{Gauge} describes the boson kinetic term:

$$\mathcal{L}_{Gauge} = -\frac{1}{4} G_{\mu\nu}^a (G^a)^{\mu\nu} - \frac{1}{4} W_{\mu\nu}^d (W^d)^{\nu\mu} - \frac{1}{4} B_{\mu\nu} B^{\mu\nu}. \quad (1.6)$$

\mathcal{L}_{Higgs} introduces Higgs potential and spontaneous symmetry breaking which allows particle to acquire mass. It is defined as:

$$\mathcal{L}_{Higgs} = (\nabla_\mu \phi)^\dagger (\nabla^\mu \phi) + \mu^2 (\phi^\dagger \phi) + |\lambda| (\phi^\dagger \phi)^2, \quad (1.7)$$

where ϕ is $SU(2)$ doublet of spin-0 complex fields ($\langle \phi \rangle = \frac{v}{\sqrt{2}}$), λ describes quartic self-interactions among the scalar fields and v is vacuum expectation value. The first term represent the kinetic energy of the field and other the mass term. The gauge symmetry is broken in the Spontaneous Symmetry Breaking (SSB) of the electroweak group to the electromagnetic subgroup:

$$SU(3)_C \times SU(2)_L \times U(1)_Y \rightarrow SU(3)_C \times U(1)_{QED}, \quad (1.8)$$

which generate masses of the fermions and bosons. The result of symmetry breaking is a particle called Higgs Boson.

Finally, the \mathcal{L}_{Yukawa} describes interactions between the Higgs field and fermions.

$$\mathcal{L}_{Yukawa} = Y_{ij}^d \overline{Q}_{Li}^I \phi d_{Rj}^I + Y_{ij}^u \overline{Q}_{Li}^I \tilde{\phi} u_{Rj}^I + Y_{ij}^l \overline{L}_{Li}^I \phi l_{Rj}^I + h.c., \quad (1.9)$$

where $h.c.$ is hermitian conjugate, $Y_{ij}^{d,u,l}$ are 3×3 complex matrices ($i, j = 1, 2, 3$) which describe the so-called Yukawa couplings between the Higgs doublet ϕ and the fermions.

The two first terms conserve Charge-Parity (CP) symmetry (which is described in detail in this chapter), and the \mathcal{L}_{Yukawa} violates CP symmetry. Under SSB, this term

becomes \mathcal{L}_{Mass} .

$$\mathcal{L}_{Mass} = \overline{d}_{Li}^I M_{ij}^d d_{Rj}^I + \overline{u}_{Li}^I M_{ij}^u u_{Rj}^I + \overline{l}_{Li}^I M_{ij}^l L_{Rj}^I + h.c., \quad (1.10)$$

where: $M_{ij}^{d,u,l} \equiv \frac{v}{\sqrt{2}} Y_{ij}^{d,u,l}$

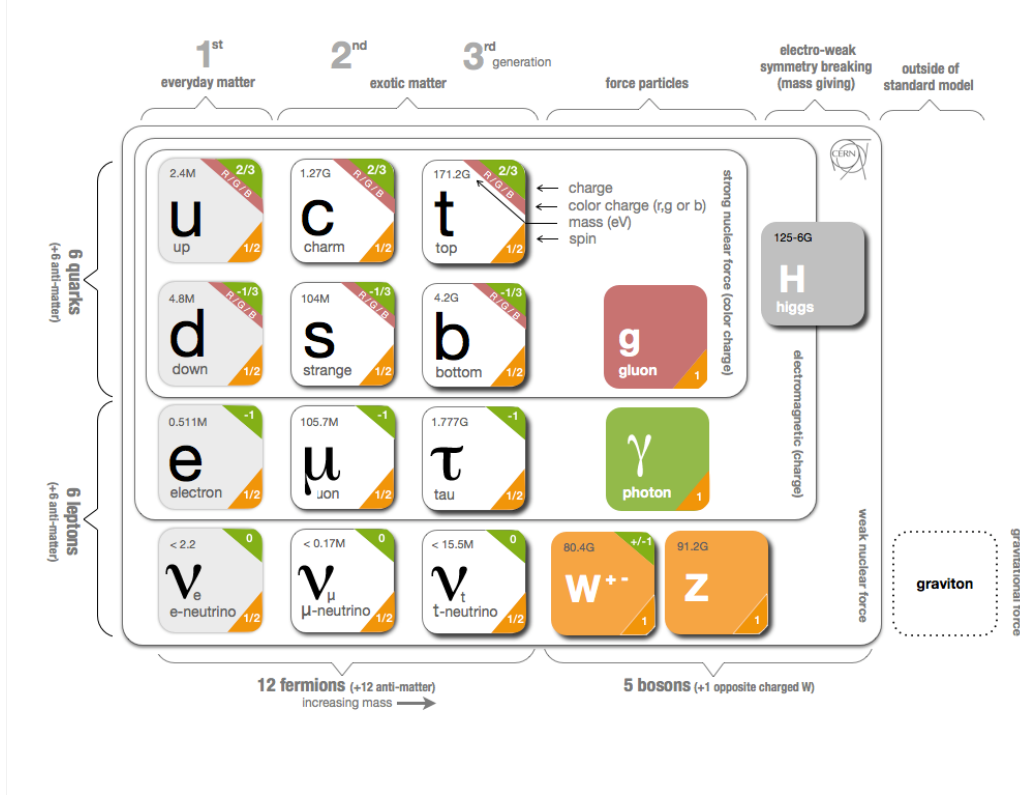


Figure 1.2: Summary of the Standard Model particles and forces [3].

The CP symmetry violation is introduced by an irreducible complex physical phase in \mathcal{L}_{Yukawa} term. From the \mathcal{L}_{Kin} term, one can express the charge current interaction between the quarks and charged $SU(2)_L$ gauge bosons as functions of the weak interaction eigenstates:

$$\mathcal{L}_{W^\pm} = \frac{-g}{\sqrt{2}} \overline{Q}_{Li}^I \gamma^\mu W_\mu^+ Q_{Li}^I + h.c. \quad (1.11)$$

Expressing it as a function of the mass eigenstates, the formula can be rewritten as:

$$\mathcal{L}_{W^\pm} = \frac{-g}{\sqrt{2}} (\overline{u}_L, \overline{c}_L, \overline{t}_L) \gamma^\mu W_\mu^+ V_{CKM} \begin{pmatrix} d_L \\ s_L \\ b_L \end{pmatrix} + h.c., \quad (1.12)$$

where V_{CKM} is known as the Cabibbo-Kobayashi-Maskawa (CKM) matrix [2].

1.2 The CKM matrix

The weak force couples pairs of weak quark eigenstates, allowing flavour transition. The weak eigenstates are not the same as the mass eigenstates, and their difference is described by the CKM matrix (Eq. 1.12). A down-type mass eigenstate is a superposition of all three down-type weak eigenstates and can transition to any of them. It means that the transitions of quarks between generations via flavour-changing processes mediated by the weak charged-current interaction are allowed, see matrix in Eq. 1.13.

$$\begin{pmatrix} d' \\ s' \\ b' \end{pmatrix} = \begin{pmatrix} V_{ud} & V_{us} & V_{ub} \\ V_{cd} & V_{cs} & V_{cb} \\ V_{td} & V_{ts} & V_{tb} \end{pmatrix} \begin{pmatrix} d \\ s \\ b \end{pmatrix} \quad (1.13)$$

The d , s and b are flavour eigenstates of down-type quarks, d' , s' , b' are weak-interaction eigenstates and V_{ij} , $i = u, c, t, j = d, s, b$ are the CKM matrix elements. The CKM matrix elements are complex numbers and transform under the CP into their complex conjugates as: $V_{ij} \rightarrow V_{ij}^*$ what opens the possibility for observation of CPV in the Standard Model. The value of V_{ij} squared describes the probability of quark's transitions [2]:

$$\begin{pmatrix} |V_{ud}| & |V_{us}| & |V_{ub}| \\ |V_{cd}| & |V_{cs}| & |V_{cb}| \\ |V_{td}| & |V_{ts}| & |V_{tb}| \end{pmatrix} = \begin{pmatrix} 0.974 & 0.227 & 0.004 \\ 0.226 & 0.973 & 0.041 \\ 0.009 & 0.040 & 0.999 \end{pmatrix} \quad (1.14)$$

where the uncertainties are $\mathcal{O}(10^{-3})$ or smaller. The magnitude of the diagonal amplitudes indicates that transitions between the same generation are the most likely, whereas transitions between generations are less probable.

1.3 Limitation of the Standard Model

Undeniably, the Standard Model has been extensively confirmed experimentally theory of particle physics. However, there is a number of limitations related to well-known physics aspects. The neutrinos, which are predicted to have zero mass, have a non-zero mass which has been measured in studies of heavy flavour oscillations [2].

The size of the imbalance of matter and antimatter in the Universe (which is a central point of the physics program of the LHCb experiment) is also not explained in the SM. The Standard Model predicts that matter and antimatter should have been created in equal amounts. Observations of the Universe have showed that either this assumption is false or in the early Universe existed processes that violated the matter - antimatter symmetry. One possible solution is that large charge parity violating (*CPV*) effects may have occurred in as yet undiscovered physics beyond the SM [4][5].

The approach of incorporating gravity into the SM has not succeeded either. The Standard Model does not predict and explain the source of the fourth force - gravity. Moreover, general relativity and quantum theory are well known as incompatible, which impedes the explanation of the phenomenon of gravity [6]. The solution to this puzzle is particularly hard, since the gravity seems to be a macroscopic phenomenon and is not related with interaction of any kind - the gravity is just curvature of time-space and is a purely of geometric nature.

The SM does not explain the particle quantum numbers which are externally provided, such as the electric charge Q , weak isospin I , hypercharge Y and colour, gauge couplings, *CP*-violating parameter, quark and charged-lepton masses and three Cabibbo weak mixing angles and more [2].

The theory that could describe the effects that the Standard Model does not predict supersymmetry (SUSY). In SUSY theory, each particle has a super-partner *s-particle*, which differs by half a unit of spin (spin-0 for sfermion and half-spin for gauge fields). If supersymmetry particles were asymmetry of particles, the particles would have the same masses as the particles and would have already been discovered. Although the exact mass scale of SUSY particles is unknown, there are predictions of particles with relatively low mass that modern particle detectors should observe. There is no evidence of the direct production of SUSY particles to this day [7],[8].

1.4 CPV

In the early Universe, at the large scale of thermal energy, there were an equal number of baryons and antibaryons created in the process of creating particles ($\gamma \rightarrow p\bar{p}$). During the expansion of the Universe, the temperature decreased as the photon's energy, which led to a decrease in the number of particles that appears in the pair's creation. Because of that, the number of baryons and antibaryons in the Universe became stable.

The process of creation of matter and antimatter in the early Universe is called baryogenesis. Without any violation of symmetry of matter and antimatter, no baryons could survive recombination with antimatter.

The size of asymmetry between the matter is around 10^{-9} , which means that, for every 10^9 antibaryon in the early Universe, there must have been 10^9 plus one baryon. As a result of the recombination of 10^9 baryons and antibaryons, only one baryon is left.

The source of this asymmetry was widely studied by Andrei Sakharov², who has formulated three conditions [9]:

- baryon number violation,
- C -symmetry and CP -symmetry violation,
- interactions out of thermal equilibrium.

Baryon number violation is directly necessary to produce an excess number of baryons over antibaryons. The departure from thermal equilibrium is necessary since, in thermal equilibrium, any baryon number violating process is balanced by the inverted process.

The sources of CP violation in the Universe are currently widely studied. Extensive studies were performed in beauty [5] and charm [10] sector. These measurements do not fully explain the observed CP violation, which is a motivation for further searches of other sources.

There are three different types of the CP violation:

- direct CP violation which manifests in the difference between partial decay width of process and its complex conjugate, i.e. $\Gamma(X \rightarrow Y) \neq \Gamma(\bar{X} \rightarrow \bar{Y})$,
- indirect CP violation in the mixing of neutral mesons ($B_s^0 - \bar{B}_s^0, B^0 - \bar{B}^0$, etc.),
- CP violation in mixing manifests in the interference between direct and indirect CP violation.

The Standard Model partly explains the size of phenomena of CPV . This effect in the CKM matrix can be seen through particular parametrisations. For example, in Wolfenstein parametrisation [11], it can be expressed as:

²Andrei Sakharov (21 May 1921 – 14 December 1989) was a Soviet and Russian nuclear physicist, dissident, Nobel laureate, and activist for disarmament, peace and human rights.

$$V_{CKM} = \begin{pmatrix} 1 - \frac{\lambda^2}{2} & \lambda & A\lambda^3(\rho - i\eta) \\ -\lambda & 1 - \frac{\lambda^2}{2} & A\lambda^2 \\ A\lambda^3(1 - \rho - i\eta) & -A\lambda^2 & 1 \end{pmatrix} + \mathcal{O}(\lambda^4), \quad (1.15)$$

where A , ρ , η are real parameters. The CPV in the SM using this parametrisation is accounted in η .

The CKM matrix is unitary. Providing unitary condition: $\sum_i V_{ij}V_{ik}^* = \delta_{jk}$ ($i = u, c, t$, j and $k = d, b, s$), nine equations may be constructed. Each of them corresponding to a vector in the $\bar{\rho}, \bar{\eta}$ plane, where $\bar{\rho} = \rho(1 - \lambda^2/2)$ and $\bar{\eta} = \eta(1 - \lambda^2/2)$. Because of unitary condition, these vectors define *Unitarity Traingles* (Fig. 1.3).

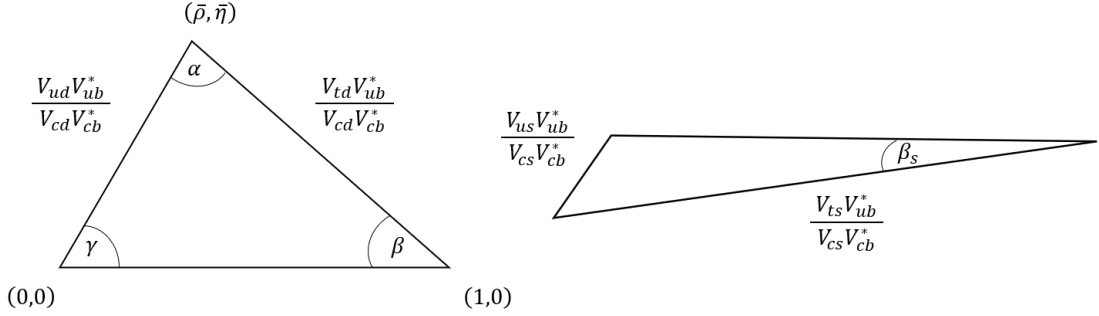


Figure 1.3: Unitarity Triangles.

Only two of them represent objects which can be studied experimentally: $V_{ud}V_{ub}^* + V_{cd}V_{cb}^* + V_{td}V_{tb}^* = 0$ and $V_{us}V_{ub}^* + V_{cs}V_{cb}^* + V_{ts}V_{tb}^* = 0$.

$$\alpha = \arg \left(-\frac{V_{td}V_{tb}^*}{V_{ud}V_{ub}^*} \right) \quad (1.16)$$

$$\beta = \arg \left(-\frac{V_{cd}V_{cb}^*}{V_{td}V_{tb}^*} \right) \quad (1.17)$$

$$\gamma = \arg \left(-\frac{V_{ud}V_{ub}^*}{V_{cd}V_{cb}^*} \right) \quad (1.18)$$

$$\beta_s = \arg \left(-\frac{V_{ts}V_{tb}^*}{V_{cs}V_{cb}^*} \right) \quad (1.19)$$

The other parametrisation, called Standard Parametrisation, describes the CKM matrix by magnitudes of their elements and weak phases:

$$\begin{pmatrix} d' \\ s' \\ b' \end{pmatrix} = \begin{pmatrix} |V_{ud}| & |V_{us}| & |V_{ub}|e^{-i\gamma} \\ -|V_{cd}| & |V_{cs}| & |V_{cb}| \\ |V_{td}|e^{-i\beta} & -|V_{ts}|e^{-i\beta_s} & |V_{tb}| \end{pmatrix} \begin{pmatrix} d \\ s \\ b \end{pmatrix} \quad (1.20)$$

which illustrates in which processes (processes in which there are quark transitions corresponding to particular elements of the CKM matrix) individual parameters can be measured.

The current constraints on the CKM parameters are obtained from the measurement of the CKM matrix parameters performed by different collaborations (LHC: ATLAS, CMS, LHCb, ALICE and other: Belle, BaBar, CDF) [12]-[13]. These measurements may provide strong evidence against or in favour of New Physics beyond the Standard Model (BSM); however, no evidence has been found so far. Especially interested are studies of differences between processes described by tree-level diagrams [14] and others affected by loops [15]. These studies and a mathematical description of the relationship between angles of the CKM matrix and CPV are described in Chapter 1.4.

Because of this strict relationship, studies of CPV can be exploited in probing Standard Model limitations. The LHCb experiment focuses on extended studies of the heavy meson sector in its physics program. Quark transitions occurring in decays and oscillations of mesons of this sector are related to the angle γ of the CKM matrix. Measurement of the CKM angle γ in tree-level processes is called *the standard candle* for the Standard Model because of very small theoretical uncertainty: $\Delta\gamma/\gamma < 10^{-7}$ [16]. Any discrepancies between angle γ measured in processes with loops and only tree-level processes may provide strong evidence for the effects which the Standard Model does not explain. Fig. 1.4 show the recent (2021, [17]) result of the measurement of the CKM matrix parameters (α , β , γ , $|V_{ub}|$, ϵ_K , δm_s and more), including the CKM angle γ measured using only tree-level processes (Fig. 1.4-top) and all modes (Fig. 1.4-bottom).

The angle γ can be probed using several methods. These methods differ in the final state, intermediate state and type of B meson.

1.4.1 The Gronau, London and Wyler method

A method for extracting γ with the use of amplitude relations was originally proposed by Gronau, London and Wyler [18]. This method (GLW) was based on the interference between the $B^- \rightarrow K^- D^0$ ($b \rightarrow c\bar{u}s$) and the $B^- \rightarrow K^- \bar{D}^0$ ($b \rightarrow u\bar{c}s$) diagrams

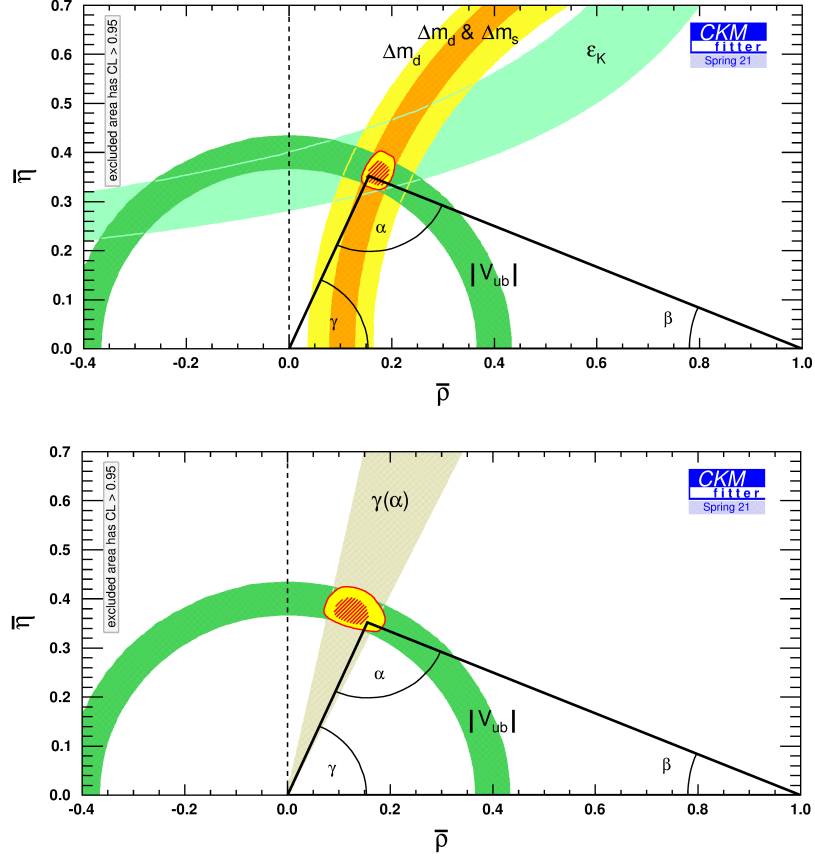


Figure 1.4: Result of the measurement of the CKM matrix parameter using only tree-level processes (top) and all possible modes (bottom)[17].

once the D^0 and the \bar{D}^0 mesons decay to their CP states. In the original proposal, the direct CP violation and the CKM angle γ can be extracted via six decay processes: $B^- \rightarrow K^- D^0$ (\bar{D}^0), $B^- \rightarrow K^- D_{CP}$ (D_{CP} denotes that the D^0 or the \bar{D}^0 is seen in a CP eigenstate) and their CP conjugate decays. The sensitivity to CP violation is achieved through the interference of the two quark level processes: $b \rightarrow c\bar{u}s$ and $b \rightarrow u\bar{c}s$ with a relative phase γ . If D_{CP} denotes the CP eigenstate of the neutral D -meson system with eigenvalue $CP = +1$ (K^+K^- , $\pi^+\pi^-$) or $CP = -1$ ($K_s\phi$, $K_s\pi^0$) then:

$$D_{CP} = \frac{1}{\sqrt{2}} (D^0 \pm \bar{D}^0) \quad (1.21)$$

and, for $CP = +1$ one can obtain the relations:

$$\sqrt{2}A(B^- \rightarrow K^- D_{CP}) = A(B^- \rightarrow K^- \bar{D}^0) + A(B^- \rightarrow K^- D^0), \quad (1.22)$$

$$\sqrt{2}A(B^+ \rightarrow K^+ D_{CP}) = A(B^+ \rightarrow K^+ \bar{D}^0) + A(B^+ \rightarrow K^+ D^0). \quad (1.23)$$

The $B^- \rightarrow K^- \bar{D}^0$ amplitude is an order of magnitude smaller than the $B^- \rightarrow K^- D^0$ one because the $K^- \bar{D}^0$ is colour-suppressed while $K^- \bar{D}$ is not. In addition, the CKM factors suppress this amplitude ratio by about 1/3. That results in the two interfering amplitudes being very different in magnitude:

$$\left| \frac{A(B^- \rightarrow K^- \bar{D}^0)}{A(B^- \rightarrow K^- D^0)} \right| = \left| \frac{A(B^+ \rightarrow K^+ D^0)}{A(B^+ \rightarrow K^+ \bar{D}^0)} \right| \approx \frac{1}{\lambda} \left| \frac{V_{ub}}{V_{cb}} \right| \times \frac{a_1}{a_2} \approx 0.1 \quad (1.24)$$

and thus, the interference effects are limited to $\mathcal{O}(10\%)$. Above, the a_1/a_2 ratio denotes the relative size of Cabbibo suppressed to allowed amplitudes. Nothing changes when the CP conjugated final states are considered, except that the CKM elements must be complex conjugated. Apparently, the CP -conjugated triangle can also be determined, and the $A(B^+ \rightarrow K^+ D^0)$ is rotated by 2γ with respect to $A(B^- \rightarrow K^- \bar{D}^0)$ and the γ angle can be extracted.

Denoting:

$$\begin{aligned} A_1 &\equiv A(B^- \rightarrow K^- D^0) = A(B^+ \rightarrow K^+ \bar{D}^0), \\ A_2 &\equiv A(B^- \rightarrow K^- \bar{D}^0), \\ \bar{A}_2 &= A_2 e^{2i\gamma}, \\ A_3 &\equiv \sqrt{2} A(B^- \rightarrow K^- D_{CP}) = A_1 + A_2 e^{i(\gamma-\delta)}, \\ A_4 &\equiv \sqrt{2} A(B^+ \rightarrow K^+ D_{CP}) = A_1 + A_2 e^{i(\gamma+\delta)}, \end{aligned} \quad (1.25)$$

where δ is a strong phase difference.

One has:

$$\begin{aligned} \Gamma(B^- \rightarrow K^- D^0) &= \Gamma(B^+ \rightarrow K^+ \bar{D}^0) = A_1^2, \\ \Gamma(B^- \rightarrow K^- \bar{D}^0) &= \Gamma(B^+ \rightarrow K^+ D^0) = A_2^2, \end{aligned} \quad (1.26)$$

and:

$$\begin{aligned} \Gamma(B^- \rightarrow K^- D_{CP}) &= \frac{1}{2} [A_1^2 + A_2^2 \pm 2 A_1 A_2 \cos(\delta - \gamma)], \\ \Gamma(B^+ \rightarrow K^+ D_{CP}) &= \frac{1}{2} [A_1^2 + A_2^2 \pm 2 A_1 A_2 \cos(\delta + \gamma)]. \end{aligned} \quad (1.27)$$

The CP violation in all these processes occurs only in:

$$\Gamma(B^+ \rightarrow K^+ D_{CP}) \neq \Gamma(B^- \rightarrow K^- D_{CP}). \quad (1.28)$$

In practice, the direct CP violating effects will be seen through:

$$A(B^+ \rightarrow K^+ D^0) = A(B^- \rightarrow K^- \bar{D}^0) \times e^{2i\gamma}. \quad (1.29)$$

If all the corresponding branching ratios are known, one can extract the interference effects and thus determine the $\cos(\delta \pm \gamma)$ and the values of the strong and weak phases.

1.4.2 The Atwood, Dunietz and Soni method

The alternative approach was proposed by Atwood, Dunietz and Soni [19]. They pointed out that despite the initial decay $B^- \rightarrow K^- \bar{D}^0$ is *colour-suppressed*³ and $B^- \rightarrow K^- D^0$ is colour allowed, the difference in the decay rates of $\bar{D}^0 \rightarrow K^- \pi^+$ and $D^0 \rightarrow K^- \pi^+$ tends to overcome this tendency. The final states are indistinguishable and will interfere.

In this method, one can take advantage of the significant interference effects. Here both contributing decay amplitudes, leading to the same final state f_D , should be of comparable size (Eq. 1.30), which causes large CP -violating effects. The difficult to measure $\Gamma(B^- \rightarrow K^- \bar{D}^0)$ is not required and can be even determined by the experimental observable.

$$\left| \frac{A(B^- \rightarrow K^- \bar{D}^0(\rightarrow K^+ \pi^-))}{A(B^- \rightarrow K^- D^0(\rightarrow K^+ \pi^-))} \right|^2 \approx 1 \quad (1.30)$$

In particular, large asymmetries are possible for final state f_D such that $D^0 \rightarrow f_D$ is doubly Cabbibo suppressed, and $\bar{D}^0 \rightarrow f_D$ is Cabbibo allowed. The final state f_D could be for instance $f_D = K^+ \pi^-$, $K_S^0 \pi^+ \pi^-$, etc.

This approach is also challenging since it is useful only if a couple of different channels are involved, usually with total branching fractions of $\mathcal{O}(10^{-7})$. An accurate determination of relevant D -meson branching ratios $\mathcal{B}(D^0 \rightarrow f)$ and $\mathcal{B}(\bar{D}^0 \rightarrow f)$ is also essential.

³When a quark from decay of virtual W boson must be combined with an anti-quark, the other anti-quarks will have the right colour to form a colour singlet only one-third of the time. Therefore, these decays are colour-suppressed.

1.4.3 The Giri, Grossman, Soffer, and Zupan method

The GGSZ method [20] was proposed by Giri, Grossman, Soffer and Zupan and includes multibody $D \rightarrow K_S^0 h^+ h^-$ decays where h stands for kaon or pion with the analysis of the Dalitz space (visual representation of the phase-space of a three-body decay involving spin-0 particle). The binning eliminates the model-dependent systematic uncertainty in the measurement. The signal yield in each bin is given by:

$$\Gamma_i^\pm \propto N_i + r_B^2 \bar{N}_i + 2\sqrt{N_i \bar{N}_i} (c_i x_\pm + s_i y_\pm), \quad (1.31)$$

where $x_\pm = r_B(\cos(\delta_B \pm \gamma))$, $y_\pm = r_B(\sin(\delta_B \pm \gamma))$.

Here, N_i is the number of events in the i^{th} bin of a flavour tagged⁴ D decay sample, c_i and s_i are the amplitude-averaged strong phase difference between D^0 and \bar{D}^0 over i^{th} bin. The (x_\pm, y_\pm) parameters can be obtained from Eq. 1.31 using maximum likelihood method⁵.

1.4.4 Time-dependent method

Time-dependent method [23] is based on the transition of B_s^0 and \bar{B}_s^0 flavour eigenstates to the final state f . The flavour eigenstates of B_s^0 mesons are an admixture of the physical mass eigenstates $|B_L\rangle = p|B_s^0\rangle + q|\bar{B}_s^0\rangle$ and $|B_H\rangle = p|B_s^0\rangle - q|\bar{B}_s^0\rangle$ where $|p|^2 + |q|^2 = 1$. From the differential decay rates for initially produced B_s^0 or \bar{B}_s^0 one can derive observables - mixing asymmetries and coefficients which are defined as:

$$\begin{aligned} A_{mix}^f(t) &= \frac{N_f(t) - \bar{N}_f(t)}{N_f(t) + \bar{N}_f(t)} = \frac{C_f \cos(\Delta m_s t) - S_f \sin(\Delta m_s t)}{\cosh(\frac{\Delta\Gamma_{st}}{2}) + A_f^{\Delta\Gamma} \sinh(\frac{\Delta\Gamma_{st}}{2})}, \\ A_{mix}^{\bar{f}}(t) &= \frac{\bar{N}_{\bar{f}}(t) - N_{\bar{f}}(t)}{\bar{N}_{\bar{f}}(t) + N_{\bar{f}}(t)} = \frac{C_f \cos(\Delta m_s t) + S_{\bar{f}} \sin(\Delta m_s t)}{\cosh(\frac{\Delta\Gamma_{st}}{2}) + A_{\bar{f}}^{\Delta\Gamma} \sinh(\frac{\Delta\Gamma_{st}}{2})}, \\ C_f &= \frac{1 - r^2}{1 + r^2}, \\ A_f^{\Delta\Gamma} &= -\frac{2r\kappa(\delta - (\gamma - 2\beta_s))}{1 + r^2} & S_f^{\Delta\Gamma} &= +\frac{2r\kappa(\delta - (\gamma - 2\beta_s))}{1 + r^2}, \\ A_{\bar{f}}^{\Delta\Gamma} &= -\frac{2r\kappa(\delta + (\gamma + 2\beta_s))}{1 + r^2} & S_{\bar{f}}^{\Delta\Gamma} &= +\frac{2r\kappa(\delta + (\gamma + 2\beta_s))}{1 + r^2}, \end{aligned} \quad (1.32)$$

⁴It is a procedure which allows identify the initial flavour of neutral particle by looking at the flavour at decay, which is defined by the electric charge of the decay products in the final state [21].

⁵description of method can be found in [22]

where N indicates the number of B_s^0 or \bar{B}_s^0 mesons decaying to given f or \bar{f} final state.

1.5 Motivation for searching for new $B \rightarrow DK$ channels

Measurement of the CKM angle γ provided by the LHCb spectrometer is the most precise measurement of the angle γ from a single experiment [14]. This measurement is a combination of a series of single measurements, and the most precise one is obtained in the analysis of the $B^+ \rightarrow DK^+$ decay, where D stands for a superposition of D^0 and \bar{D}^0 mesons reconstructed from the same final state [14]. However, extended studies of other $B \rightarrow DK$ type channels, including decays through resonance states, increase the precision of the γ measurement. This is the primary motivation for searching for new $B \rightarrow DK$ channels. The expected precision of sensitivity of γ from time-integrated measurements (ADS, GLW, GGSZ methods) is shown in Fig. 1.5. For time-dependent studies, there is no such precise prediction, but expected sensitivities of γ from $B \rightarrow DK$ decay decays are about 4° , 2.5° and 1° after collecting 23, 50 and 300 fb^{-1} , during Run 3, 4 and 5 respectively [24].

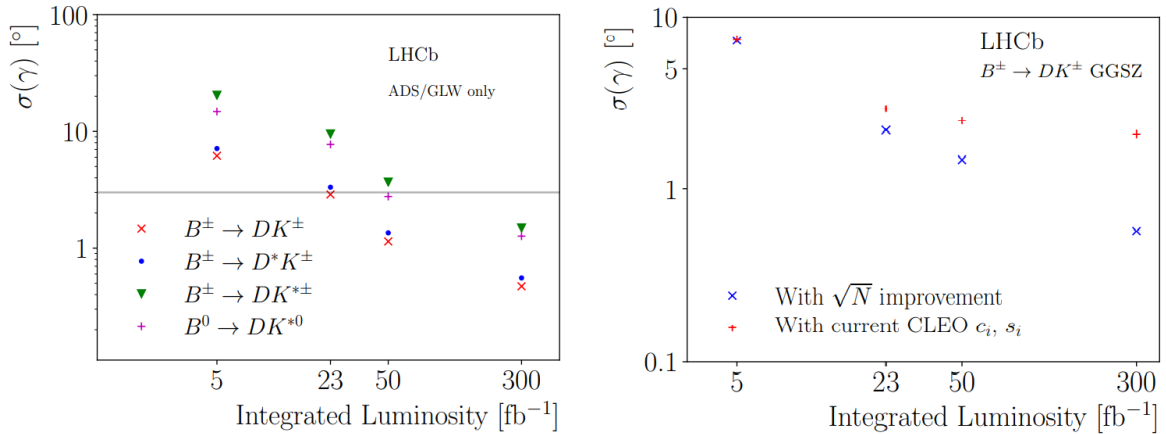


Figure 1.5: Extrapolation of γ sensitivity from the ADS/GLW (left) and GGSZ ($B^\pm \rightarrow DK^\pm$, right) The expected Belle II γ precision at an integrated luminosity of 50 ab^{-1} is shown by the horizontal grey lines [24].

Chapter 2

LHCb experiment

The largest accelerator on Earth is the Large Hadron Collider at CERN. The following paragraph describes the history of CERN and the performance of LHC and LHCb spectrometers. The description of all LHCb subsystems is followed by a discussion about the modernisation of the tracking system and trigger for Run 3 and 4.

2.1 CERN

The European Organization for Nuclear Research (CERN - fr. Conseil Européen pour la Recherche) was established on 29 September 1954 by 12 countries in Western Europe. The main motivation was to reclaim European physicists scattered in Europe and other countries due to World War II [25],[26]. The original purpose of CERN was studies of nuclear physics, but soon it was applied to high-energy physics and other fields of science. To emphasise the non-military purpose of the laboratory, the CERN constitution prohibits any military research at CERN. CERN is recognised for high-level studies of particle physics; however, scientists at CERN perform also advanced studies in astrophysics, computing, theoretical physics, medical application of physics and more. The central part of the laboratory is located near Geneva (Switzerland has been chosen due to its political neutrality), but other CERN facilities are split between Switzerland and France. Nowadays, more than 17 000 people work in CERN (about 3000 of personnel and 14,000 associated with CERN) as physicists, engineers, administrators, and more [27].

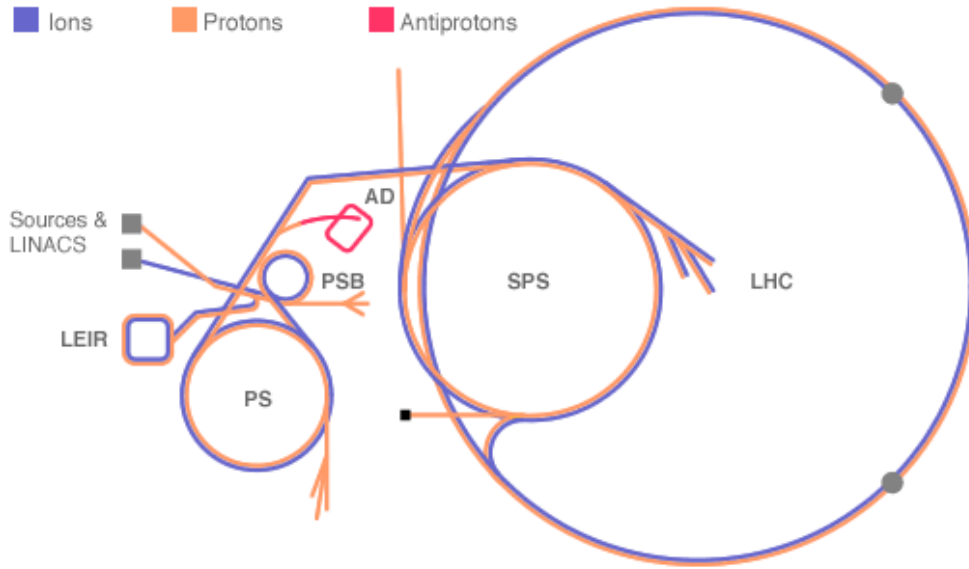


Figure 2.1: Schematic view of accelerator complex at CERN [28].

2.2 LHC

The Large Hadron Collider (LHC) was built at CERN between 1998 and 2008. It occupies the LEP (Large Electron Positron collider) tunnel, 175 meters underground with a total length of 27 kilometres [29]. It is divided into eight straight and eight arc sections. Each one has a different purpose (maintenance of accelerator, cooling etc.). The LHC ring accommodates 1232 dipoles (15 meters long and 35 tonnes weight, Fig. 2.2, [30]). These superconducting electromagnets use a current of 11,000 amperes to produce magnetic field 8.33 T (power of dipole magnetic field, about 100,000 times more than Earth's magnetic field). Dipoles have to be cooled to the temperature of 1.9 K. Two liquid gas is used: helium (cooling of dipoles) and nitrogen (powering, prevent for too fast cooling of materials). The quadrupole magnets (858) squeeze particles closer together before the collision, which increases the total number of collisions in each cross-section of beams [31].

The accelerator complex (Fig. 2.1) at CERN is a sequence of devices that accelerate particles to nominal energy of the LHC (6.5 TeV per beam during Run 2). Each accelerator increases the particle's energy before injecting the beam into the next machine. The proton source is a simple bottle of hydrogen gas located in the Linac 2 laboratory [32]. An electric field strips hydrogen atoms of their electrons to yield protons. Linac 2, the first accelerator in the chain, accelerates the protons to the energy of $50 \text{ MeV}/c^2$. Then,

the beam is injected into the Proton Synchrotron Booster (PSB, [33]), which accelerates the protons to 1.4 GeV, followed by the Proton Synchrotron (PS, [34]), which increases energy to 25 GeV. Protons are then injected into the Super Proton Synchrotron (SPS, [35]), where they are accelerated to 450 GeV (Fig. 2.1). The final one – LHC accelerates particles (protons and ions) up to the energy of 6.5 TeV per beam and collides them [36], [37].

Heavy ions are also collided in LHC either as lead–lead and proton-lead collisions. The accelerator, before Upgrade 1 (Run 1 and Run 2, [38]) collided protons up to a center-of-mass energy \sqrt{s} of 13 TeV with a maximum instantaneous luminosity: $\mathcal{L} = 10^{34} \text{cm}^{-2} \text{s}^{-1}$ and heavy ions (Pb - Pb) with a center-of-mass energy of 5 TeV at a instantaneous luminosity of $\mathcal{L} = 10^{27} \text{cm}^{-2} \text{s}^{-1}$ [36]. At the nominal beam condition, the beam consists of 2808 proton bunches per ring, each containing 10^{11} protons, and the frequency of collision at LHC reached 40 MHz [29].

The collider has four crossing points around which experiments are positioned: LHCb, ATLAS, CMS, ALICE, TOTEM, LHCf, MoEDAL and FASER (from Run 3) detectors (Fig. 2.3).

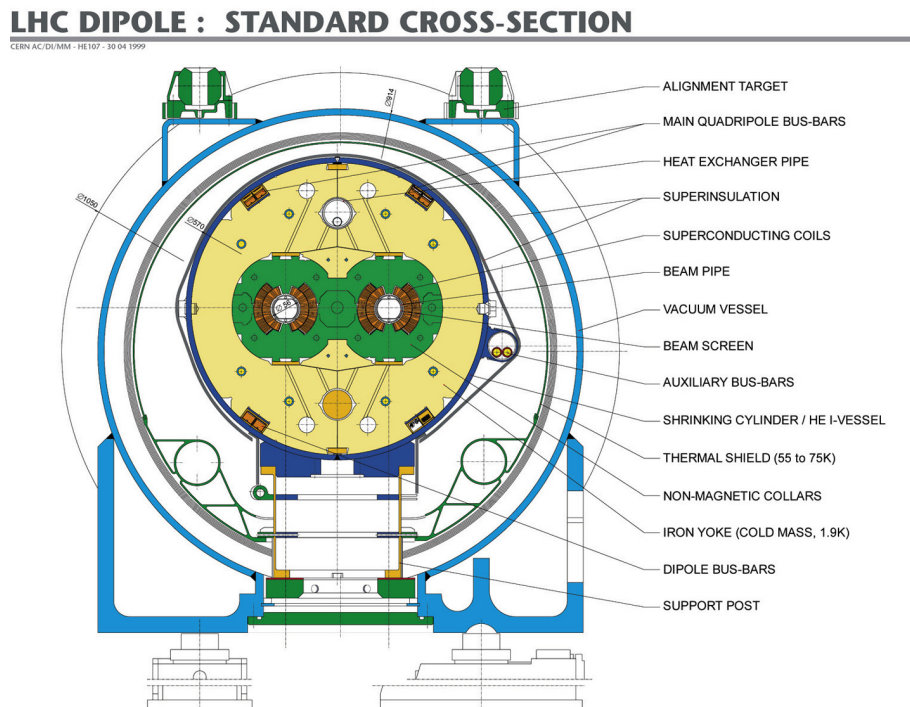


Figure 2.2: Diagram showing the cross-section of an LHC dipole magnet with description [39].

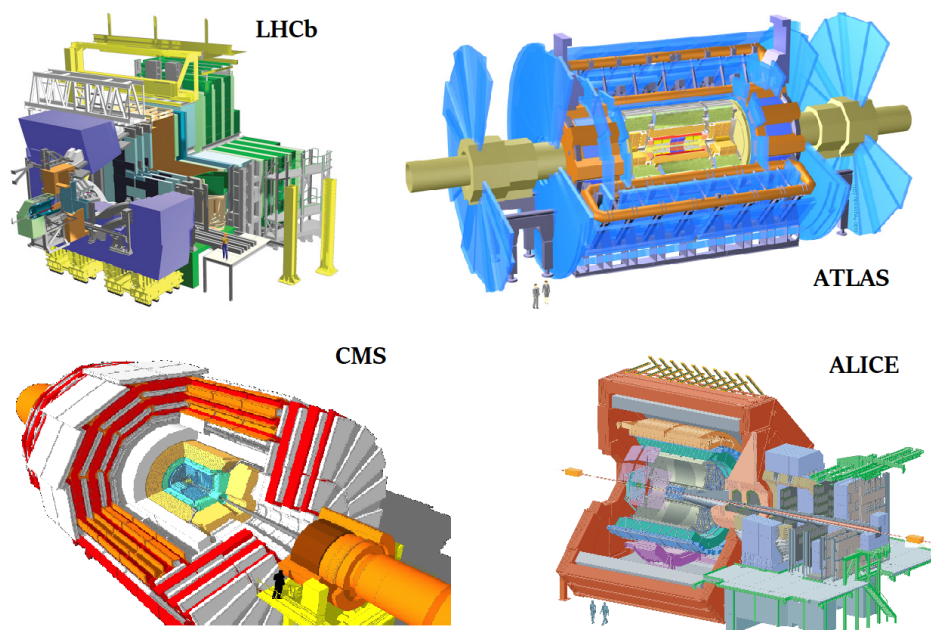


Figure 2.3: Schematic view of LHCb detector [40], ATLAS [41], CMS [42] and ALICE [43].

- **ATLAS** (Toroidal LHC ApparatuS): the general-purpose detector (Fig. 2.3-top right), designed to search for the Higgs Boson and evidence of theories of particle physics beyond the Standard Model. The detector is 46 metres long, 25 metres in diameter, and weighs about 7,000 tonnes. It is the largest at LHC. ATLAS is also the largest volume particle detector ever constructed. The detector is located close to the main CERN site in Switzerland [44].
- **CMS** (Compact Muon Solenoid): the Compact Muon Solenoid (CMS) is second (after ATLAS) general-purpose detector at the Large Hadron Collider (Fig. 2.3-bottom left). With similar scientific programs to the ATLAS experiment, CMS experimented with different technical solutions to validate the most important results of both experiments. A cylindrical coil of superconducting cable generates a field of 4T. It 21 metres long, 15 m in diameter, and weighs about 14,000 tonnes [45].
- **ALICE** (A Large Ion Collider Experiment): designed to advanced studies of products of heavy-ion collisions (Fig. 2.3-bottom right). Each year, after collecting data during proton-proton collisions, the LHC provides collisions between lead

ions, recreating an environment similar to the one just after the Big Bang. This environment is called quark-gluon plasma. Studies of quark-gluon plasma (QGP) properties are key issues in quantum chromodynamics (QCD) theory. The ALICE detector weight is a 10,000-tonne, 26 m long, 16 m high, and 16 m wide detector. It is located 56 m below ground close to the village of Saint Genis-Pouilly in France [46].

- **LHCb** (Large Hadron Collider beauty): designed to study the heavy flavour quark physics (Fig. 2.3-top left). Currently upgraded [47]. It is extensively discussed in Sec. 2.3 [48].
- **TOTEM** (TOTal Elastic and diffractive cross section Measurement): is designed to explore *forward physics* by taking precise measurements of protons colliding at small angles. These processes studies are especially interesting since these measurements are inaccessible in the other LHC experiments. TOTEM is the most extended experiment at LHC, and TOTEM detectors are spread across almost half a kilometre around the CMS interaction point. The sensor is composed of four-particle telescopes and 26 Roman pots. The telescopes track the particles emerging from collisions at the CMS interaction point while Roman Pots with silicon sensors perform measurements of scattered protons [49].
- **MoEDAL** (The Monopole and Exotics Detector at the LHC): experiment focus on searches for magnetic monopole – a hypothetical particle carrying a magnetic charge. The MoEDEL detector is built from 400 modules, each consisting of a stack of sheets of nuclear-track detectors. Any monopoles created during collisions at LHC would break long chains of molecules in plastic nuclear-track detectors and leave track throughout the whole detector.

Another purpose of the MoEDAL detector is to search for highly ionising Stable Massive Particles (SMPs), which are not described in the Standard Model and could provide evidence for New Physics [50].

- **LHCf** (The Large Hadron Collider forward): experiment performs precise measurement of particles thrown forward by collisions in the Large Hadron Collider, which can mimic cosmic rays. Cosmic rays occur when a particle with high energy hits the upper part of the Earth's atmosphere. As a result, a cascade of the particle is created. Studies of these particles are demanding since only a few particles hit the

Earth. LHCf comprises two detectors that sit along the LHC beamline at 140 metres on either side of the ATLAS collision point. This location allows the observation of particles at an angle of nearly zero degrees to the LHC beam direction. Each of the two detectors weighs only 40 kilograms, is 30 cm long, 80 cm high, and 10 cm wide [51].

- **FASER** (The Forward Search Experiment): is an experiment that will start collecting data during Run 3. FASER experiment is designed to search for light and extremely weakly interacting particles which the Standard Model does not describe. These particles cannot be observed in other LHC detectors. FASER detector is also designed to detect neutrinos [52].

2.3 Description of LHCb detector

The LHCb detector is designed to study heavy flavour physics at LHC and search for evidence of Physics Beyond the Standard Model [53]. It is a single-arm spectrometer with a forward angular coverage from approximately 15 mrad to 300 (vertical) / 250 (horizontal) mrad. At high energies, the $b\bar{b}$ pairs are produced mainly in the same forward or backward cone; hence the entire 4π geometry of the detector is not required. The scheme of the LHCb spectrometer is shown in Fig. 2.4.

Most detector subsystems are assembled in two halves, which allow them to move during maintenance and provide access to the beam pipe. They are referred to as A-side and C-side.

The LHCb dipole magnet generates an integrated magnetic field of about 4 Tm. During the Run 1 and 2 tracking system consisted of the VERtEX LOcator (VELO, [54]) situated around the interaction region inside a vacuum tank, four tracking stations: the Tracker Turicensis (TT, [55]) - upstream of the dipole magnet and tracking stations T1–T3 ([56], [55]) - downstream of the magnet. The charged hadron identification system consisted of two Ring Imaging Cherenkov detectors (RICH1 and RICH2, [57]). The calorimeter system ([58]) was composed of a Scintillating Pad Detector (SPD), a shashlik type electromagnetic calorimeter (ECAL), a preshower (PS) and a hadronic calorimeter (HCAL). It identified electrons, photons and hadrons as well as energies and positions of particles. At the end of the spectrometer, there were muon stations [59].

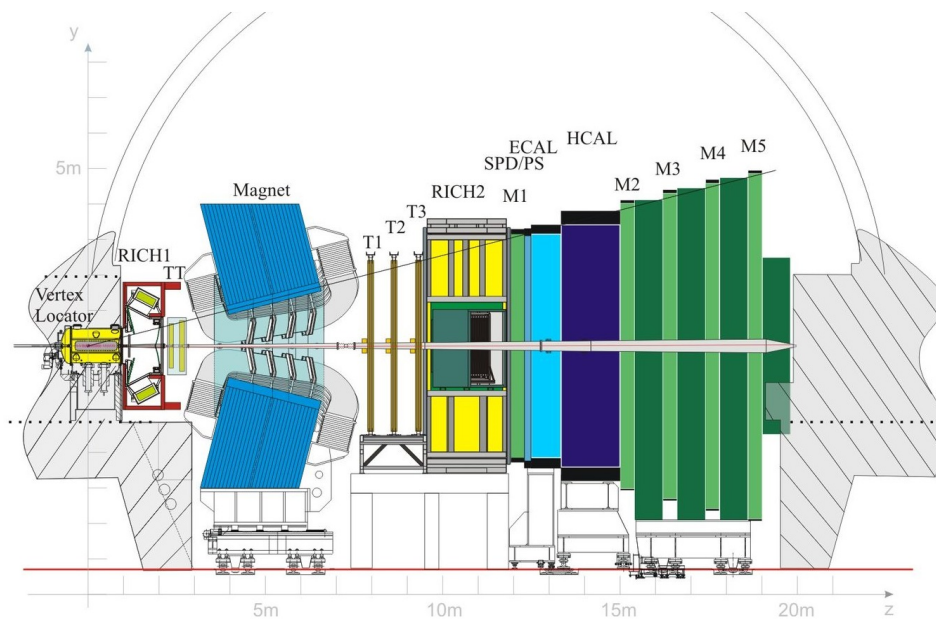


Figure 2.4: Schematic view of the Run 1 and 2 LHCb detector [48].

LHCb spectrometer covers the pseudorapidity range $2 < \eta < 5^1$ (Fig. 2.5).

Pseudorapidity is Lorentz invariant under boosts along the longitudinal axis; therefore, it is a commonly used spatial coordinate in particle physics, when cylindrical coordinate system is of interest.

2.3.1 LHC and LHCb performance

Several parameters vital for the performance of LHC and each detector operating at LHC. One of them is the pile-up, which is the average number of proton-proton interactions per bunch crossing. Its magnitude changes over time as the luminosity evolves throughout the fill². The characterisation of the pile-up level during LHC operation is critical for the experiments since the number of expected vertices depends on the pile-up. The pile-up at LHC during Run 1 and 2 varied from 1 to 40, but at lower luminosity (at experiments like LHCb and ALICE), this value was about 1-2. Beams of protons collided at the LHCb has dimension $\sigma_x \approx 17 \mu\text{m}$ and $\sigma_y \approx 17 \mu\text{m}$, $\sigma_z \approx 4 \text{cm}$ and contains 10^{11} particles [61], [62]. The instantaneous luminosity is defined by number of particles per bunch N_1, N_2 ,

¹Pseudorapidity is defined as:

$$\eta = -\ln \left[\tan \left(\frac{\theta}{2} \right) \right], \quad (2.1)$$

where θ is the angle between the particle momentum and the direction of the beam axis.

²A fill refer to a lifetime of beams in LHC from injections from SPS to end of the collisions and removing it to dumping stations.

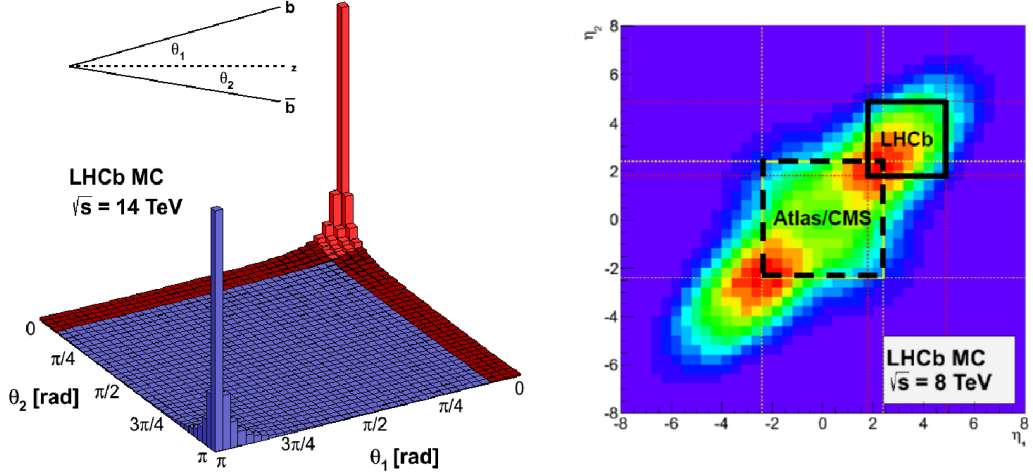


Figure 2.5: Angular distribution of $b\bar{b}$ quarks in collisions at $\sqrt{s} = 7$ TeV (left). Acceptance in the pseudorapidity plane for LHCb other LHC experiment (right) [60].

parameters of beam profile, collision of frequency f and the number of bunches N_b (Eq. 2.2).

$$\mathcal{L} = \frac{N_1 N_2}{\sigma_x \sigma_y} f N_b \quad [\text{cm}^{-2} \text{s}^{-1}] \quad (2.2)$$

Time integrated luminosity (L) becomes the proportionality factor between a number of expected events (N) during this time and respective cross-sections (σ):

$$N = L \cdot \sigma. \quad (2.3)$$

ATLAS and CMS experiments work on significantly higher instantaneous luminosity than LHCb and ALICE. Lower instantaneous luminosity reduces radiation damage to detector components and enables precise measurement of vertices and tracks. Instantaneous luminosity in LHCb spectrometer remains fixed (Fig. 2.6-bottom). The number of data collected each year strictly depends on spectrometer performance in a year of data taking. The performance of the LHCb spectrometer significantly changed whilst Run 1 and Run 2. During Run 1 (2010-2012), the nominal centre-of-mass energy was $\sqrt{s} = 7$ TeV and $\sqrt{s} = 8$ TeV for the 2011 and 2012, respectively. During Run 1, the LHCb collaboration collected a data sample of 3 fb^{-1} . During Run 2 (2015-2018), after the first long shutdown (LS1), the nominal centre-of-mass energy was increased to 13 TeV, and

the LHCb spectrometer collected data corresponding to an integrated luminosity of 6 fb^{-1} . Maximum instantaneous luminosity at LHCb was order of $10^{32} \text{ cm}^{-2}\text{s}^{-1}$ [63].

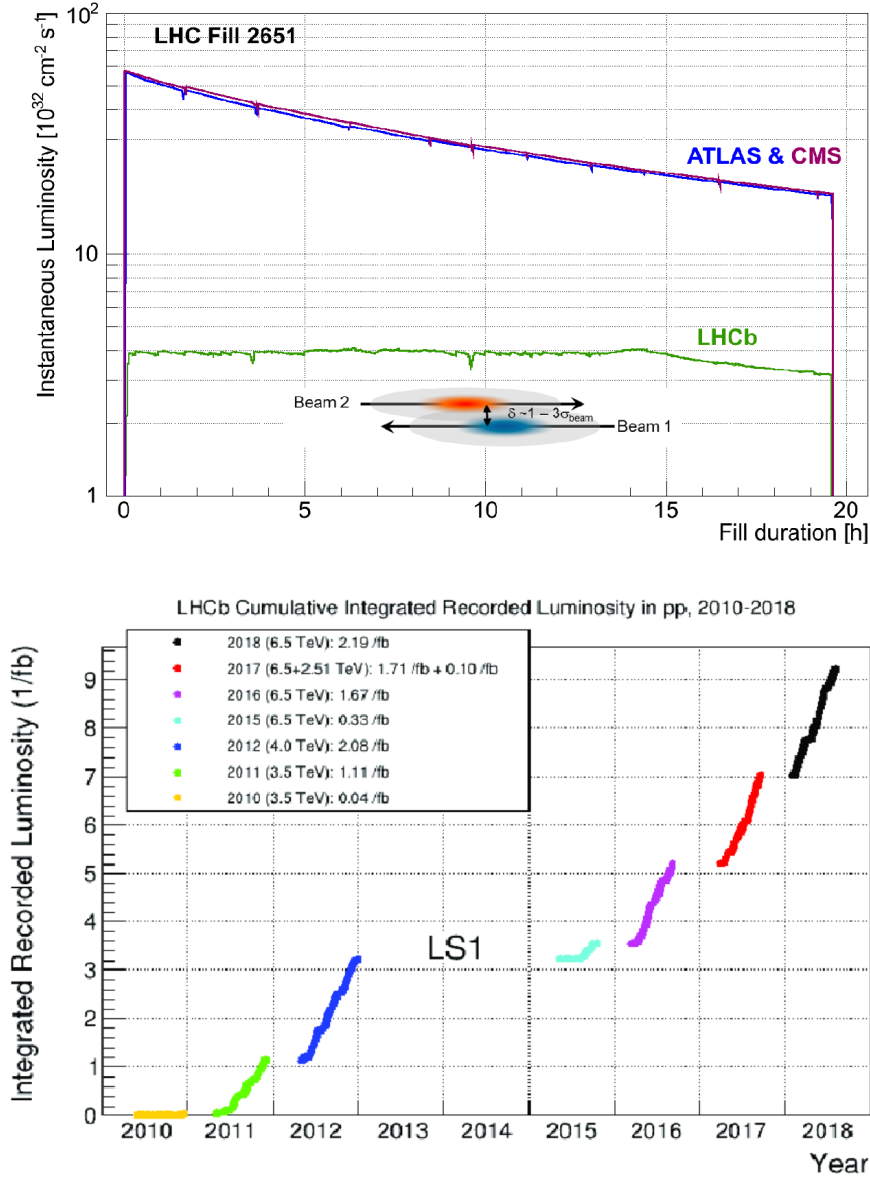


Figure 2.6: Comparison of the evolution of the instantaneous luminosity for ATLAS, CMS and LHCb during fill 2651 (top) [48]. The LHCb integrated luminosity in 2010-2018 (bottom) [63].

2.3.2 LHCb's subsystems

During the ongoing upgrade of the LHCb spectrometer [38], detectors: ST, TT, T1-T3 and VELO have been replaced by new ones to sustain higher luminosity and occupancies,

but the remaining ones will continue to operate during Run 3 and 4. The following paragraph describes the LHCb spectrometer operating during Run 1 and 2.

Fig. 2.4 shows a schematic view of the LHCb detector. The LHCb spectrometer consists of a tracking subsystem, the particle identification subsystem and muon chambers which are responsible for measuring muons.

Tracking subsystem

LHCb tracking system [64] aims at efficiently reconstruct track parameters of charged particles that go through the detector during collisions in the LHC. Tracks of charged particles in the magnetic field provided by the LHCb dipole are curved therefore measurement of this curvature allows precise measurement of particle's momentum. Tracking information is also essential to determine points where particles decay and which particles originate from the same point (vertex). The former particle tracking system (during Run 1 and Run 2) consists of the Vertex Locator (VELO), the Trigger Tracker (TT) and the three Tracking stations (T1-T3), and the dipole magnet.

VELO - Vertex Locator

The Vertex Locator has been designed to reconstruct proton-proton (pp) interaction point and decay vertex of heavy hadrons, called primary and secondary vertex respectively [54]. Moreover, the VELO allows for measuring the Impact Parameter (IP) of charged particle's trajectories³. The Run 1 and Run 2 VELO consisted of two sides of semi-circular silicon sensors, each 0.3 mm thick (Fig. 2.7). Inside, the small cutout in the sensor's centre allowed the particle beam to pass through the detector during LHC operation. Charged particles traverse the silicon and generate electron-hole pairs, and then these generated charges are collected by the detector readout system. Finally, an analogue signal is converted into a digital signal. During physics data-taking, the silicon sensors have positioned around the LHC beam at a distance of 8 mm. Before data taking, VELO halves remained open to prevent the interference with the beam adjusting procedures. The whole VELO system was placed inside the secondary vacuum, the sensors were separated from the primary beam vacuum by Radiation-Frequency (RF) foil - a thin aluminium layer. The VELO detector was composed of two types of sensors; the first type was called R-type, which was dedicated to measuring r -coordinate

³The Impact Parameter is defined as a transverse distance of the closest approach between a particle trajectory and a vertex.

- distance from the proton beam, and the ϕ -type sensors measured the azimuth angle. The strip pitch varies from $38\ \mu\text{m}$ at the innermost region to $102\ \mu\text{m}$ at the edge of the sensor. To mitigate adverse effects of radiation damage caused by a high radiation dose, the cooling system, based on CO_2 , cooled all sensors and readout electronics. During data taking, the VELO sensor's operational temperature was around -8°C . The readout of the data from sensors was performed by the Beetle front-end ASIC [65].

TT - The Tracker Turicensis

The second silicon tracking detector (TT) was located before the dipole magnet [55]. Information from TT was crucial in reconstructing low-momentum long-lived tracks as neutral K_S^0 mesons that decay mostly outside the VELO detector. A long-lived K_S^0 travels up to several centimetres before decaying to pions [2]. TT consisted of two stations called TTa and TTb, four planes denoted as TTaX, TTaU, TTbV, and TTbX (Fig. 2.8). The X planes were positioned perpendicular to the beam pipe with strips along the LHCb y-axis. The U and V stations were also positioned perpendicularly to the beam pipe but their strips featured, so called, stereo angle tilt by -5° and $+5^\circ$, respectively and covered a rectangular area $150\ \text{cm}$ wide and $120\ \text{cm}$ in height. Silicon microstrip sensors constitute the total active area, around $8.4\ \text{m}^2$. The spatial resolution was about $50\ \mu\text{m}$. Layers were arranged in pairs, separated about $27\ \text{cm}$ in the z direction. The distance between planes TTaX and TTaU, as well as TTbV and TTbX, was around $4\ \text{cm}$ and allowed to reconstruct one spatial point by combining 1-D measurements. The TT silicon sensors were $500\ \mu\text{m}$ thick with a strip pitch of $183\ \mu\text{m}$. TT operated during Run 1 and 2 and is substituted by a new silicon UT detector for Run 3 and 4.

The Inner and Outer Tracker

Set of three tracking stations (T1-T3) was situated behind the magnet. These sub-detectors were removed after Run 2 and replaced by the new Fibre Tracker detector. The former detector was divided into two parts: Inner (IT [55]) and Outer (OT [56]) Tracker. The inner part of the TT stations (IT) covered the acceptance region close to the beampipe, where the density of reconstructed particles is the highest; therefore, it was designed in silicon strip technology. The strip pitch was around $198\ \mu\text{m}$, and the detector's active area was approximately $11\ \text{m}^2$. The outer part of the TT stations (OT) is composed of a drift-time detector. It provided acceptance coverage in the outer region of the tracking stations. Each module was built with drift tubes with diameters of about

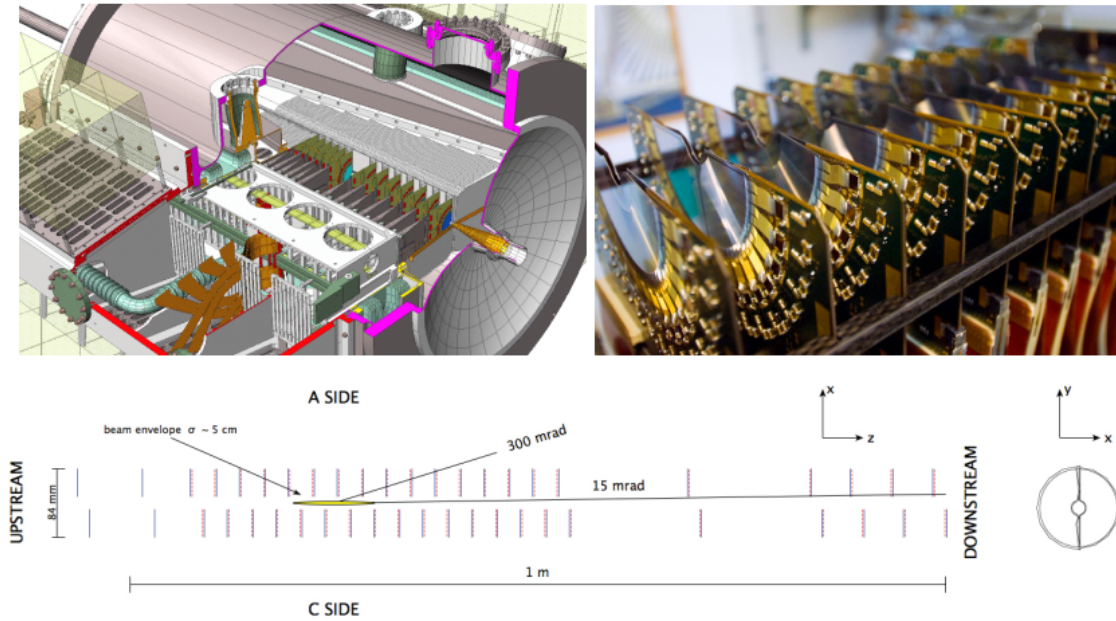


Figure 2.7: The LHCb VELO vacuum tank (top right). A photograph of one side of the VELO during assembly showing the silicon sensors and readout hybrids (top left) [66]. Cross-section in the xz plane at $y = 0$ of the sensors and a view of the sensors in the xy plane (bottom) [67]. The detector is shown in its closed position. R/ϕ sensors are shown with solid blue/dashed red lines. The modules at positive (negative) x are known as the left or A-side (right or C-side).

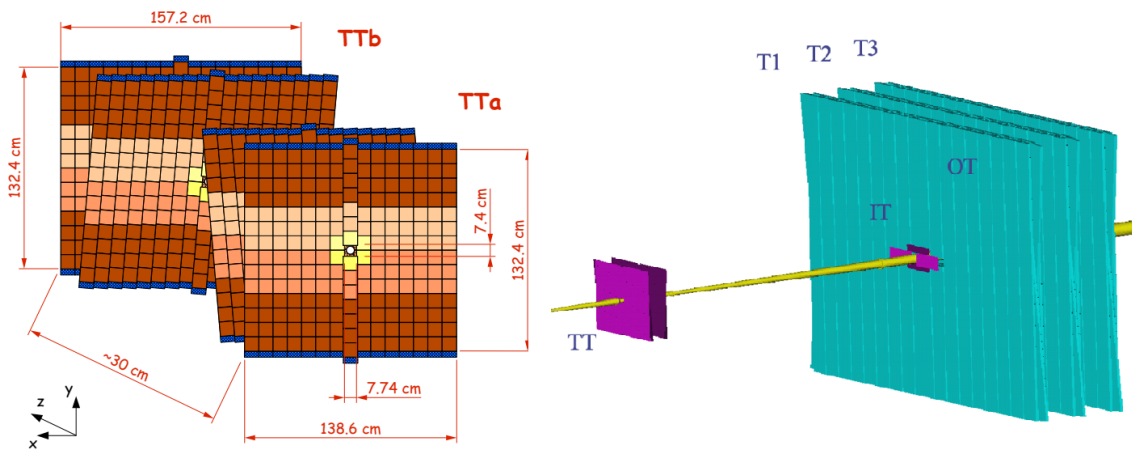


Figure 2.8: The TT, detectors schematic view (left). The T1-T3 schematic view (right) [68].

5 mm and was filled with argon (70%) and CO_2 (30%). The drift times were below 50 ns. The largest station covered a sensitive area of $600 \text{ cm} \times 490 \text{ cm}$. The distance of the

closest approach of the particle to the anode wire was used to measure the particle's position. It gave a $200\ \mu\text{m}$ resolution and a hit efficiency of more than 99%.

The LHCb magnet

Measuring the momentum of charged particles that pass through the detector requires a magnetic field. The LHCb dipole (Fig. 2.9) is a warm-type magnet design with saddle-shaped coils in a window-frame yoke with sloping poles to match the required detector acceptance [69]. The total weight of the yoke is 1500 tons, and the two coils are 54 tons. The integrated magnetic field of the LHCb dipole is 4 Tm. The unusual shape of the LHCb magnet is owed to the RICH detector constraint (field $< 2\ \text{mT}$ inside RICH) and maximising a field in the tracking subsystem. 100 mm thick plates were used to form the identical horizontal bottom and top parts and the magnet yoke's two mirror-symmetrical vertical parts (uprights). The two identical coils with conical saddle shapes are placed mirror-symmetrically. Each coil consists of fifteen *pancakes* made from a hollow aluminium conductor.

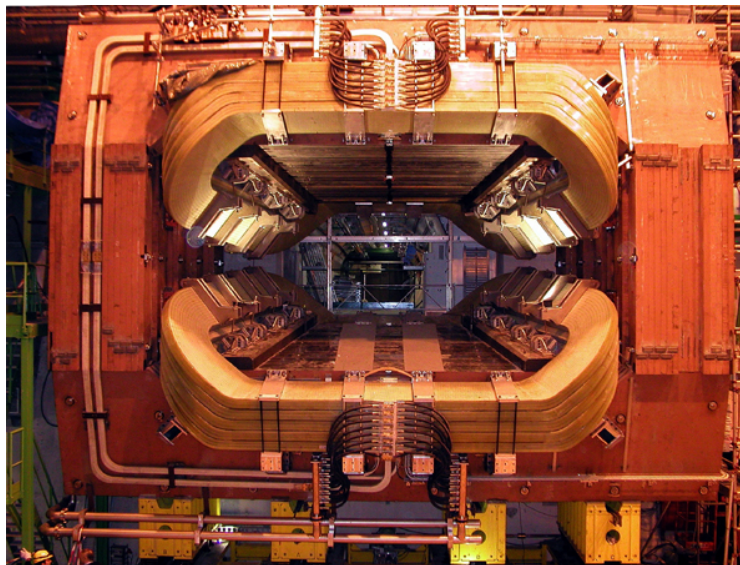


Figure 2.9: The LHCb dipole [70].

Particle identification subsystem

Analysis of complicated B meson decays involves the identification of hadronic states, including kaons, pions, photons and muons. In the LHCb spectrometer, the particle identification subsystem consists of RICH 1, and RICH 2 detectors [57]. The RICH

detector's performance is based on the correlation between momentum and polar angle, with the high-momentum particles produced predominantly at low polar angles [57].

RICH detectors use the light emitted by a charged particle passing detector material with a velocity greater than the speed of light in that material. It is the Cherenkov radiation effect. Photons are emitted into a cone defined as:

$$\cos(\theta) = \frac{c}{nv}, \quad (2.4)$$

in reference to the propagation direction, n is the refraction index of the detector material. For particles which travel with a velocity close to the speed of light, the Cherenkov angle is calculated using only the refraction index:

$$\cos(\theta) \approx \frac{1}{n} \quad \beta \rightarrow 1. \quad (2.5)$$

RICH 1 covers the low and intermediate momentum region of 2 - 40 GeV/ c , while RICH 2 covers the high-momentum region 15–100 GeV/ c . RICH 1 is placed as close as possible to the interaction region to increase the acceptance of the detector. RICH 1 and 2 detectors have a similar optical system, consisting of a spherical focusing mirror and flat mirrors. The spherical mirrors of RICH 1 are constructed in four quadrants, with a carbon-fibre structure, while those of RICH 2 (56 segments) are flat mirrors.

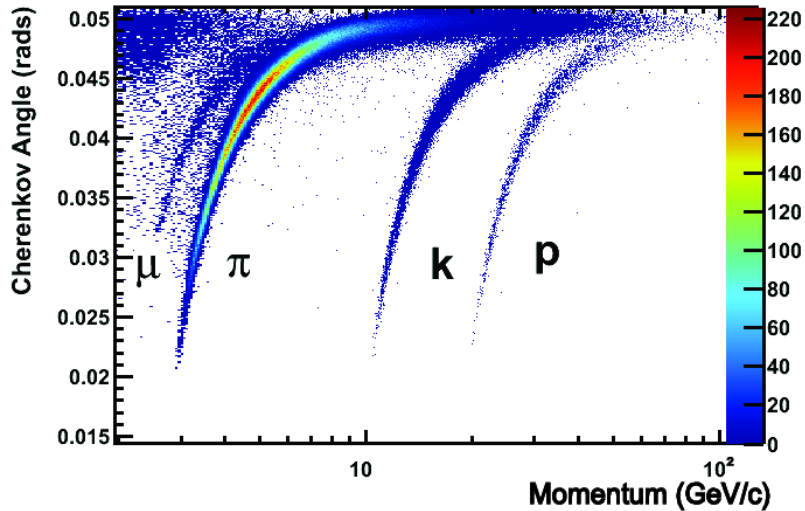


Figure 2.10: Reconstructed Cherenkov angle as a function of track momentum in the C_4F_{10} radiator (simulation, [71]).

The reconstructed Cherenkov angle for the simulation sample is shown in Fig. 2.10.

Calo subsystem

The calorimeter system plays a key role in identifying neutral particles that pass through the detector. As neutral particles are not bent in the magnetic field nor emit Cherenkov light, their identification can be done exclusively in calorimeters. The calorimeter system measures the amount of particle's energy by stopping them as they pass through the detector. LHCb exploits two types of the calorimeter systems. The electromagnetic calorimeter (ECAL) measures electrons and photon's energy. In contrast, the hadron calorimeter (HCAL) measures the energy of protons, neutrons, and other particles containing quarks (Fig. 2.11).

The Scintillating Pad Detector (SPD) and LHCb Preshower (PS) are placed before the ECAL, and the PS is placed after the SPD. Both of them consist of scintillating pads. Between them, there is a 15 mm lead absorber (around 2.5 radiation lengths for electrons, choice of the lead thickness is a compromise between trigger performance and energy resolution [72]). The SPD interact with charged particles. The lead absorber creates a shower after interaction with neutral particles. Since the shower consists of electrons and photons, the PS signal is significantly larger than for pions. SPD and PS identify electrons which allow for differing them from π^0 (Fig. 2.11).

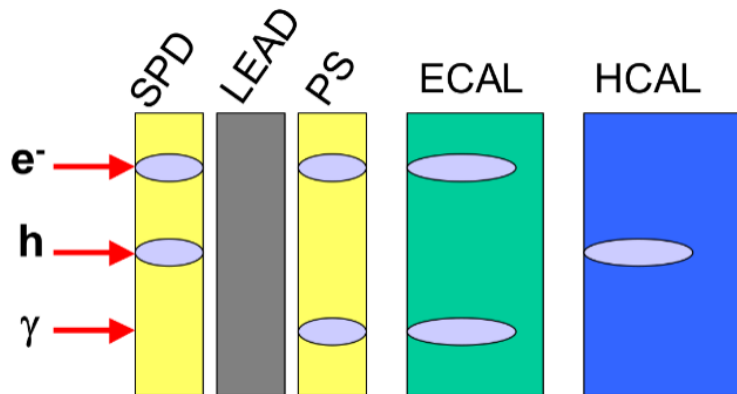


Figure 2.11: Signal deposited on SPD, PS, ECAL and HCAL by an electron, a hadron, and a photon [73].

The SPD/PS detector consists of two almost identical planes of rectangular scintillator pads with 12032 readout channels (Fig. 2.12). The detector planes are divided vertically into halves (this design allows for service and maintenance). Each PS and SPD plane is divided into the inner, middle and outer regions. Each region is composed of 3072, 3584

and 5376 cells, respectively. The detector's active area is 7.6 m wide and 6.2 m high.

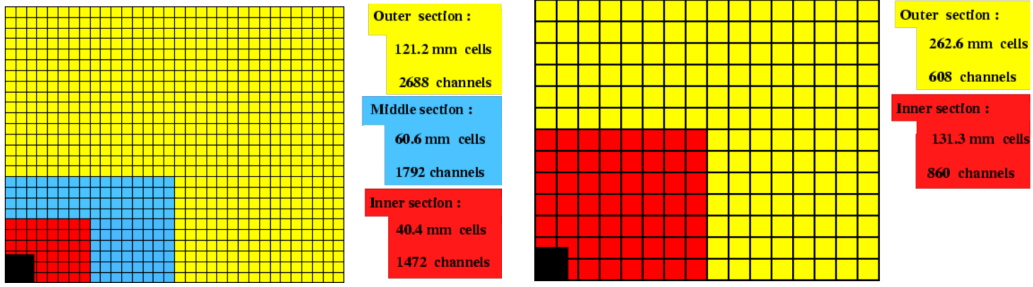


Figure 2.12: Scheme of segmentation of the SPD/PS and ECAL (left) and the HCAL (right). One-quarter of the detector's front face is shown [48].

Each plate comprises the 4 mm thick scintillator tiles and 2 mm lead plates. This design provide energy energy resolution of $(8\% \div 10\%)\sqrt{E} \oplus 0.9/GeV$ [72]. The HCAL comprises 4 mm thick scintillator tiles sandwiched between 16 mm iron sheets. The HCAL resolution is $69\sqrt{E} \oplus 9/GeV$ [72].

Muon subsystem

During Run 1 and 2, the muon detector, like the calorimeters, was designed to provide a fast measurement of muon's momentum and identification for L0 trigger [59]. The muon detector comprises five rectangular stations (M1–M5) covering a combined area of 435 m², placed along the beam axis. Each muon station consists of two halves, called A and C sides which facilitates service and maintenance. The first station (M1) is placed before the calorimeter system, which improves the transverse momentum measurement in the trigger. The M2 - M5 stations are alternated with 80 cm thick iron absorbers. Absorber allows selecting muons by stopping any other particles. The total absorbers thickness (calorimeters and muon station) corresponds to approximately 20 interaction lengths. Each station is divided into R1-R4 regions; all but R1M1 stations use multiwire proportional chamber detectors (276, filled with carbon dioxide, argon, and tetrafluoromethane). Because of the high particle density, the R1M1 uses triple gas electron multiplier detectors (12 GEM detectors). The muon detector and station design are shown in Fig. 2.13.

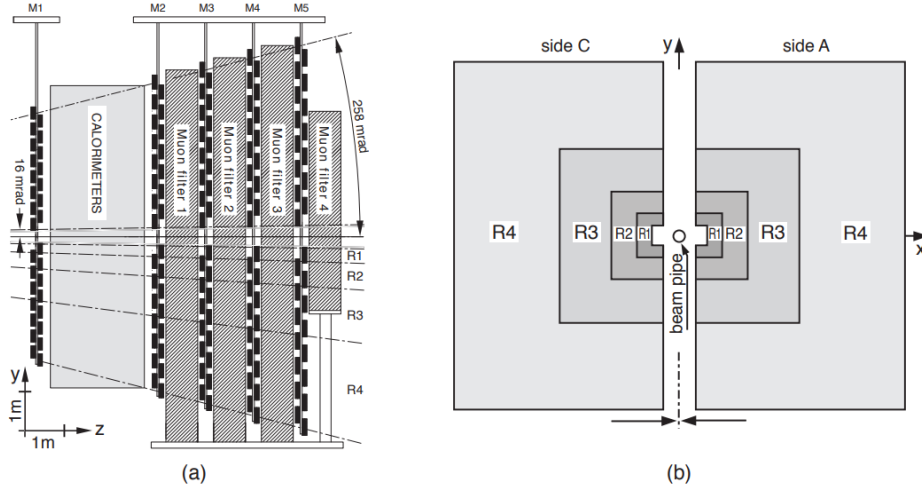


Figure 2.13: Side view of the muon detector (left), station layout of the muon detector (right) [74].

Trigger

The number of particles produced in pp interactions at LHC is too large to reconstruct and record them all on the data storage. A dedicated subsystem, trigger, performs a selection of candidates for interesting physical processes [75]. Trigger benefits from properties of B hadrons which have relatively long lifetime. As a result, primary vertex and secondary vertex (B meson decay point) can be distinguished by the trigger system on different levels performing event by event selection.

The Run 1 and 2 trigger system was built to reduce the event rate to 12.5 kHz (achieved in Run 2). The trigger was composed of two levels: the Level-0 trigger (L0), implemented with the hardware components, and the High-Level Trigger (HLT), a two-stage software trigger executed on event filter CPU farms. Two primary tasks of the HLT were to confirm the L0 decisions and perform the event reconstruction (Fig. 2.14).

The High-Level Trigger (HLT) was software-based and was divided into two stages, HLT1 and HLT2. HLT1 performed an inclusive selection of events based on track signatures, the presence of muon tracks displaced from the PVs, or dimuon combinations. L0 combined the information from calorimeters and the muon system and selected only candidates with high p_T or high transverse energy. Events that passed the HLT1 requirements were buffered (deferred) on disk storage. They awaited further selection during LHC inactivity: long shutdown, technical shutdown, and time between fills when the maximum CPU power of LHCb is available.

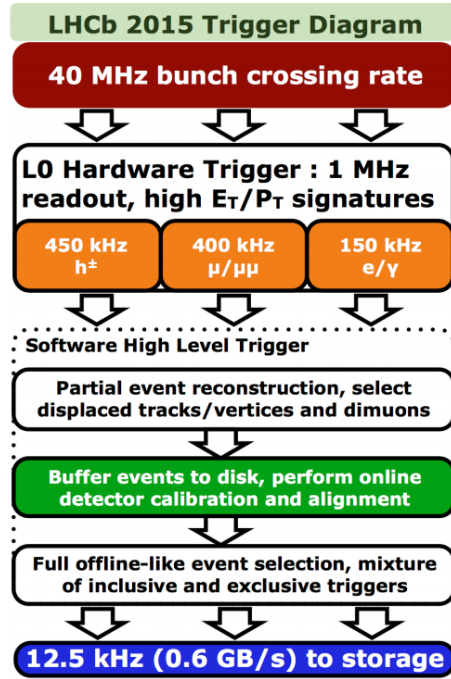


Figure 2.14: Simplified model of data processing in Run 2 trigger system [75].

Reconstruction of tracks at LHCb

There are several types of tracks reconstructed at LHCb [76]. A track type depends on detectors where a particle is registered. Long tracks, were defined as those traversing the entire tracking system, which resulted in the most precise momentum resolution. Upstream tracks passed only through the VELO and TT. Downstream tracks traversed only through TT detectors and T stations. These tracks originated from long-lived composite particles like K_s^0 or Λ . Because these tracks did not pass through VELO, their momentum resolution is significantly lower than for long tracks. The VELO tracks contain VELO hits only. Because of the acceptance of the LHCb, only backward tracks and tracks with larger polar angles are generally categorised as VELO tracks. T tracks were reconstructed by T stations only. Reconstructing momentum was impossible because they do not traverse the magnetic field. These tracks are used at LHCb for a special purposes like primary vertex reconstruction or veto. Detector's hits are converted into the track using sophisticated pattern recognition algorithms (including Hough transform technique) and then fitted with the Kalman filter. The quality of the track is measured using χ^2 per degree of freedom of the fit [77]. Visualisation of tracks reconstructed at LHCb is shown in Fig. 2.15.

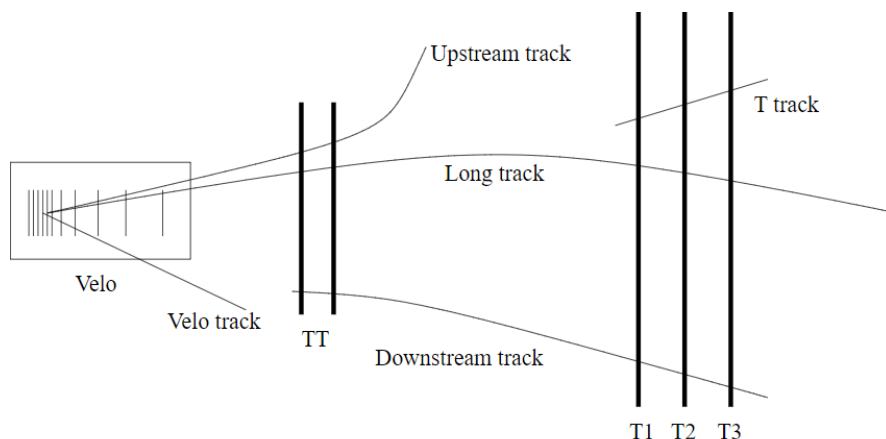


Figure 2.15: Visualisation of track types reconstructed at LHCb [78].

The LHCb data flow

Several offline subsystems were designed to reconstruct events, store data and prevailing only an amount of interesting events. The main components of the offline system during Run 1 and 2 were (Fig. 2.16):

1. Trigger: data from the detector were filtered through L0 - hardware trigger and the HLT - software trigger. The application which was executed on the online filter farm (implementation of the HLT trigger) is called Moore [79];
2. Reconstruction: the reconstruction procedure transform hits into clusters and tracks. The Brunel application handles it [80]. Data are stored in the RAW Zero-Suppressed format;
3. Stripping: each stripping line is associated with a several selection criteria that allow for reducing combinatorial background in the early stage of analysis. The candidates are categorised into families of processes (charm physics, beauty physics, exotic particles and more) which demonstrate similar properties [81].

In addition, simulated events could be processed by the same software that performed the reconstruction and selection algorithms on collision data. An essential step that made it possible was detector readout emulation that allowed to encapsulate the simulated data into the transport structures used by the LHCb event builder system. It provided an identical structure of simulated events as for real data. There are several purposes for applying simulated events in physics analyses at LHCb:

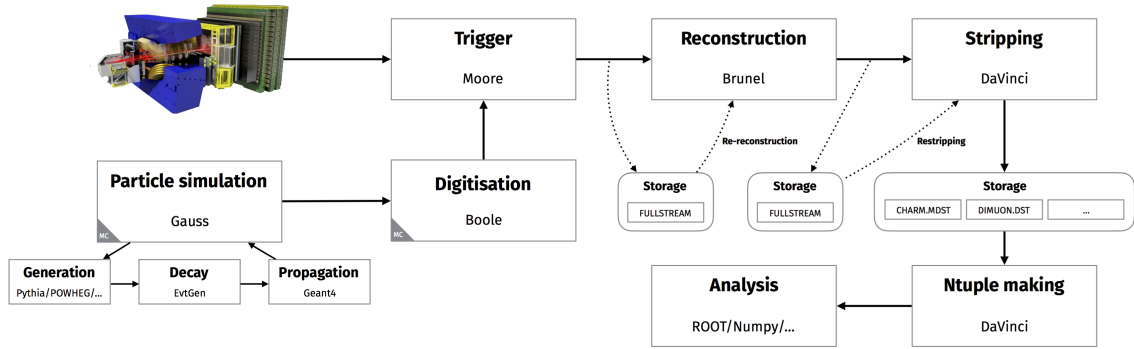


Figure 2.16: The LHCb data flow [82].

1. Studies of the feasibility of studies at LHCb (detector acceptance);
2. Training multivariate intelligent algorithms (MVA);
3. Calculation of probability density functions to describe the invariant-mass spectra of signal and background components;
4. Calculation of efficiencies (selection, identification and more).

It is worth mentioning that the overall architecture of the data processing, from the software point of view, has been retained and is being used for Run 3 and 4, with necessary upgrades.

At LHCb, the Gauss application control generation process uses several generators. The Pythia [83] generator simulates proton-proton collisions and $b\bar{b}$ pairs. The EventGen is used in the simulation of B decays. The Geant4 simulates the interactions of the particles with the detector [84].

2.3.3 Modernisation of tracking system during LS2

The LHCb results based on data collected during both Run 1 and Run 2 showed its discovery potential and the leading role of the LHCb among the flavour physics experiments. The SM was confirmed but searches for New Physics BSM [85] are ongoing. Studies of the most interesting and rare processes require large data samples, which can be achieved since LHC is currently in the upgrade phase [38], but obtained with the same precision as before.

In the first phase of the upgrade, the LHCb experiment will operate at the maximum instantaneous luminosity higher by a factor of 7.5 with respect to Run 2 ($\mathcal{L} = 2 \times$

$10^{33} \text{ cm}^{-2}\text{s}^{-1}$) with proton collisions at LHC centre-of-mass energy $\sqrt{s} = 13.8 \text{ TeV}$. Each LHC experiment, including LHCb, had to be prepared to deal with a larger number of collisions and significantly larger particle fluence. Many other requirements, including new front-end electronics and a flexible full software trigger designed to read out the whole detector every 25 ns had to be fulfilled. The upgraded LHCb detector (Fig. 2.17) is conceived to collect data corresponding to the integrated luminosity of at least 50 fb^{-1} during Run 3 and 4, which requires a completely new tracking system. The following paragraph describes Upgrade 1 of the LHCb spectrometer briefly. The details of Upstream Tracker have discussed in Sec. 3.

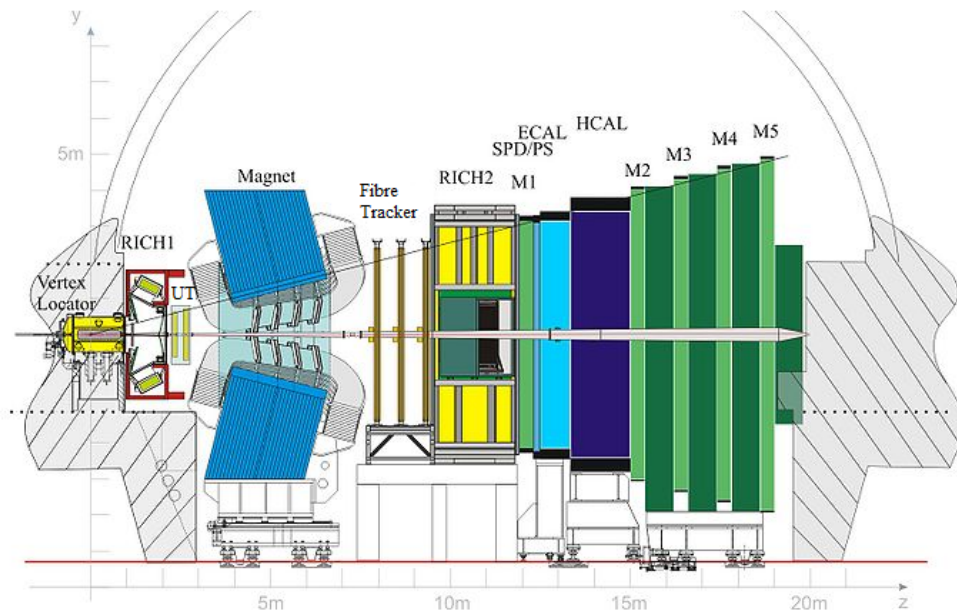


Figure 2.17: Schematic view of the LHCb upgrade detector with location of future UT and Fibre Tracker detectors (taken from [86] with modifications).

Trigger

To meet the LHCb requirements at increased luminosity during Run 3 and 4, the L0 hardware-based trigger was removed, and HLT will perform a full reconstruction of events at 30 MHz event rate (Fig. 2.18). Using the particle identification and tracks reconstructed in the real-time, the rate will be reduced to 20-100 kHz. Another purpose of the new trigger is to increase the hadronic channel's triggering efficiency by the factor of 2 to 4 with respect to Run 1. Expected hadronic yield with this efficiency will increase

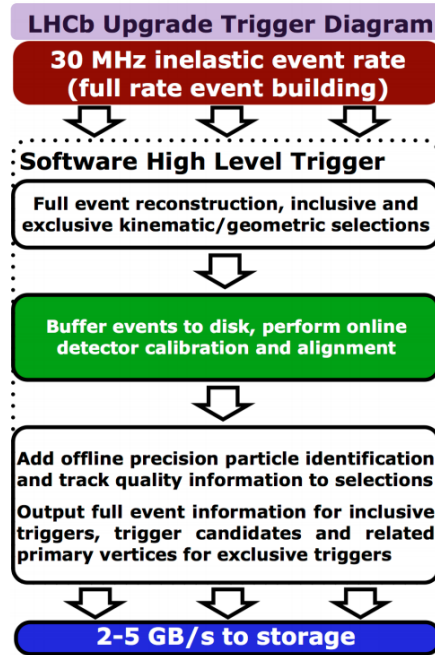


Figure 2.18: Simplified model of data processing in Run 3 trigger system [87].

by the factor of 10 to 20. All available information will be sent to the CPU/GPU farm, and event builder software on the surface by optical links [87]-[88].

VeloPix

The pixel sensor readout chip designed for the upgraded VELO is the VeloPix ASIC [89]. Each new pixel sensor is readout by three such ASICs with the individually tuned binary readout channels. The upgraded VELO will consist of 208 sensors mounted on 26 stations along the parallel axis to the proton beams, similar to the old VELO structure. Thus, the detector's total number of channels will amount to approximately 42 million, 200 times more than in the old VELO, where the corresponding number was just over 172000. Besides the enhanced planar resolution, the full event's nominal readout frequency will be 40 MHz, with the innermost sensors closer to the proton collision region than before (5.1 mm comparing to 8 mm for the strip detector). Design of the VeloPix detector is shown on Fig. 2.19 (a).

Fibre Tracker

The Fibre Tracker [90] consists of three stations (T1, T2, T3) each with four detection planes, as shown in Fig. 2.19 (c). There are eight fibre mats in each module of the

detector with a length of 2.4 m as active detector material. The fibre mats consist of 6 layers of densely packed blue-emitting scintillating fibres with a diameter of $250\ \mu\text{m}$. The scintillation light is recorded with multi-channel silicon photo-multipliers, and processed data are sent via optical links to the DAQ system. To reduce the noise of the silicon photo-multipliers (up to $10^{12}\ \frac{\text{neq}}{\text{cm}^2}$), the SiPM is mounted in cold boxes and cooled down by titanium cold-bars to $-40\ \text{°C}$. The detector is designed to provide a hit efficiency of 99% and a resolution better than $100\ \mu\text{m}$.

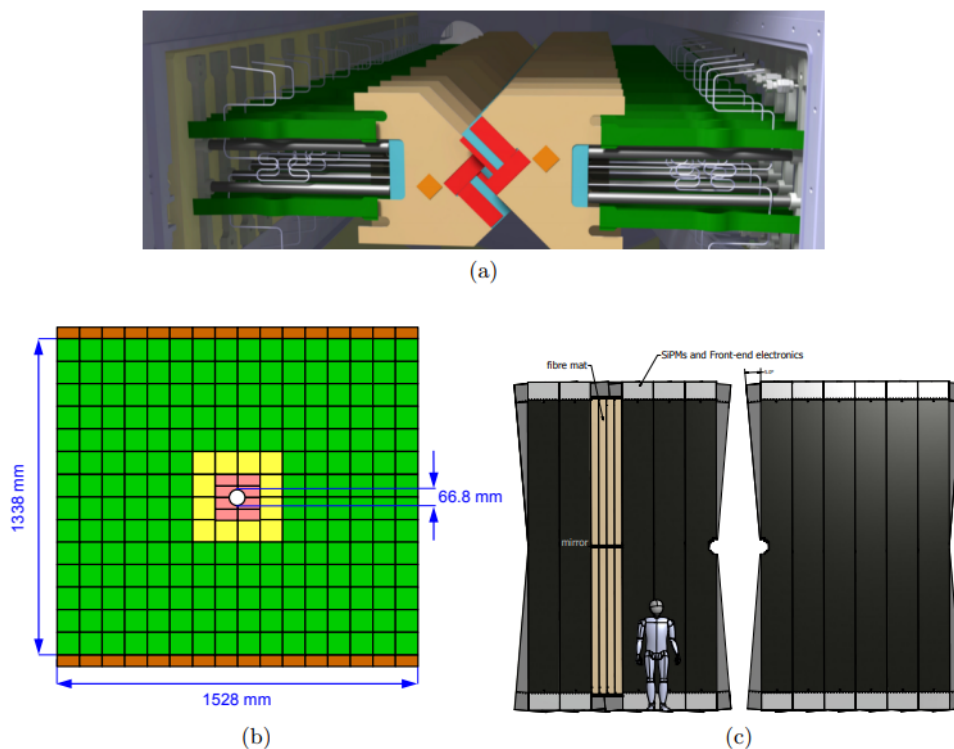


Figure 2.19: Sketches of the upgraded LHCb trackers: VELO (a), UT (b) and SciFi (c) [91].

Upstream Tracker

The Upstream Tracker (UT) will be used to reconstruct downstream tracks of long-lived particles decaying beyond the VELO detector [90] and to provide an intermediate measurements for the long tracks. The UT detector consists of four silicon planes (Fig. 2.19 (b)), each about $1.5\ \text{m} \times 1.3\ \text{m}$. They are composed of 1.5 m staves tiled with around $10\ \text{cm} \times 10\ \text{cm}$ silicon wafers mounted on opposite sides of the stave to ensure no gaps (for the same purpose, staves are also overlapped). The size of sensors installed on the

staves has an approximate size of pitch: $190 \mu\text{m}$ at the detector's outer region and $95 \mu\text{m}$ at the inner region. Since, one of the topic of this thesis is directly related to the UT development and commissioning a more detailed description of the detector can be found in Sec. 3.

Chapter 3

Upstream Tracker

The Upstream Tracker (UT) detector is designed to replace Run 1 and Run 2 tracking detector - TT. The following chapter emphasises several aspects of the construction of UT detector, its readout system, and its maintenance.

3.1 Motivation and requirements

Long-lived particle decays, which predominantly occur outside the VELO, contribute to many physics analyses at the LHCb. During Run 1 and 2, the TT hits were required in the reconstruction of tracks associated with these particles. The types of tracks reconstructed during Run 1 and 2 are detailed in Sec. 2.3.2. Fig. 3.1 shows that in the case of $B^0 \rightarrow J/\psi K_S^0$ studies, most of the events ($\sim 70\%$), were reconstructed from the downstream track and TT hits. For this decay channel, TT hits reduced the background events rate from 30% to 17%. Moreover, TT hits significantly improved the momentum resolution. Fig. 3.2 shows the impact of TT tracks in the analysis, including di-muon pairs, where the resolution was improved by $\sim 25\%$ [91]. Another issue related to the reconstruction of tracks at LHCb is *ghost tracks*. Tracks in LHCb have distant segments between the VELO and the downstream tracker. Despite the overall excellent performance, there is a substantial possibility of mismatching these segments, which are 7 m apart, what might result in creating of false tracks called ghost tracks. These tracks are significantly reduced when the extrapolated hits at the TT match real hits.

The UT design must fulfil performance requirements, which should be met throughout the detector operation. The integrated luminosity expected after Run 3 and 4 is at least 50 fb^{-1} . Hence, the degradation of the system's performance after extensive irradiation

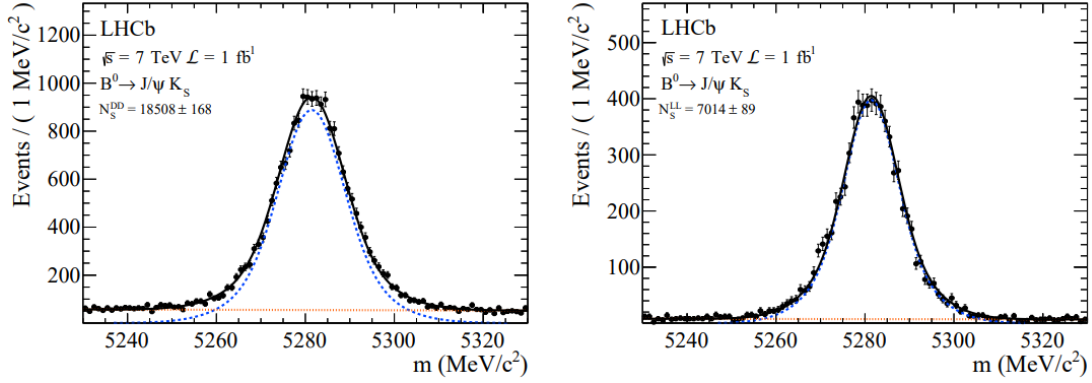


Figure 3.1: The invariant $J/\psi K_S^0$ mass for candidates reconstructed using only the TT and downstream tracker (left), and using the VELO and the downstream tracker, including TT hits if they exist with the fit to distribution (right, the red dotted lines show the background, the blue dashed lines the signal)[91].

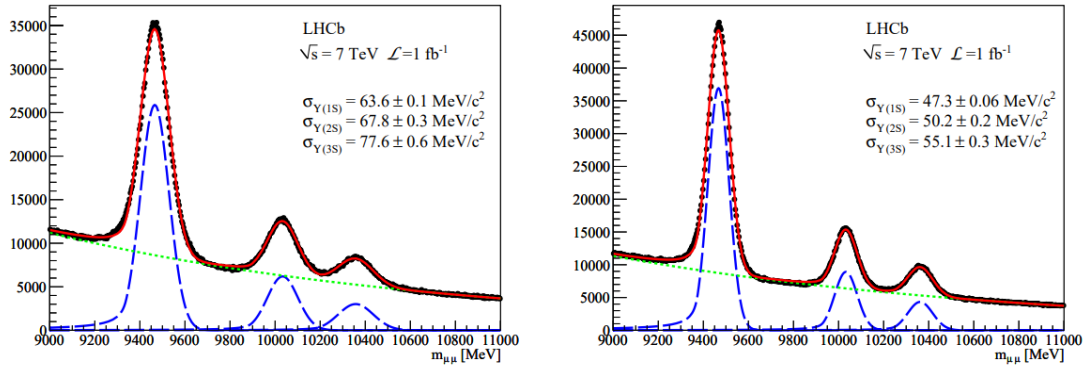


Figure 3.2: The invariant $\mu^+\mu^-$ mass for candidates reconstructed without TT hits (left) and candidates with both tracks having TT hits with the fit to the distribution (right, the green dotted line shows the background, the blue dashed line the signals) [91].

of its innermost components must be considered. Moreover, specific requirements refer to the detector's geometry and material budget constraints. The new detector's aims at:

- providing the electronics readout adjusted to LHC 40 MHz clock, able to perform on-detector data processing, up to the hit detection and zero-suppression,
- improving the design of the inner region capable to sustain high particle's fluence and with increased acceptance comparing to Run 1 and 2 design,
- removing any gaps in detector geometry (which occur in TT detector),
- attaining at least 99% single hit efficiency.

Furthermore, a similar requirement as for TT will be made for UT detectors where tracks will need to match at least 3 of 4 UT plains in order to reduce the number of ghost tracks.

3.2 SALT

For the UT detector - the project of a novel 128-channel ASIC - SALT (Silicon ASIC for LHCb Tracking), was developed by the LHCb group at AGH University of Science and Technology in Krakow [92]. The SALT chip's purpose is to convert analogue signals from the sensor, perform advanced digital processing and prepare the output data for the serialisation. The chip is made in TSMC CMOS 130 nm technology, designed to readout data from 128 channels simultaneously. The sophisticated analogue part of SALT is also responsible for fast signal conditioning. After the analogue part, the signal is digitalized by 6-bits ADC. To deal with 40 MHz LHC bunch crossings, the front-end of SALT comprises a charge preamplifier and a fast shaper ($T_{peak} = 25$ ns) required to distinguish between the LHC bunch crossings at 40 MHz. To synchronize the ADC sampling instance with beam collisions, an ultra-low-power (< 1 mW) Delay-Locked Loop (DLL) is used to shift and align an external clock.

The ADC output is processed by a Digital Signal Processing (DSP) block, which implements a number of algorithms, including pedestal subtraction, common mode subtraction (CMS) and a zero suppression (ZS). The DSP procedure cannot be too complicated due to power limitations. After the DSP, the data, with additional header information are placed into a buffer and transmitted using serial links to the event builder. Two systems control the ASIC: the Timing and Fast Control (TFC) and the Experiment Control System (ECS). The processing chain is presented in Fig. 3.3.

3.3 Stave

Each UT plane is constructed with vertical structures, called *staves*. Staves are approximately 1.6 m long and 10 cm wide and are mounted vertically [91]. The stave comprises 14 or 16 silicon sensors and read-out ASICs attached to a hybrid flex. The hybrid flex is about 220 μm thick with the same width as the sensor. The stave structure is shown in Fig. 3.4. The hybrids are mounted on both sides of the stave support with a spatial overlap of 2 mm in y .

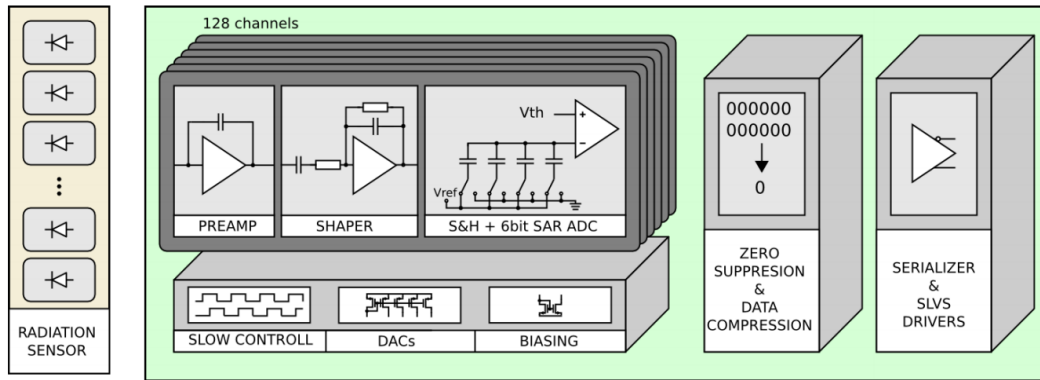


Figure 3.3: SALT block diagram [92].

The sensors send signals via data flex cables. Similarly, power cables provide power supply for the sensors and electronics equipment. The structure includes also the cooling tube to remove heat from the stave's components. The cables between the stave support and the hybrids carry power, ground, and data. The cables extend from the read-out edge of the innermost hybrids to the end of the stave, where connections are made to peripheral electronics (PEPI). The design of each UT plain provides overlaps, ensuring full sensor coverage and no gaps in a plane perpendicular to the beam axis.

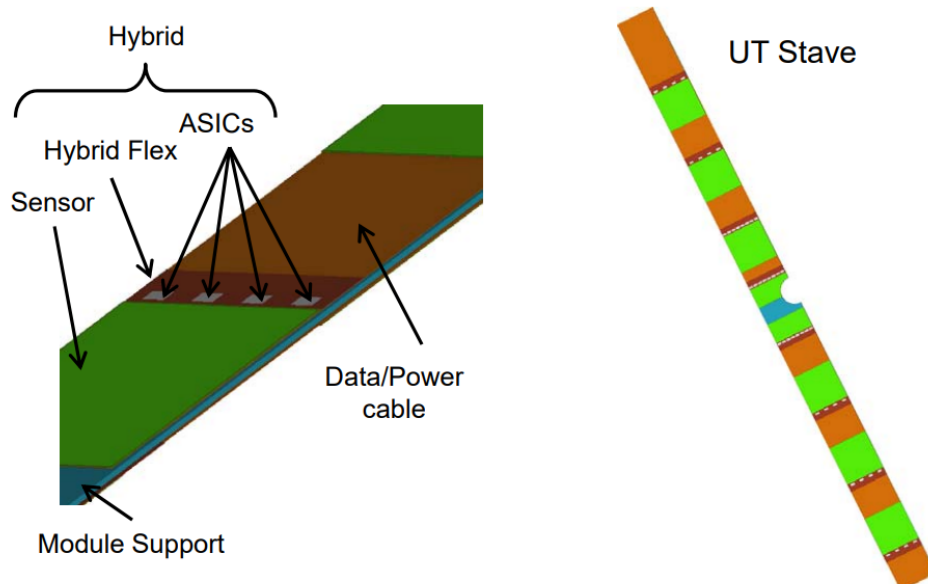


Figure 3.4: UT stave structure: UT hybrid has silicon strip sensor (left), read-out ASICs attached to hybrid flex, (right) [91].

3.4 Sensor

UT sensors are single-sided silicon micro-strip devices designed to work in highly irradiation environment. Expected fast hadron fluence, proportional to the integrated luminosity during Run 3 and 4 (50 fb^{-1}), estimated by thorough simulation studies, amounts to approximately $5 \times 10^{14} \text{ neq/cm}^2$ at the inner region of the silicon sensors. The predicted fluence distribution is highly non-linear and rapidly decreases with the distance from the LHC beam axis (Fig. 3.5).

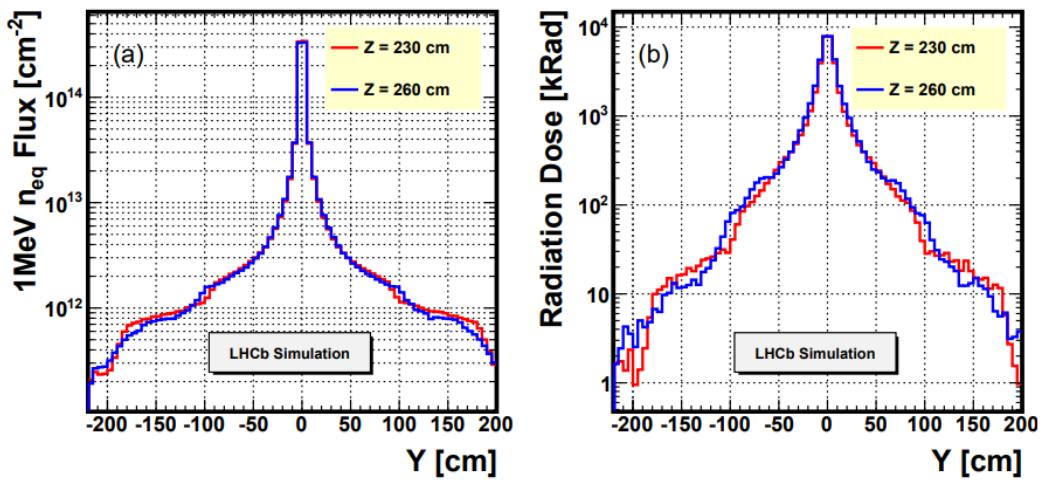


Figure 3.5: Expected fluency profile (left) and dose profile (right) after 50 fb^{-1} of total integrated luminosity as a function of the vertical position, [91].

Four types of sensors have been designed to fulfil the requirements for each detector region. Different types allow for including detector geometry effects like LHC beam and different higher occupancy in the inner region of the detector, which require more ASICs. The B-type, C-type and D-type sensors, which work in the inner region at a close distance to the beam, are designed in n^+ -in-p technology, called p-type. A-type sensors are designed to work in the outer area of the detector, where expected radiation is relatively low and work in different p^+ -in-n technology called n-type (Fig. 3.6). The thickness of the sensors is $320 \mu\text{m}$ (A sensors) or $250 \mu\text{m}$ (B, C, D sensors). Physical properties of sensors are described in Tab. 3.1.

The interconnection structures between strips and ASICs, called pitch adaptors, are integrated directly into the sensor structure. This is one of the major innovation related to the UT sensor design.

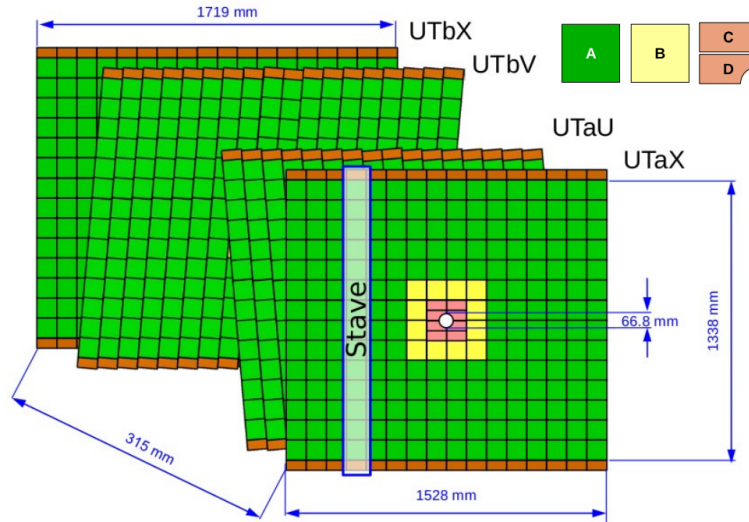


Figure 3.6: The UT detector scheme with an indication of the position of all types of sensors [91].

	B (C,D) type	A type
Thickness	250 μm	250 μm
Length of strip	98 (49) mm	98 mm
Number of strips	1024	512
Strip pitch	95 μm	190 μm
Number of sensors	1024 (1024)	512

Table 3.1: Physical parameters of each type of UT sensor.

3.5 Hybrid

The front-end electronics (SALT ASICs) is mounted on flexible circuit boards that allow the ASICs to be connected to data and power flexes electrically [91]. Each module (Fig. 3.8-left) consists of the front-end hybrid and the silicon sensor with strips wire bonded to the corresponding input channels. Sensors are read out by two types of modules. The hybrid of B, C, and D sensors host eight SALT ASICs, while hybrids which hosting read-out electronics for sensors A host four of them.

An example of the hybrid module is shown in Fig. 3.7. The green area represents the silicon sensor, whilst the eight yellow rectangles represent the SALT chips. A brown layer represents the underlying flexible circuit transporting power and data (bidirectionally)

to the back-end electronics that connect the ASICs to the individual circuits.

Hybrids have a rectangular shape, approximately $10 \times 3 \text{ cm}^2$. The design of the hybrid is intended to minimise the radiation length. Additionally, the hybrid provides the thermal interfaces between the chips and the cooling system, the electrical connections between the chips, and the electrical connections with the rest of the system. Signals generated in the sensor are processed, digitised, serialised by the ASICs and sent to the DAQ system. The heat generated by the power dissipation of the SALTs must be effectively transferred to the detector cooling system (Fig. 3.7). Thus, effective thermal contact is essential.

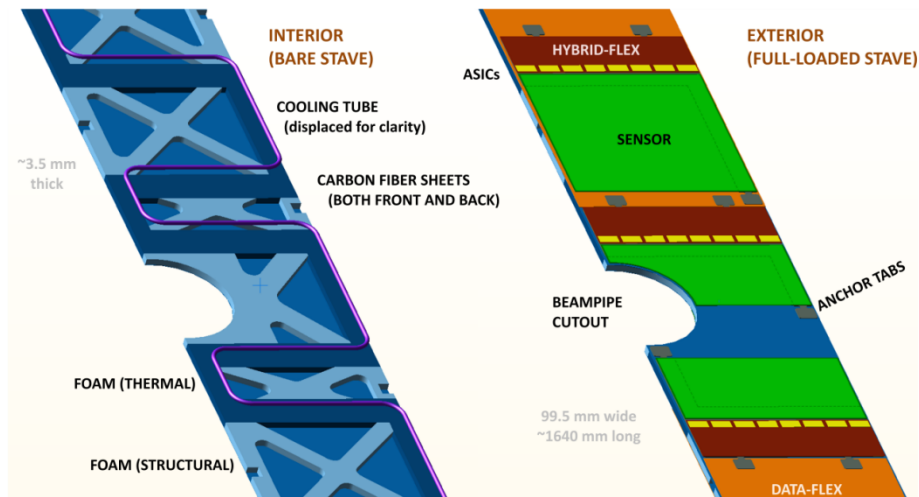


Figure 3.7: UT stave cooling system (left), and UT stave structure with hybrid (right) [91].

3.6 Stave cooling system

Front-end electronics of the UT will be placed near detector sensors in an active area. To reduce radiation damage caused by particle fluence, the cooling system should keep the sensors operating temperature below $-5 \text{ }^\circ\text{C}$ [91]. To prevent the sensor thermal runaway, the cooling system must remove the heat generated in the ASICs, estimated to be 0.77 W per chip. Silicon sensors and power cables are sources of heat. Sensors generate heat depending on their radial position; inner sensors have greater granularity, leading to more read-out chips and consequently greater leakage currents. Four ASICs read out the outer

sensors. The highest heat load is in the inner region (8 ASICs per sensor in the inner region), at a radial distance of about 5 cm. Power cables account for about 10% of the power consumed by ASICs. The cooling system should remove about 5 kW of heat (900 W per plane), considering the heat dissipation in every 4092 ASICs, sensors, cables, and other components. In addition, silicon sensors are required to maintain a temperature range of 5 °C.

Evaporative cooling, which cools CO₂ through an adiabatic process, without using compression or absorption of the coolant, has several advantages over liquid cooling. Having a large latent heat for vaporizing liquid means one need less flow to remove a given amount of energy, which translates into a smaller diameter pipe. The cooling system is designed around CO₂ evaporation at temperatures between -25 °C and below. The temperature of evaporation is fixed, and it is -5 °C for the UT. The temperature of the coolant is around -35 °C at a pressure of 10 bar. A pressure drop should not change more than 1 bar to obtain a stable temperature difference along the pipes line (Fig. 3.8-right) [91].

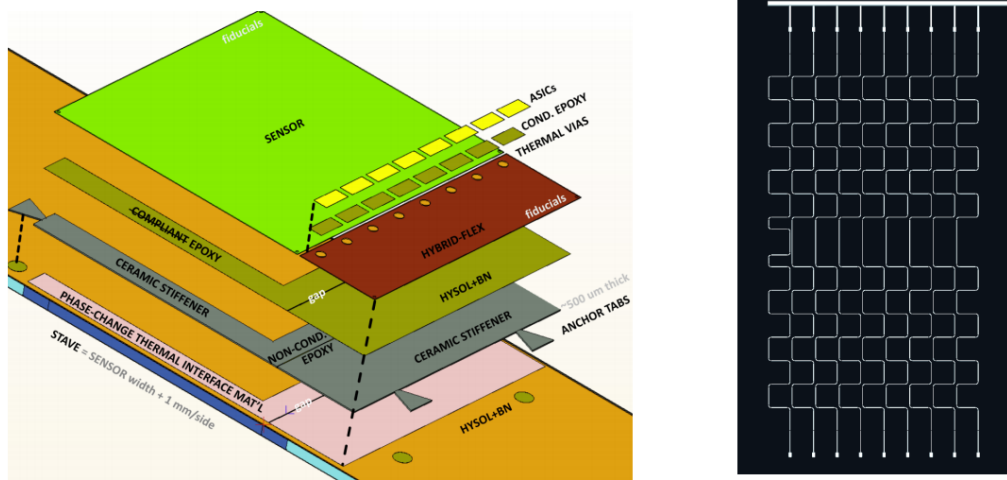


Figure 3.8: Design of the UT module (left), the snake pipe design (right) [93].

Chapter 4

Monitoring and calibration of UT detector

The chapter emphasises the development of UT's calibration and monitoring systems. It comprises the motivation for system development, details of the designed platform, and description of algorithms and interface applications.

4.1 Radiation damage

Silicon sensors used in the reconstruction of particle tracks are the most sensitive components of particle detectors. As follows, silicon-based detectors are often subjected to a harsh radiation environment, especially at hadronic colliders, which decreases their effectiveness over time. Radiation damage can be divided into two classes: bulk damage and surface damage [94], [95].

Bulk damage is mainly caused by the interaction of particles with the silicon crystal structure without ionisation. This, so called, displacement damage occurs when transferred kinetic energy to the lattice is enough to displace a silicon atom from its lattice site. Displaced atoms may create a pair of vacancy-interstitial, or it can rise a cascade of displacements. Minimum recoil energy of 15 eV is required to cause the displacement. Electrons need the energy of 260 keV in order to provide such recoil energy, while protons and neutrons require 190 keV [96], [97]. Most of the primary effects are gone when interstitial and vacancies are annealed; however, there is a large number of defects which are either stable or interact with the crystal impurities to produce permanent effects. The n-type silicon is usually doped with phosphorus. The presence of vacancy right to

the donor dopant changes the crystal's electrical properties because the phosphorus atom cannot fulfil the role of the dopant anymore. This effect, called *donor removal*, leads to changes in the crystal's electrical properties.

The surface region of silicon, as well as the inner area, is sensitive to radiation. The passage of ionising radiation by the oxide layers causes the built-up of latched space charge. Sever effects can arise. It can be electron-hole pairs created in the oxide that does not recombine, moving in the electric field. An electron can escape from the recombination and inject into the silicon bulk, or holes can be trapped at the SiO₂-Si interface. This effect can lead to the degradation of the oxide. Furthermore, the trapped charge produces new energy levels at the SiO₂-Si interface through the bandgap. Leakage current can increase due to the formation of mid-gap generation and recombination centres that facilitate the transition of electrons from the valence to conduction bands. It can change the effective doping concentration of the sensor, which affects the operating voltage needed for total depletion. Finally, the loss of charge collection efficiency due to charge carrier trapping in defect states within the bandgap.

As a result, the continuous impact of particle fluence leads to progressive degradation of their properties and even to their complete failure. Therefore, these changes should be continuously monitored and mitigate where possible.

4.2 Gaudi framework

There are several goals that the experiment software must meet. The software should work universally on many levels and be flexible enough to be adjusted quickly to new requirements that appear throughout the lifetime of the planned experiment. The LHCb collaboration uses GAUDI, a general object-oriented framework designed to provide a common infrastructure and environment for a number of applications from a selection of events on trigger-level through the generation of Monte Carlo data to physics analysis [98], [99]. The core of GAUDI framework is written in C++ programming language. It is based on components that constitute a software system with services and applications. The development of new applications based on common elements (detector description, event model and more) enables a significant increase in the software development efficiency. The design of the input and output operations of the GAUDI includes data flow between different components and high-level options provided by the end-user to manage the whole system. As a result, the user can treat each package as an application controlled

only by a simple script (usually written in Python).

A schematic view of the GAUDI architecture is depicted in Fig. 4.1. It presents the main components, a hierarchy of the structure and data flow.

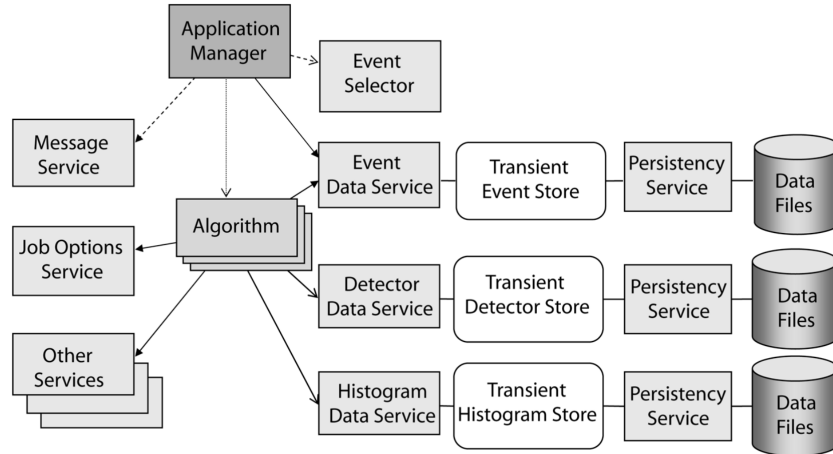


Figure 4.1: A schematic view of the GAUDI architecture [99].

Every GAUDI application includes:

1. **Algorithms:** they are the basic components of the GAUDI application. Each algorithm contains code which proceeds operations by defined input data. Because algorithms are executed sequentially, a series of simple algorithms can be used by complex processing pipelines;
2. **Services:** it is a group of components common to multiple applications. It allows avoiding writing routine code for software tasks typically needed in applications;
3. **Tools:** utilities to help other components perform data processing. Because they are executed on demand, the output of these procedures is local and separated from the general data flow system.

Two main data types are specified within GAUDI. These are *transient data* and *persistent data*. The data flow between algorithms proceeds via the transient store. The basic type of data for the GAUDI application is event data, histograms, projection and tuples. Each type of data is organised under a unique location in separate transient data stores (TDS). The data within the TDS is organised in a tree structure. Data from TDS can be converted into persistent data through a persistence service which uses appropriate converters. Persistent data are saved as a file in data storage.

A common framework for many subsystems requires a universal data structure. In the LHCb experiment, this common data structure is the LHCb Event Model [100], [101]. It describes different aspects of experiments, including Monte Carlo events, digitalised detector data, reconstructed events (vertices, tracks), and detector conditions. Each type of data is stored in a specific location that can be accessed through a unique key. To meet the LHCb framework model requirements, each new data processing platform needs to be adjusted to the well-defined input and output data structure.

4.3 General concept of monitoring and calibration software for UT

The general idea of monitoring and calibration software for UT detector is based on the synergy of several components, where each of them is responsible for a specific task. Depending on the detector operating mode, RAW data stream produced by UT will be sent to Vetra (during the commissioning of the detector - in 2022, there are RAW binary data, while during data taking - from 2023, it will be an LHCb data banks), which is extensively described in the following paragraph. Vetra performs emulation of SALT readout chip, prepares the monitoring plots and produces an output root file for each UT sensor and calibration run. Vetra's output converted to XML file will be send to STORCK - calibration database [102] and from there handled by both inner (UT) and central (LHCb) monitoring (Sec. 4.8). Fig. 4.2 shows the general design of the UT platform for monitoring and calibration of the detector.

Calibration of the detector is described by a configuration file prepared by recipe builder for each SALT and contains information about the current value of noise, pedestal level and more. As one of the tasks of the system is the performance of calibration of the UT detector, dedicated algorithms will analyse calibration data to decide whether there is a need to calibrate the detector. As work on this part of the software is still in progress, the thesis does not contain a detailed description of these algorithms.

4.4 Introduction to Vetra package

Vetra is a successor of the software with the same name that originated in Run 1 and 2, created in 2010 [103] to facilitate the commissioning of the Vertex Locator (VELO), to

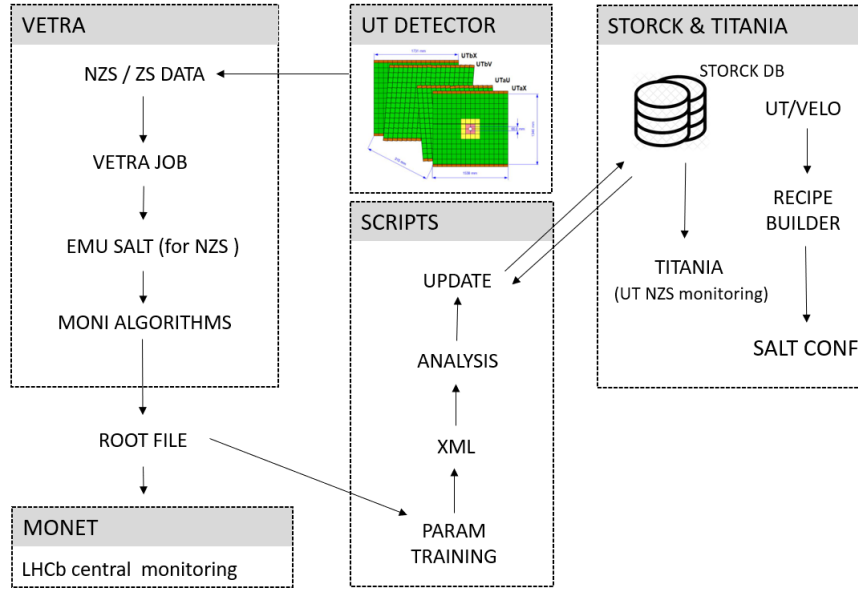


Figure 4.2: General design of UT platform for monitoring and calibration of the detector.

maintain cluster recognition and simulate operations of TELL1 [104] electronics boards. Later, the Vetra framework was also adapted to use the ST detector.

Vetra was a versatile tool for handling various procedures of LHCb silicon detectors, used for data taking, technical breaks and test beam tests. Moreover, it took advantage of computational intelligence methods for signal processing. Furthermore, the entire TELL1 processor logic was implemented to emulate the detector behaviour for both real and Monte Carlo data. Vetra was emulating the Beetle chip, a readout ASIC for the LHCb silicon detectors.

Vetra during Upgrade 1, again, encompasses software for handling the two LHCb silicon detectors, VELO and UT. The platform is built on top of the GAUDI framework within the LHCb software environment and includes the Python/C++ framework for data analysis and persistency.

4.5 Data signal processing

The calibration and monitoring systems at UT are based on an emulation of SALT’s digital signal processing (DSP) that performs various operations on a sequence of digitised signals. For UT, this sequence consists of RAW (unprocessed) ADC values from each channel of the UT detector. The Vetra DSP emulation module can be used for both calculation of the calibration parameters and bit-perfect emulation of the Zero-Suppressed

data produced by the SALT chip. The module consists of the following algorithms:

1. Decoding of the raw data, which consist of binary data into ADCs values in decimal format;
2. Bad or noisy channels rejection (which are excluded from further processing algorithms);
3. Pedestal following/subtraction (calculation of charge value in each channel measured by the readout system in the absence of signal and noise, challenging to implement in the readout system of the sensor);
4. Common Mode suppression (two types of noise are considered, one common to a larger group of channels, while the other is in each channel. In the case of the former, the simplest Mean Common Mode Suppression (MCM) with the assumption that the common mode noise is constant throughout the ASIC is applied; thus, all 128 channels are used to estimate the common noise value for each channel, also challenging to implement in the readout system of the sensor);
5. Zero suppression (events that do not pass the threshold derived from noise are rejected to limit the output of the DSP procedure);
6. Raw bank encoding (output data format).

The Vetra SALT emulation is used for many tasks. First of all, it can evaluate the processing parameters that are uploaded to the chip's memory (this is the core part of the calibration procedure). Next, it can be used to verify the SALT processing by comparing the Zero-Suppressed banks content. Finally, it can be used to perform detailed RAW and calibration data monitoring to analyse the condition of the UT detector.

Decoding

The Front-End data are sent to the Back-End TELL40 through optical fibres following the Gigabit Bidirectional Trigger and datalink (GBT) protocol [105]. The SALT chips send event data to GBTx [106] chips via 320 Mbps link for serialisation and packaging into data frames. In the GBT frame, 112 bits are divided into sub-frames that allow multiple SALTs to share the same bandwidth (Fig. 4.3). The number of links (or e-ports) for event data varies according to the detector region: 5 e-ports and 3 e-ports for the

inner and outer regions. It is caused by the different number of hits in the inner region than in the outer due to the higher fluency of particles during LHC operation. Data must be transmitted with a header which comprises bunch crossing number and another parameter to identify their source. The data length is always a multiple of 12 bits. The following chapter emphasises the most common configuration, but other configurations are extensions of the 3-port configuration.

Time	Bit 111													0	
	E-port	ASIC 0			ASIC 1			ASIC 2			ASIC 3				
	bits	0	1	2	0	1	2	0	1	2	0	1	2		
0	16b	8b	8b	8b	8b	8b	8b	8b	8b	8b	8b	8b	8b		
1	00000	header	data		header	header		header	idle		header	data			
2	00000	data		data		header	data		idle		idle		data	data	
3	00000	header	idle		data		data		idle		idle		header	idle	
4	00000	idle		idle		data		header		idle		header		idle	

Figure 4.3: GBTx frame structure for the UT event data. Example of 4 x 24-bit sub-frame case.

The 12-bit header is divided into 4 fields: 4-bit BXID (bunch crossing ID), parity bit, 1-bit packet flag and 6-bit length. SALT saves a parity bit from detecting bit error and protecting the event's integrity. When the packet flag is 0, the packet is a normal event packet, and the 6-bit field defines the length of the data field. If the flag is 1, the 6-bit field indicates a different type of special packet as listed in Fig. 4.4. The length field defines the length of the data following the header. The possible data types are:

1. Zero Suppression (ZS), compressed data, a length field contains the number of incoming data bits that define the frame's total size;
2. Non-Zero Suppression (NZS), uncompressed data, the data format remains the same except for the length field, which defines that incoming data are NZS;
3. Idle packet, a packet that is sent when there is not enough data;
4. Other: Synch - when the Front-End receives a SYNCH command from TFC, EventBusy packet when an ASIC has too many hits, BX veto (BX VETO) packet, when the TFC system sends a BxVeto command, BufferFull and BufferFullNZS.

Header (12b)				Data	Comment
BXID	Parity	Flag	Length		
4b	1b	1b	6b	12n b	
0000b	1b	1b	11 0000b		Idle
Bxid	*	1b	01 0001b		BxVeto
			01 0010b		HeaderOnly
			01 0011b		BusyEvent
			01 0100b		BufferFull
			01 0101b		BufferFullNZS
			00 1100b	data	NZS
		0b	nhits	data	ZS
12b					Synch

Figure 4.4: Header structure for a different type of data.

The electronics show a fluctuating signal even if no particles pass through the detector. A pedestal is defined as the average level of a signal, whereas noise is its fluctuation. Both values may influence possible readouts during passing particles through the sensor.

Pedestal following and subtraction

The pedestal calculation is described as a running average over a set of training events. For each channel, the pedestal sum is updated by considering the current pedestal sum and the current ADC count. This sum is expressed as follows:

$$P_i^{sum}(n+1) = P_i^{sum}(n) + \frac{\Delta_i(n+1)}{N}, \quad (4.1)$$

$$\Delta_i(n+1) = ADC_i(n+1) - P_i^{sum}(n-1), \quad (4.2)$$

where i indicates a channel and the N is the weighting factor set by default to 1024. Then, the correction for each channel, calculated as $p_i = \frac{P_i^{sum}(n+1)}{N}$ is used to subtract pedestal value. The following algorithm is only executed by the emulation module, then the pedestals are uploaded to the chip's memory to perform subtraction on real data. After the pedestal subtraction the properties of all channels are *equalised*, i.e., on average one should see the mean value of idle channels to oscillate around 0 ADC. This procedure is also called finding the base-line.

Common Mode Suppression, thresholds calculation, Zero Suppression and masking procedure

The next step in DSP is the Common Mode Subtraction and the noise calculation for each channel. There are two significant components of noise that affect the performance of silicon sensors. The first changes each channel independently. Another one is common for a large group. In the UT, it is a group of 128 channels (readout by one SALT chip).

The Common Mode Suppression algorithm consists of two phases. The first was implemented for calculating the average pedestal-subtracted ADC value of a group of channels. Then, this value is used to calculate the new mean value for each channel. The noise is calculated using the following formula:

$$\sigma_i = \sqrt{\frac{\sum_N^{n=1} (ADC_i(n) - \mu_i)^2}{N}}, \quad (4.3)$$

where μ_i is the mean ADC value per channel. Afterwards, the noise value is used to calculate high and low threshold values. These parameters are required in two following procedures. The Zero Suppression procedure rejects all events with the ADC value below the high threshold. It allows for reducing the size of the output of the emulation procedures chain. The low threshold allows estimation of whether the channel should be masked. A channel is masked if met the following conditions:

$$|ADC_i(n) - CMS_i^{corr}| > \beta \sigma_i^{RMS}, \quad (4.4)$$

where σ_i^{RMS} is a channel ADC Root Mean Square, CMS_i^{corr} is a correction, and β distinguish signal events from noise and in UT DSP it is assumed that $\beta = 3$. An example of the DSP procedure is shown in Fig. 4.7 and Fig. 4.8.

In general, the CMS algorithm decreases the noise measured on each channel and makes the base-line more flat.

4.6 Vetra - UT package description

All repositories containing code involved in LHCb data processing are stored in the version control system Gitlab [107]. Vetra is a framework shared by the VELO and UT collaboration. Due to the fact that work on the joint algorithms is not yet complete, the

following list includes only an overview of the Vetra project repository (Fig. 4.5).

Core modules

- *Vetra/UTEmuAlgorithms*

It contains all main data processing algorithms, so-called emulation *engines* that maps one to one with the relative functionality implemented in SALT chip. Each engine performs one operation on a specific part of the data. In Vetra-UT, the engine is created for each type of UT detector sensor or for every 4 ASICs of B, C, or D types of sensors. Parallelisation improves overall performance and prevents interference between data from different sensors. The naming convention includes the names of the main processing operations: *UTEmuRawDataDecoding*, *UTEmuPedestalSubtracion*, *UTEmuCommonModeSuppresion*, *UTEmuZeroSuppresion*, *UTEmuChannelValidation* or the name of the operation for engines;

- *Vetra/UTEmuMonitoring*

It contains all monitoring algorithms. Each monitoring algorithm corresponds to a main data processing algorithm, and the naming convention is similar to these in *Vetra/UTEmuAlgorithms*. The output of data processing algorithms is an input of the corresponding monitoring algorithm (example: *UTEmuPedestalSubtraction* → *UTEmuPedestalSubtractionDataMonitor*). All calibration parameters are stored in histograms. Monitoring algorithms are independent of each other;

- *Vetra/UTEmuOptions*

Python option for Vetra job configuration (I/O, list of algorithms, number of training events, etc.).

Algorithm modules

- *UTEmuAlgorithms/UTEmuRawDataReader*

Include binary data conversion and structuring of data. The decoder (*DataReader*) is implemented in *UTEmuDataReader*. The inner Vetra-UT data structure contains data from one sensor (4 ASICs, 512 channels). Output data are stored in TES (Transient Event Store);

- *UTEmuAlgorithms/UTEmuPedestalSubtractor*

PedestalCalculator (*UTEmuPedestalCalculator*) calculates pedestal level for each

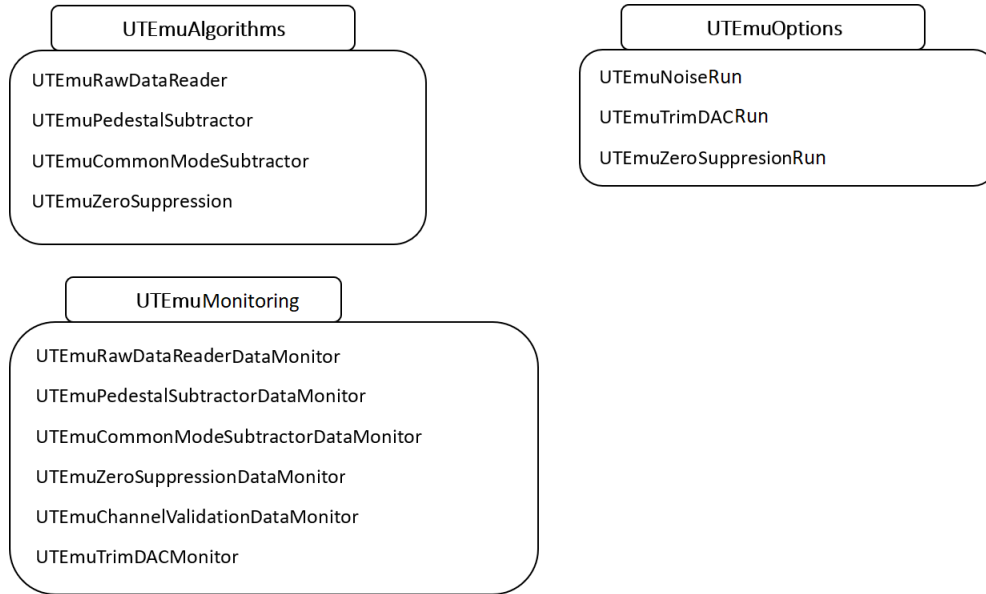


Figure 4.5: List of main components of the Vetra-UT package.

channel using training events, then *PedestalSubtractor* (*UTEmuPedestalSubtractor*) subtracts pedestals from raw data. Pedestal subtracted data are stored in TES. Pedestals can be saved into *.txt* file on demand;

- *UTEmuAlgorithms/UTEmuCommonModeSubtractor*
Calculation and subtraction of common noise for each ASIC and measurement of noise for each channel. Common noise is calculated as a running average with a given number of events and begins after the pedestals calculation phase. CMS data are stored in TES. Noise can be saved into *.txt* file on demand;
- *UTEmuAlgorithms/UTEmuTresholdProvider*
Provide high and low thresholds for each channel defined as a noise in a channel multiplied by a given factor. An input is a noise calculated by *UTEmuNoiseCalculator*;
- *UTEmuAlgorithms/UTEmuZeroSuppressionm*
ZeroSuppressor from *UTEmuAlgorithms/UTEmuZeroSuppressor* repack data to a structure that includes only ADCs from channels for which ADC pass the high threshold value.
- *UTEmuAlgorithms/UTEmuChannelValidation*
Include validation of channels. Channels that for a given number of events do

not record ADC above the low threshold value are considered bad and masked in the further procedure. Channel validator *ChannelValidator* is implemented in *UTEmuChannelValidator*.

Monitoring modules

- *UTEmuMonitoring/UTEmuDataMonitor*
Monitoring of GBTx data packet headers. Calculation of a number of nzs, idle, header only, header event, busy, buffer full, buffer nzs, synch and error (description can be found in [91]) packets in the input file;
- *UTEmuMonitoring/UTEmuRawDataMonitor*
Implements monitoring of decoded ADCs of each channel and projection of ADCs for each ASIC;
- *UTEmuMonitoring/UTEmuPedestalSubtractorDataMonitor*
Monitoring pedestal subtracted ADCs of each channel, projection of ADCs for each ASIC and pedestal values for each channel, each ASIC and sensor;
- *UTEmuMonitoring/UTEmuCommonModeSubtractorDataMonitor*
Monitoring of common noise suppressed ADCs of each channel, projection of ADCs for each ASIC and monitoring of noise values for each channel, each ASIC and sensor;
- *UTEmuMonitoring/UTEmuTresholdProviderDataMonitor*
Monitoring high and low threshold values for each channel;
- *UTEmuMonitoring/UTEmuZeroSuppressionDataMonitor*
Monitoring of zero suppressed ADCs of each channel and projection of ADCs for each ASIC;
- *UTEmuMonitoring/UTEmuChannelValidationDataMonitor*
Monitoring of channel status and calculation of total invalid channels of each ASIC and sensor;
- *UTEmuMonitoring/UTEmuTrimDACMonitor*
Implements standard trimming procedure for finding the trim value for each channel. Using this procedure, similar results can be obtained to these obtained with the

standard procedure comprising pedestal subtraction and common noise suppression and can be applied in case of failure of the standard procedure. TrimDAC scan is performed for each channel using a set of data samples to adjust the average ADC of each channel to zero.

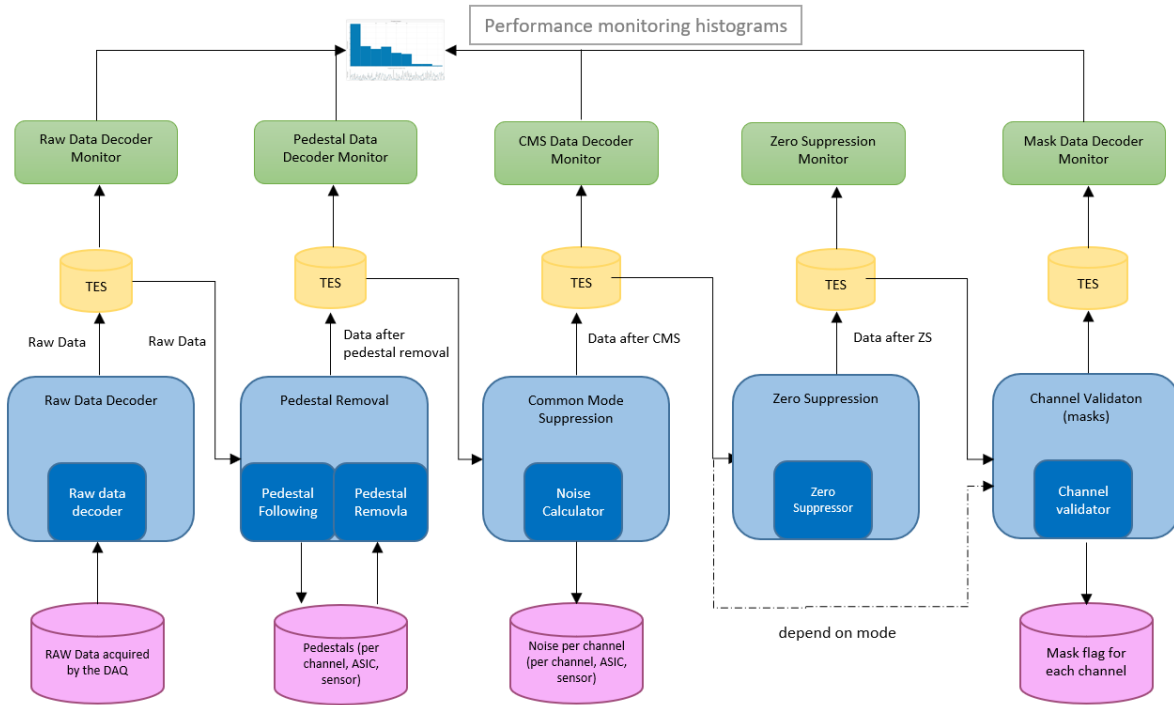


Figure 4.6: Data flow for Vetra-UT noise run.

The scheme of DSP implemented in Vetra-UT can be found in Fig. 4.6.

4.7 UT operation example

The design of Vetra allows for the configuration of the job (DPS of data) a very flexible ways (Tab. 4.1). Each task has a different algorithm sequence, input data type, output data type, and algorithm parameters, such as the number of pedestal training events, noise training events, etc. The following section provides a detailed description of all possible operating modes for Vetra-UT. Fig. 4.7-4.11 present results for test sensor, developed in the early stage of commissioning of UT detector, which allowed for generating data file comprising raw binary data with the same structure as will be obtained from the final detector setup. The investigated dataset contained more than 1000 events, where each event contains an ADC readout for each of the 512 measurement channels of the

UT sensor. 812 events were analysed, as it is the minimum number of events needed to determine the pedestal and measure noise.

Noise run

The noise run comprises calculation and subtraction of pedestals, common noise suppression, calculation of noise and validation of channels. An example of output from monitoring algorithms: decoded ADCs, pedestal subtracted ADCs, and common mode suppressed ADCs is presented in Fig. 4.7, Fig. 4.8 and Fig. 4.9 respectively. There is visible equalisation of the mean of ADC after pedestal subtraction and Common Mode Suppression. Fig. 4.10 shows monitoring plots for pedestal level, noise and threshold for one ASIC from the UT test sensor.

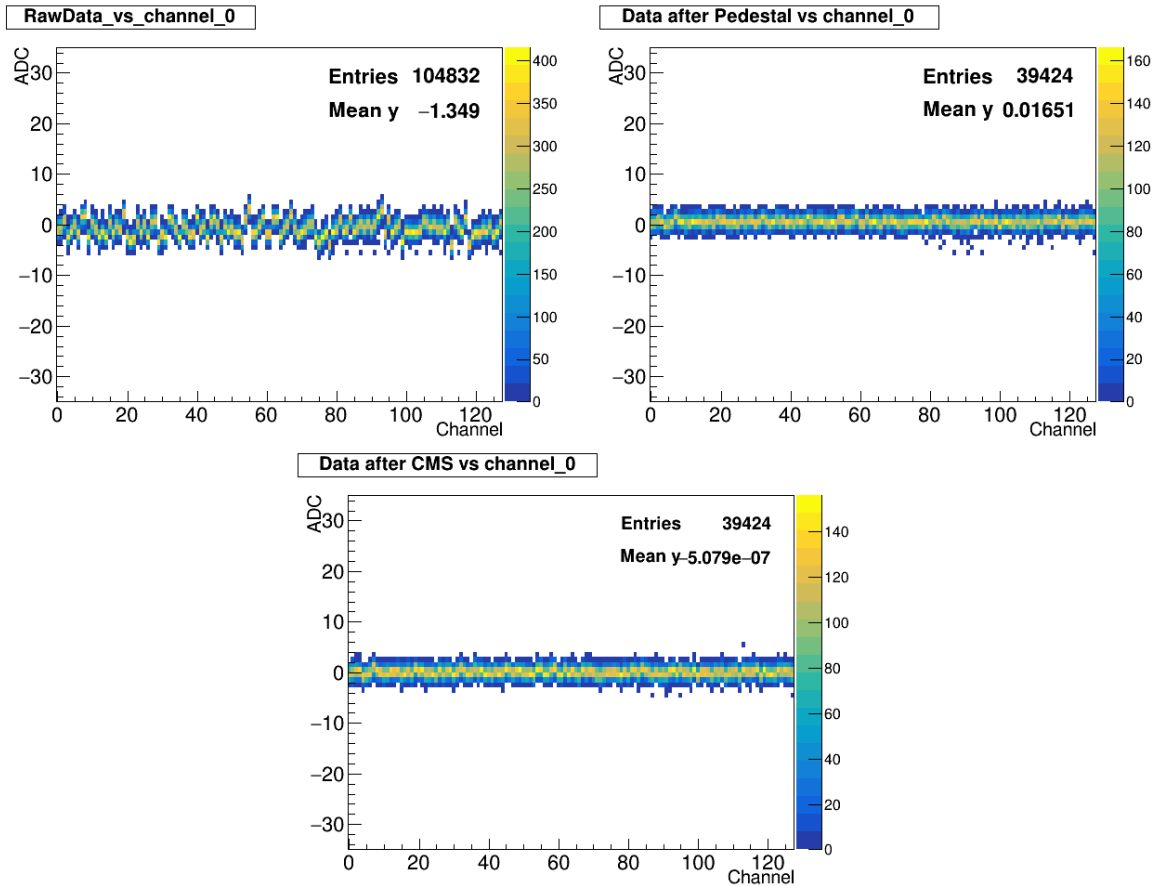


Figure 4.7: ADC vs channel for 812 events collected by one ASIC from UT test sensor for each step of DSP chain: without DSP (top left), ADC after pedestal subtraction (top right), ADC after CMS (bottom).

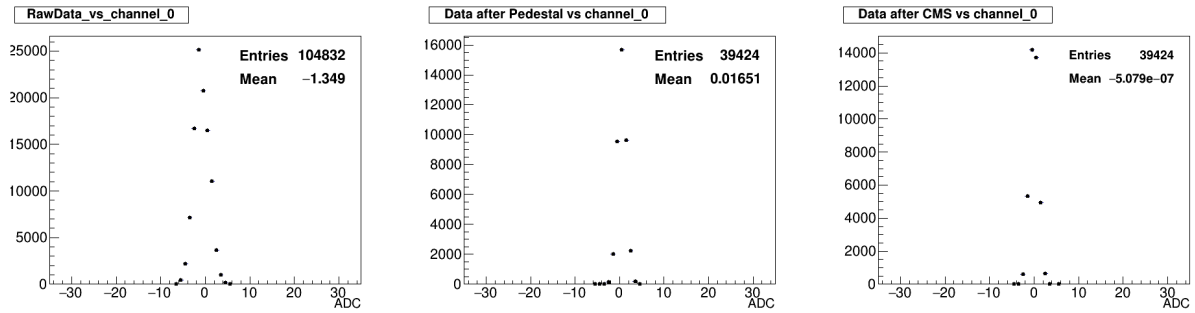


Figure 4.8: ADC distribution for events collected by one ASIC from UT test sensor and all channels for each step of DSP chain: ADC without DSP (left), ADC after pedestal subtracted (middle), ADC after CMS (right).

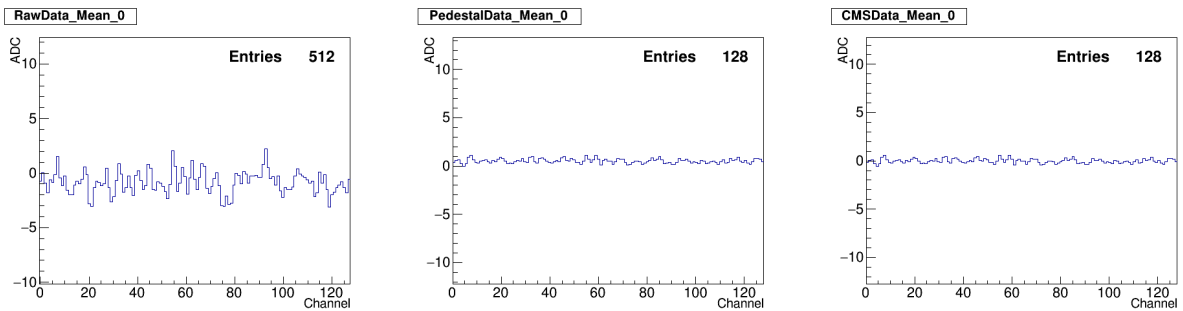


Figure 4.9: Mean ADC for each channel for events collected by one ASIC from UT test sensor for each step of DSP chain: ADC without DSP (left), ADC after pedestal subtraction (middle), ADC after CMS (right).

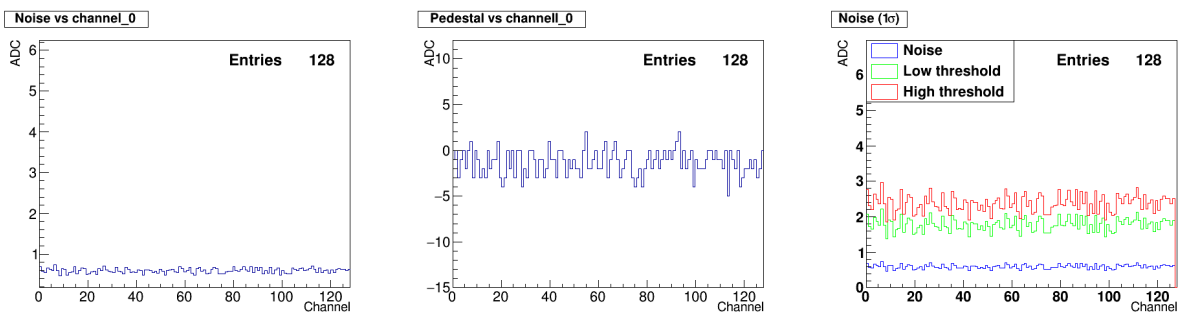


Figure 4.10: Noise (left), pedestal (middle), high and low threshold (right) per channel calculated using training events collected by one ASIC from UT test sensor.

Emulated data are stored in an XML file. A set of XML files is generated after each calibration run. The format includes pedestal per channel, noise per channel, noise per sensor and each SALT chip, mask flags, and mean ADC value for each channel¹ The

¹XML (Extensible Markup Language) is a flexible data format easy to share and display, even without

structure of an XML document is based on tags. Any element has a beginning and an ending tag. Element names describe the element's content, while the structure describes the relationship between the elements. The following hierarchy of files has been chosen: each XML file refers to one of the staves (a set of sensors equipped with a readout system, cooling system and power supply) of the UT plane and contains parameters for all sensors on this staff. Relatively, the small size of these files, allows them to be stored in the Storck data service [102].

TrimDAC run

Another exemplary calibration procedure is an analysis of the TrimDAC scan output. TrimDAC scan is performed for each channel using a set of data samples to adjust the average ADC of each channel to zero. This run allows confirmation that the full processing chain is functionally correct or allows to substitute the standard procedure if it fails. Fig. 4.11 shows the trim DACs work correctly in the whole range, and their trim range is wide enough to correct the baseline spread. A deeper look at Fig. 4.11 reveals small steps in the trim curves. This effect is caused by the higher resolution of the trim DACs over the ADCs.

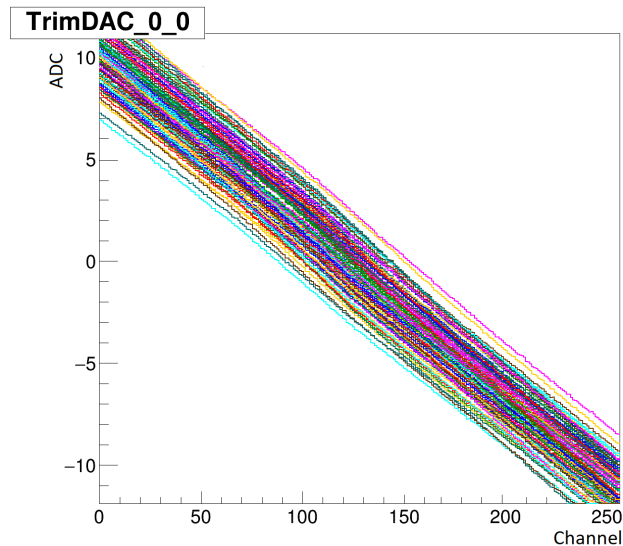


Figure 4.11: Trim Digital-to-Analog Converters (DACs) scan for 128 channels.

an interpreter. It is a self-defining format, meaning the data structure is embedded with the data. XML can also support nested elements or elements within, supporting hierarchical structures.

Zero Suppression run

A Zero Suppression run is similar to a noise run but extends it with a zero suppression algorithm. As the actual data was unavailable at the time of writing this thesis, it was impossible to present the results of the zero suppression algorithm.

Run	Algorithms
Noise	<i>RawDataReader, PedestalSubtractor, CommonModeSubtractor, ChannelValidation</i> + corresponding monitoring algorithms
Zero Suppression	<i>RawDataReader, PedestalSubtractor, CommonModeSubtractor, ChannelValidation, ZeroSuppression</i> + corresponding monitoring algorithms
TrimDAC	<i>RawDataReader, TrimDACDataMonitor</i>

Table 4.1: Algorithms used in each of Vetra-UT modes.

Summary

A list of modes and a detailed description of the algorithms used in each of them can be found in Tab. 4.1.

The plots provided by Vetra can be accessed directly to provide information about software performance. Fig. 4.7-4.11 provide evidence of the platform's proper operation (assuming that the sensor and ASIC are working properly). Fig. 4.7-left shows the correctly decoded ADC for 128 channels, with visible pedestals and noise. Fig. 4.7-middle shows that ADC distribution after pedestal subtraction was equalised, and the baseline is visible, around 0 ADC. Fig. 4.8-right presents that the remaining contribution from common noise was removed, and the baseline equals 0 DAC. The distributions in Fig. 4.9, which shows the mean ADC for each channel and each step of DSP, confirms these results. In the case of TrimDAC studies, Fig. 4.11 shows results of a successful TrimDAC scan for each channel with visible differences between channels and proper readout for each trim value. These views will provide vital input for the daily operation team during proton-proton data taking.

4.8 Interfaces for UT monitoring system

Vetra output stream can be used for the internal and central monitoring interfaces of the LHCb detector. The central monitoring interface for the LHCb spectrometer is Monet [108], whereas the Titania application is an interface for the internal monitoring of the UT detector [102]. Author played a leading role in designing the overall monitoring strategy for UT detector and participated in appropriate high-level software.

Monet

A dedicated interface application is necessary to enable the detector to be monitored by other members of the collaboration, particularly those working in the experiment control room. In LHCb, this interface application is Monet. Each sub-detector's group design and develop a set of views for monitoring purposes. The UT group will contribute to Monet just like others. Additionally, UT experts should be able to monitor the detector without running Vetra to analyse already processed data. The UT's internal interface application is Titania [102].

Monet is a Python-based web application. On the LHCb Online computational farm, a small subset of data selected by the trigger is reconstructed from time to time. Then, the data are grouped into series and shown in Monet.

Monet works in several modes. Prompt DQM (Data Quality Monitor) allows for monitoring already reconstructed data (a unique run number labels each portion) and flagging runs as *good* or *bad* depending on the condition of individual sub-detectors [108]. For the experiment data analysis, only *good* runs can be utilised; hence the online DQM uses the small subset of data to assess the current detector condition by shifter working in the LHCb control room (Fig. 4.12). Several additional modes, such as Simulation DQM, are under development. Monet allows users to browse historical data as well.

Like each detector, UT needs to provide a set of histograms that will allow the detector to be monitored through Monet by the other experiment members who are in the control room during detector operation.

Titania

A project called *Lovell* was used as an interface application during Run 2. Due to its incompatibility with Run 3 requirements, a new application was developed by the VELO group. Because the monitoring and calibration system during Run 3 will be fully shared

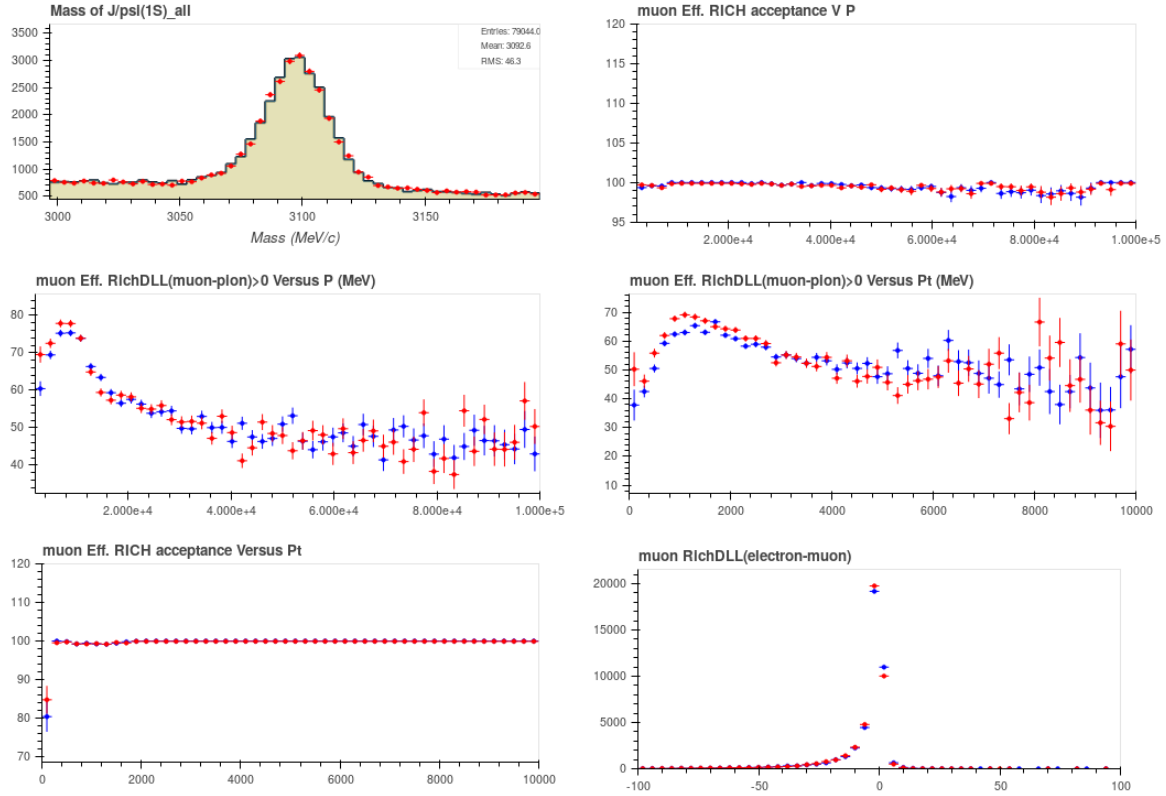


Figure 4.12: An example view of Monet application [109].

between UT and VELO, the framework solution should be reusable and easily applicable for different purposes. As part of its internal monitoring system, UT uses the new application written by members of the VELO group called *Titania*. Several ideas from the Lovell application were transferred, such as the configuration of tabs which gather together histograms describing a particular parameter. It is used as a desktop application by default, but any visualisation can also be adapted to a web browser. The PyQt framework [110] was chosen as an effective way to develop modern GUI applications.

Considering the simplicity of adapting the application, a part of the Author's research work was devoted the development of *Titania* to provide monitoring of the UT detector.

The general philosophy of *Titania* is splitting the monitoring tasks into three aspects: data reading, viewing (linking the entirety of the application with the QtGUI or web interface) and exploration (moving through the data with specialised GUI items). Through this division, data reading and plotting can be independent of the actual viewing mode (web or GUI), allowing re-use without much adaptation (Fig. 4.13).

Several modes were implemented according to the needs expressed by the UT group

and will be progressively developed during the ongoing detector commissioning. During the commissioning of the detector, particular emphasis is placed on measuring basic parameters such as noise and pedestal level to assess the performance of the sensors newly installed on the hybrid. This is especially important because sensors with a high average noise level will not be able to measure particles passing through them. The basic list of modes includes:

1. *Noise/Pedestal view* includes pedestals view (pedestal per channel, average absolute pedestal per ASIC and average absolute pedestal per sensor), noise view (noise per channel, average noise per ASIC and average noise per sensor), masks view (mask flag for each channel, number of masked channel per ASIC and per sensor), thresholds view (low and high threshold value for each channel of one sensor, Fig. 4.14-4.17);
2. *TrimDAC scan view* includes the result of the scan for one ASIC and histogram of trim per channel (also for one ASIC, Fig. 4.18);
3. *Plain view* represents a scan of the sensor's average value of a given parameter (noise, pedestal). This view enables quick localisation of an underperformance sensor without checking all sensors (Fig. 4.19).

An input for Titania depends on the operation mode. The input file for Noise/Pedestal view and plain view is XML [111]. TrimDAC scan views use Vetra's ROOT [112] file as input. The 4.13-4.19 present results obtained from Vetra, which determined the parameters of the UT test sensor.

Summary

Results shown in Fig. 4.13-4.19 prove the proper performance of the Titania-UT application and provide other evidence for the performance of SALT. The average absolute pedestal level in each ASIC remains below 1.5 ADC (since pedestals oscillate around zero and may be negative, their simple average can be around zero even though pedestals themselves can be of high value; therefore, the average absolute value is more suitable in this studies). The noise value remains around 0.5 ADC, the expected value for unirradiated sensors. Because the masking procedure is disabled, the mask view of the Titania application does not provide any valuable information. Thresholds are noise

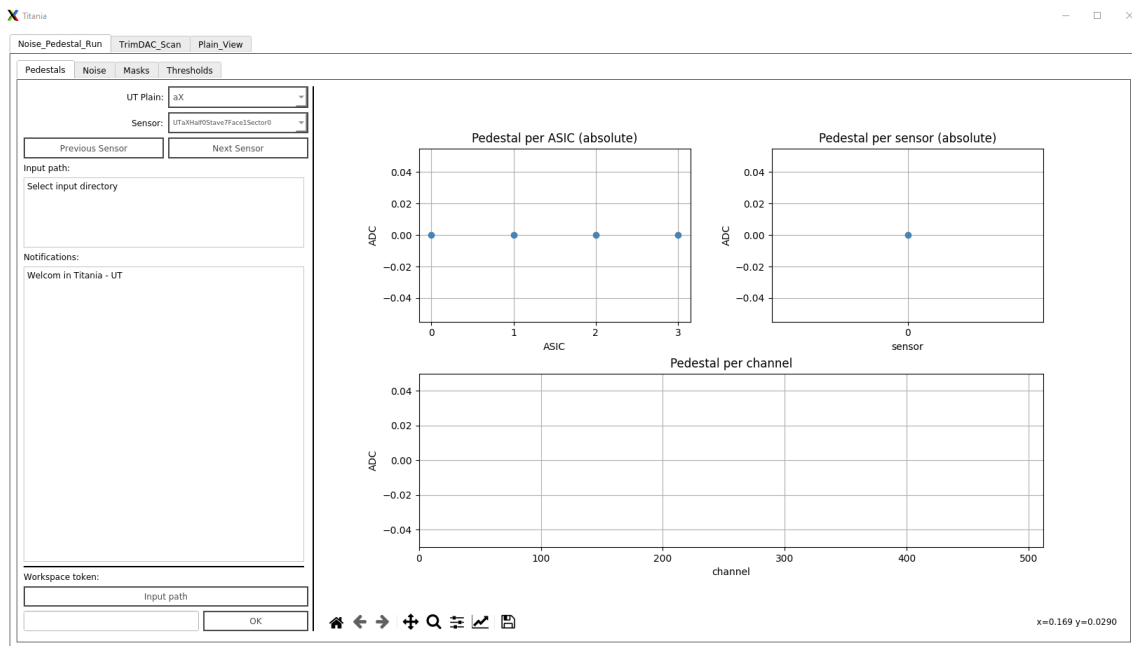


Figure 4.13: Titania - UT application.

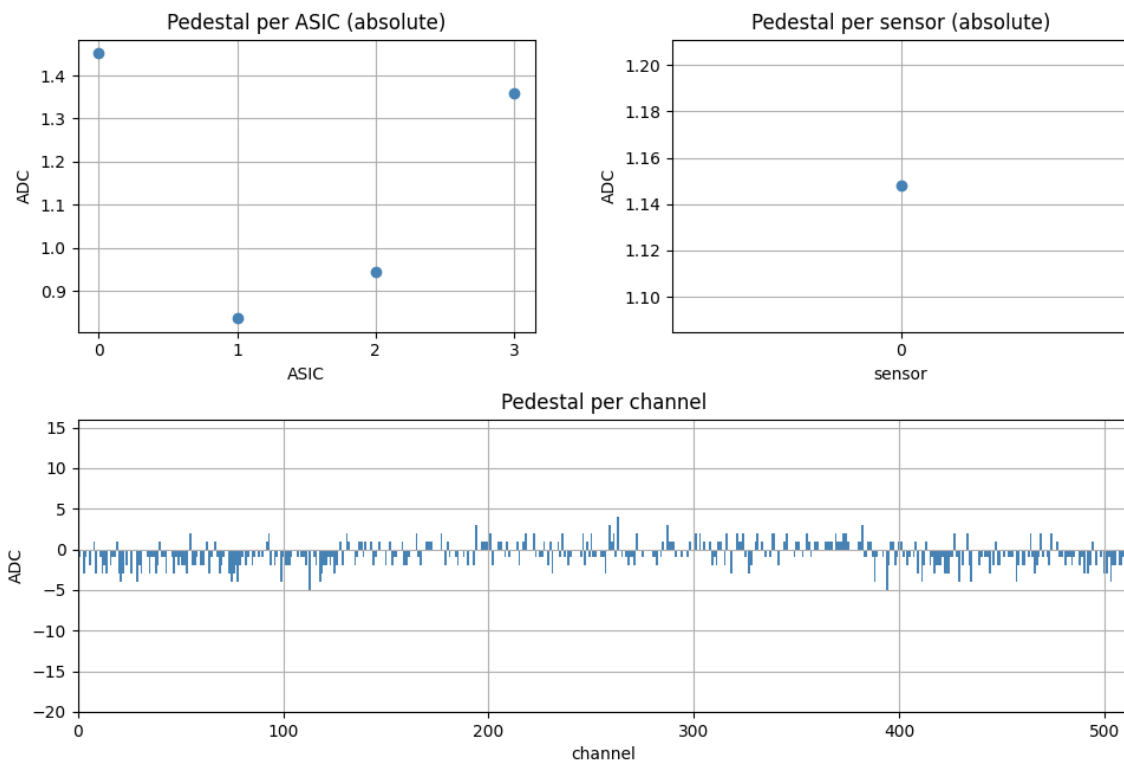


Figure 4.14: Example of pedestal view of Titania application (results obtained using data from UT test sensor).

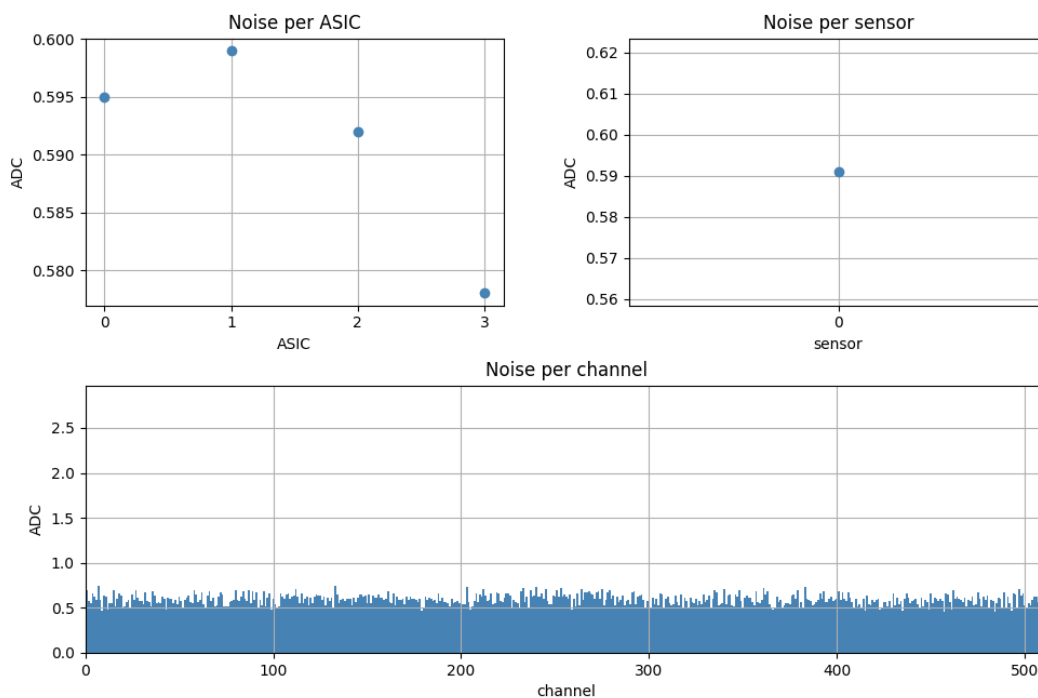


Figure 4.15: Example of noise view of Titania application (results obtained using data from UT test sensor).

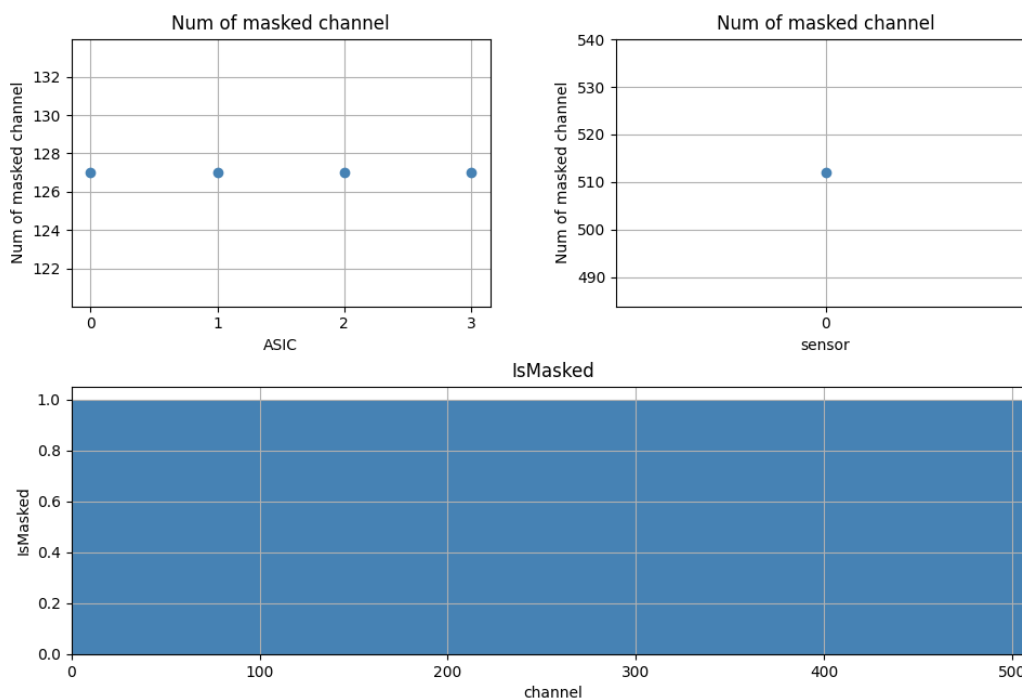


Figure 4.16: Example of mask view of Titania application (results obtained using data from UT test sensor).

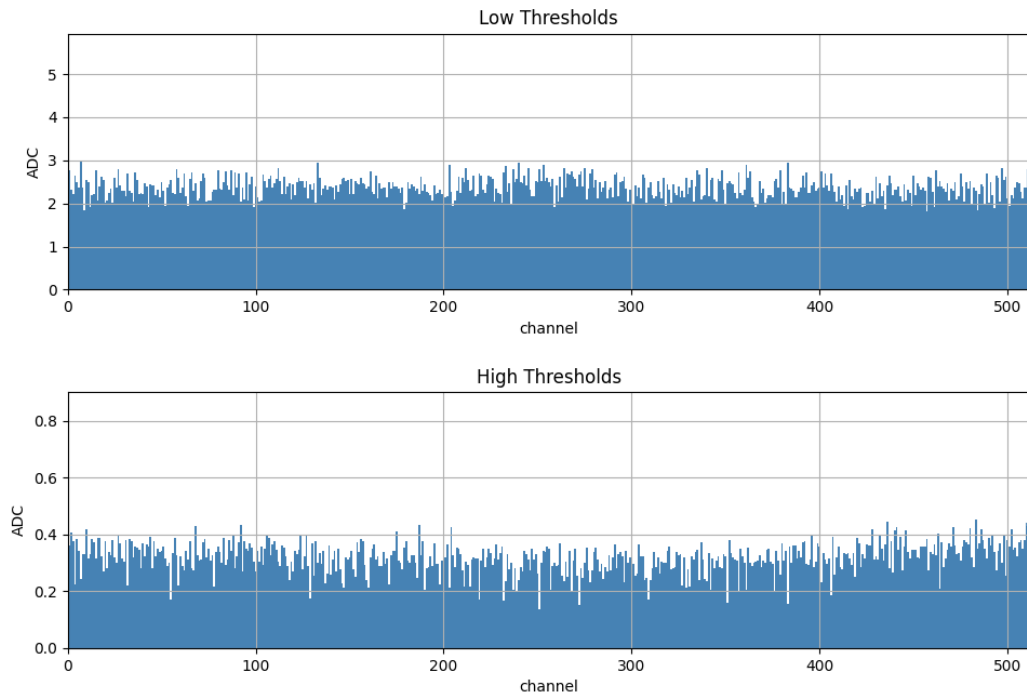


Figure 4.17: Example of threshold view of Titania (results obtained using data from UT test sensor).

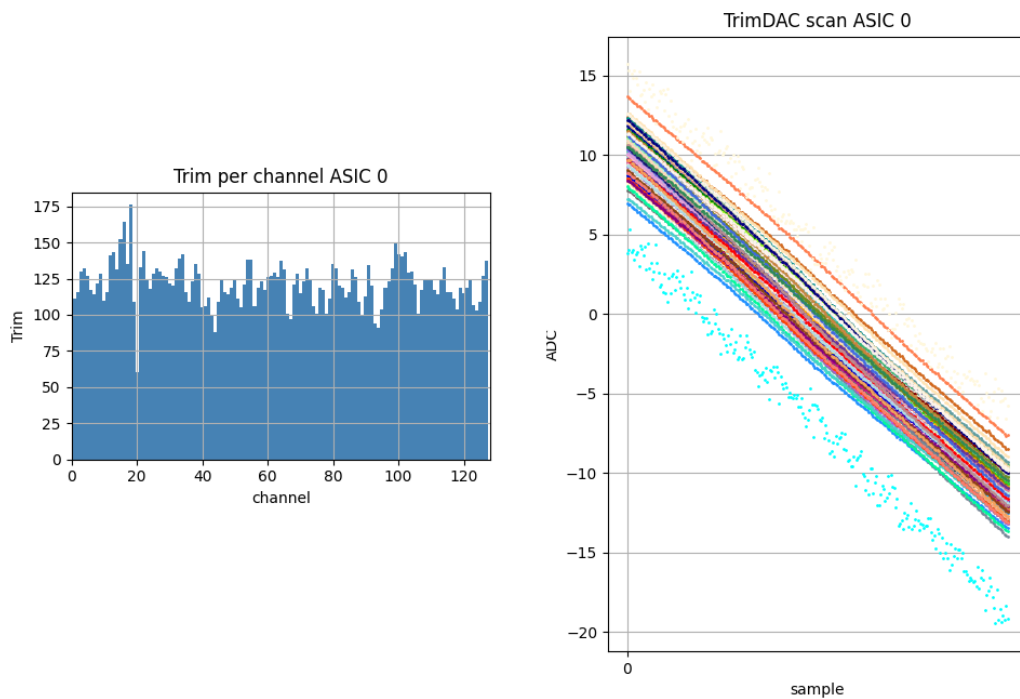


Figure 4.18: Example of TrimDAC view of Titania application (results obtained using data from UT test sensor).

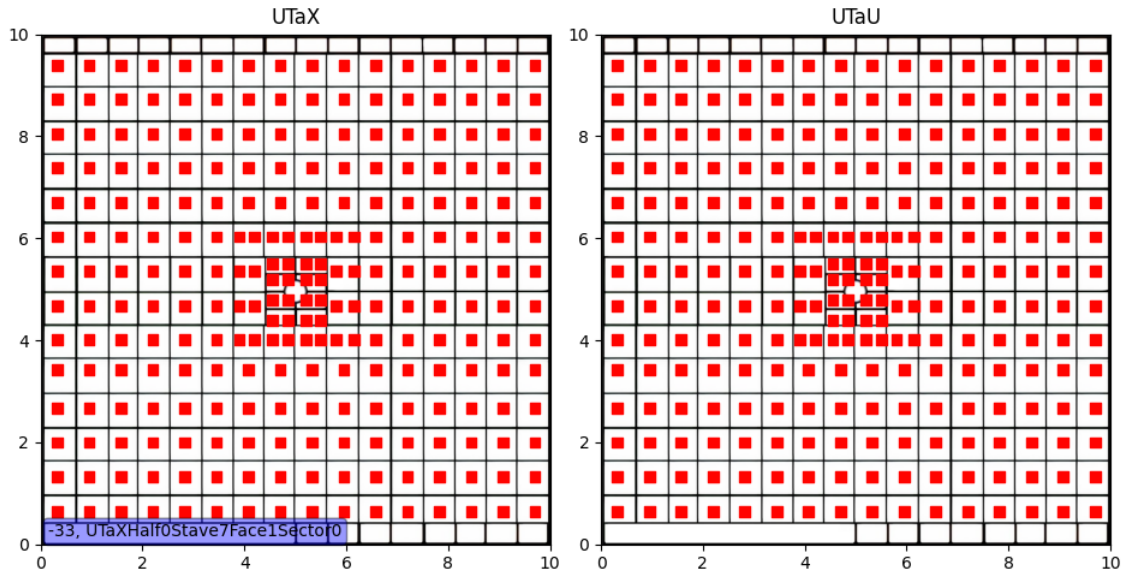


Figure 4.19: Plain view of Titania application (UTaX and UTaU plains).

scaled by noise and high threshold factors. TrimDAC view provides similar results as those obtained directly from Vetra, which means that the application properly reads input data. A view that cannot be obtained directly from Vetra is Plain View. It allows the study of a single averaged parameter for the entire UT detector plain. At this point, it is pedestal and noise, but this functionality can also be extended to the number of masked channels. Although only a single test sensor was analysed so far, this part of the application is ready for visual data from the entire UT detector.

Chapter 5

Analysis of $B_s^0 \rightarrow D_s^{*\mp} K^{*\pm}$ decay

The chapter presents several aspects of the ongoing first measurement of branching fraction of $B_s^0 \rightarrow D_s^{*\mp} K^{*\pm}$ decay. Description of the candidate's selection, including analysis of resonance states $K^{*\pm}$ and $D_s^{*\mp}$, intermediate states D_s^+ and K_S^0 , and results of multivariate analysis are followed by a discussion about possible control channel.

5.1 Preliminary remarks

The following chapter describes details of physics analysis concerning the first observation of $B_s^0 \rightarrow D_s^{*\mp} K^{*\pm}$ decay. This process (hereafter called *signal channel*) proceeds via four charge-conjugate (*cc*) tree diagrams. Each of them includes one or two suppressed amplitudes; therefore eventually, all of them are of a similar order, see Fig. 5.1. In addition, the following decays are selected as a possible candidates for so-called *control channels*:

- $B^0 \rightarrow D_s^{*\mp} K^{*\pm}$,
- $B_s^0 \rightarrow D_s^{*\mp} \pi^\pm$,
- $B^0 \rightarrow D^- D_s^{*+}$.

5.2 Introduction

The measurement of the CKM angle γ of the CKM unitarity triangle is at the top of the flavour physics program of LHCb experiments. Several methods of probing the angle γ were described in Chapter 1.4. Interesting way of determination of angle γ is extraction

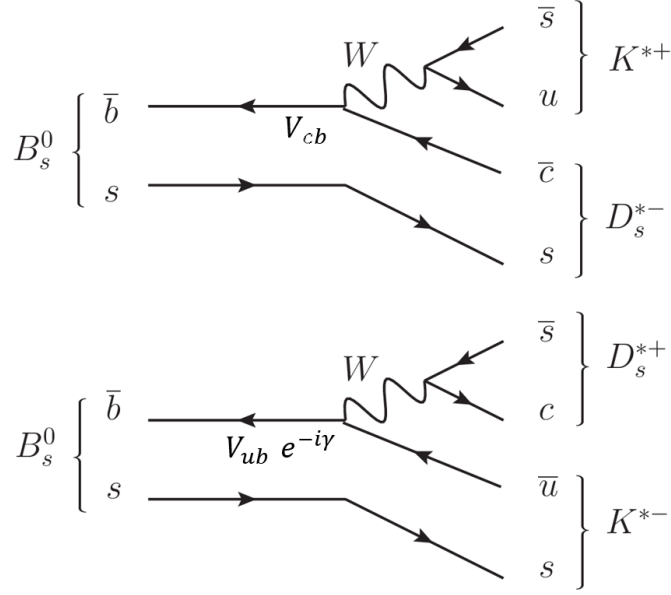


Figure 5.1: Feynman diagram for $B_s^0 \rightarrow D_s^{*\mp} K^{*\pm}$ decay.

of this parameter using time-independent rates of decays such as $B^+ \rightarrow \bar{D}^0 K^+$ [14] or by the time-dependent study of the $B_{(s)} \rightarrow D_{(s)}^{(*)} K$ decays or the analogous $B_{(s)} \rightarrow D_{(s)}^{(*)} \pi$ [113], [114]. Time-dependent CP violation in neutral B -meson decays originates from the interference between two processes: the B^0 - \bar{B}^0 and B_s^0 - \bar{B}_s^0 mixing, i.e. the transformation of B^0 and B_s^0 mesons from their particle to their antiparticle states (and vice versa), and the decay of B meson to two charge-conjugated final states.

Determining the CKM angle γ in tree-level b-hadron decays to open-charm mesons (B2OC) has negligible theoretical uncertainty [16]. The precision of the combination obtained at LHCb experiment allows the angle γ to be determined with an uncertainty of around 4° [14]. This precision is obtained by combining various measurements performed at LHCb as the most accurate measurement has an accuracy of 5° [115].

The precision of the measurement is closely related to the yield of B decay. This is the reason for adding the new B decay channels and updating old measurements with a larger data sample (e.g. over Run 1 and Run 2). The first step of analysis of the new decay mode in terms of the CKM angle γ measurement is branching fraction measurement. Branching fraction (BF or Branching Ratio - BR) is the probability of decay of a given composite particle to a specific decay mode.

5.3 Analysis strategy

The analysis of $B_s^0 \rightarrow D_s^{*\mp} K^{*\pm}$ decay ($D_s^{*\mp} \rightarrow D_s^\mp \gamma$, $D_s^+ \rightarrow hhh$, $K^{*\pm} \rightarrow K_S^0 \pi^\pm$, $K_S^0 \rightarrow \pi^+ \pi^-$, h stands for kaon or pion, Fig. 5.1) is extremely challenging in LHCb environment because it requires the proper selection of soft photons from $D_s^{*\mp} \rightarrow D_s^\mp \gamma$ and reconstruction of resonance state $K^{*\pm}$, which decays to K_S^0 and another pion. K_S^0 meson is a long-lived particle and can decay either inside the VELO or downstream the magnet with no vertex reconstructed using the precise VELO detector. Thus, the K_S^0 mesons are reconstructed at the LHCb using a different track type and the candidate's selection is divided into two exclusive categories: events with K_S^0 reconstructed using downstream or long tracks. The D_s^+ meson is reconstructed in $D_s^+ \rightarrow K^- K^+ \pi^+$, $D_s^+ \rightarrow K^- \pi^+ \pi^+$, $D_s^+ \rightarrow \pi^- \pi^+ \pi^+$ and charge-conjugate modes.

During the writing of this thesis, the analysis is still under development and the final result, including fit to B_s^0 mass distribution of $B_s^0 \rightarrow D_s^{*\mp} K^{*\pm}$ in the signal region, is blinded, which means that the signal region ($B_s^0 \rightarrow D_s^{*\mp} K^{*\pm}$) is not revealed yet, undergoing final scrutiny by the internal LHCb review board. However, the complete analysis has been provided and tuned. There are collision events passing the selection, and all the intermediate particles belonging to the decaying tree are properly reconstructed. These intermediate results prove that the whole analysis and performed selection are valid and work as expected.

The overall analysis strategy is as follows: reconstructed data, which pass trigger and stripping requirements, are selected in terms of choosing candidates for resonance states $D_s^{*\mp} K^{*\pm}$, and intermediate states D_s^+ and K_S^0 . For each selection criterion, the efficiency was determined, showing its impact on the potential reduction of the signal. A further selection is performed by Boosted Decision Tree Classifier (BDT) trained on simulated events and data. After full selection, data are investigated in terms of the analysis of the resonance states (studies of invariant mass distributions of $K_S^0 \pi^+$ and $K^- K^+ \pi^+$, $K^- \pi^+ \pi^+$ and $\pi^- \pi^+ \pi^+$), and the comparison of simulated events and data for selected variables. Finally, a discussion on a potential control channel is presented. The control channel is subjected to an identical selection as signal mode. Based on the number of obtained events, it is possible to calculate the BR for signal mode.

The rough estimation of the branching fraction of $B_s^0 \rightarrow D_s^{*\mp} K^{*\pm}$ decay allowed the evaluation of 400-800 events in every 1 fb^{-1} of data. This estimation was made by comparing the branching fraction of similar processes and taking into account the branch-

ing fraction of all sub-decays ($D_s^{*\mp} \rightarrow D_s^{\mp}\gamma$, $D_s^+ \rightarrow hhh$, $K^{*\pm} \rightarrow K_S^0\pi^{\pm}$, $K_S^0 \rightarrow \pi^+\pi^-$), expected number of $b\bar{b}$ pairs in each 1 fb^{-1} of data and total efficiency of the selection, which was assumed as 1-2%.

Chapter 5.4 details the data sample, trigger and stripping selection used in this analysis and also simulated samples. Chapter 5.6 describes preliminary selection of D_s^+ , K_S^0 , and $D_s^{*\mp}$. Chapter 5.7 includes multivariate analysis using BDT, whereas Chapter 5.8 shows results of further, post-BDT analysis. Finally, Chapter 5.9 discusses possible control channel for the $B_s^0 \rightarrow D_s^{*\mp} K^{*\pm}$ measurement.

5.4 Data samples

This analysis is based on the LHC Run 2 data sample, collected between 2015 and 2018 by the LHCb spectrometer and corresponds to 6.0 fb^{-1} of integrated luminosity [116]. In each year data originated from different stripping lines (stripping selection is detailed in Sec. 2.3.2, Tab. 5.1).

Year	Stripping [81]	Integrated luminosity (fb^{-1})	Energy (TeV)
2015	Stripping24r1	0.328	6.5
2016	Stripping28r1	1.665	6.5
2017	Stripping29r2	1.609	6.5
2018	Stripping34	2.19	6.5

Table 5.1: Summary of the data used in the analysis.

5.5 Simulated events

Full simulation samples were generated for signal mode and both magnet polarities. The 2016 samples were generated using Pythia8 [83] generator¹ and Sim09 Gauss production version²[118]. The sample was generated with all daughters in LHCb acceptance (generated events match the LHCb acceptance) [117]. The signal sample is produced with D_s^+ decay $D_s^+ \rightarrow K^+K^-\pi^+$ (and charge-conjugate decay). In this chapter, the *simulated events* refer to the simulated sample for signal mode.

¹provide the initial proton-proton collisions events

²Gauss is the LHCb simulation program. It consists of a first phase where the events are generated and a second phase where the particles are propagated through the LHCb detectors [117].

Only simulated events which pass the stripping line conditions and additional requirements are considered in this analysis. One of these requirements is the so-called *truth matching*, i.e. events that pass this procedure should have a photon and B_s^0 with trueID of photon and B_s^0 respectively³, reconstructed in the decay chain.

Monte Carlo application in MVA

Simulated events that pass the stripping line conditions and additional requirements are considered as signal decay in the training of multivariate analysis methods. Since a part of the analysis is a classification using Boosted Decision Trees (BDT), samples of the background class into which the event will be classified is also required.

Monte Carlo application in efficiency calculation

Simulated sample is also necessary for the calculation of the efficiency of selection criteria and BDT cut. Efficiency is calculated for each criterion as the number of MC events that pass the requirements to the total number of truth-matched simulated events. Selection efficiency contributes to total efficiency, which is considered during branching fraction calculation.

5.6 Selection

All selection requirements have been chosen, in such a way, to reduce both combinatorial and physics (or peaking) backgrounds retaining at the same time as many as possible signal events. The selection of candidates consists of online and offline parts. The online selection comprises trigger and stripping requirements. The offline selection consists of the following steps:

1. BDT training and choosing the most optimal BDT cut;
2. Selection of D_s^+ candidates and vetos on background contribution related to D_s^+ (D^+ , D^0 , A_c^+);
3. Post-BDT selection including additional particle identification (ProbNN) cut.

³MC-TRUE-ID is variable associated to each simulated event, corresponds to the particle identity [2].

5.6.1 Stripping selection

Data are taken from `B02DsstKsPiLLDsst2DGammaD2HHHBeauty2CharmLine` and `B02DsstKsPiDDDsst2DGammaD2HHHBeauty2CharmLine` lines from the BHADRON stripping stream which produce two sets of candidates: one set of LL candidates (long tracks) and one set of DD candidates (downstream tracks). In the Tab. A.1 (appendix A) details of stripping selection are listed.

5.6.2 Trigger selection

All candidates used in this analysis have passed several trigger requirements. At the level of L0 trigger, the data candidates have to be selected by either `L0HadronTOS` or `L0GlobalTIS` (TOS - Triggered On Signal, TIS - Triggered Independent of Signal⁴ [119]). On the High-Level Trigger (HLT) level, the requirements are typical for analyses of multibody hadronic B decays.

5.6.3 Offline Selection

First, a pre-selection algorithm is used by applying loose kinematical cuts to select intermediate states D_s^+ and K_S^0 and resonance states $D_s^{*\mp}$, $K^{*\pm}$ in $B_s^0 \rightarrow D_s^{*\mp} K^{*\pm}$. Next, a machine learning algorithm is employed to reject background events. The pre-selection criteria are summarised in Tab. 5.2, Tab. 5.6 and Tab. 5.8. The high number of parton interactions during high-energy proton-proton collisions resulted in a large fraction of events having more than one reconstructed primary vertex (PV). These events are called *multiple candidate* events. Since the offline selection removes multiple candidates, there is no need to perform any additional selection of the best candidate in the event at this stage.

Several variables participate in both cut-base and multivariate selections [120]. The description of the most important ones is presented below:

- Particle identification variables (`ProbNN` and `PID`): `ProbNN` are evaluated by a properly trained neural network (multi-layer perceptron) with one hidden layer implemented using the TMVA package. The model was trained separately for each

⁴Triggered On Signal (TOS): events for which the presence of the signal is sufficient to generate a positive trigger decision. Triggered Independent of Signal (TIS): the remaining part of the event is sufficient to generate a positive trigger decision, whereas the rest of the event is defined through an operational procedure consisting in removing the signal and all detector hits belonging to it.

particle in the binary one-vs-rest classification mode, thus creating several separate models. Classification is performed by the network using features from RICH, muon chambers and calorimeters. A separate quantity PID relies on the same information coming from RICH detectors, muon chambers and calorimeters, however, they are combined via computing the log-likelihoods separately for each sub-detector;

- $\Delta\chi^2$: difference of the fit χ^2 with and without considered particle track. To compute it, a track of the particle is combined with the B meson vertex, and the latter is refitted to obtain the new χ^2 value;
- **max (min) DOCA**: maximum (minimum) distance of closest approach between two daughter tracks;
- **DTF CTAU**: distance of flight $c\tau$ of the meson, where τ is the decay time of the meson measured in its reference frame;
- **PT**: transverse momentum of the particle;
- **IP**: impact parameter of a particle with respect to its best parent vertex;
- **ENDVERTEX CHI2**: reconstruction significance of a reconstructed decay vertex of the particle;
- **CL**: The γ CL, the confidence level is the probability that calorimeter hits tagged as a photon is a photon. For true photons, this variable peaks at 1, and for fake photons - at 0;
- **ptasy**: the p_T asymmetry is the feature that estimates the imbalance of p_T around the B_s^0 candidate momentum vector and remaining tracks of the event. It is defined as

$$I_{p_T} = \frac{p_T(B_s^0) - \sum p_T}{p_T(B_s^0) + \sum p_T} \quad (5.1)$$

where the sum is taken over all other charged tracks inconsistent with B_s^0 candidate;

- Δ_R : is a distance in the angular coordinates defined as:

$$\Delta_R(D_s^{*\mp}) = \sqrt{(\eta(D_s^+) - \eta(\gamma))^2 + (\phi(D_s^+) - \phi(\gamma))^2} \quad (5.2)$$

where η is a pseudorapidity with polar angle θ measured with respect to the z axis, and the azimuthal angle ϕ , is the angle measured with respect to the x axis

projection in the xy plane. The Δ_R is invariant under boost along the beams axis. As the typical radius of a hadron jet in the $\eta - \phi$ plane was measured to be about 1, the expected value of Δ_R should be below 1;

- **RFD**: the radial flight distance is defined as the flight distance of particle in xy plain:

$$RFD = \sqrt{(x_{end} - x_{ori})^2 + (y_{end} - y_{ori})^2} \quad (5.3)$$

where x, y are coordinates of a particle and end, ori stands for decay and origin vertex. The RFD variable is used in the selection of D_s^+ and K_S^0 mesons;

- FD_{sig} : stands for fight distance significance defined as the z distance between the particle and B decay vertices divided by the sum of this position's uncertainties in the quadrature:

$$FD_{sig} = \frac{z_{K_S^0} - z_B}{\sqrt{\sigma_{K_S^0}^2 + \sigma_B^2}} \quad (5.4)$$

where $\sigma_{K_S^0}$ and σ_B are the errors of the z position of the K_S^0 and B decay vertex. The same requirement is also made for D_s^+ mesons to separate prompt D_s^+ mesons created in proton-proton collisions from the ones from B mesons decays.

Additionally the `DecayTreeFitter` (DTF) was employed [77]. DTF applies constraints on the reconstructed mass of composite particles by setting their values to the nominal (PDG) masses and refits vertices positions in chain decays. In this study, the D_s^{*+} and K_S^0 candidates were constrained.

Mass distributions for candidates for resonance states $D^{*\mp}$ and $K^{*\pm}$ and intermediate states D_s^+ and K_S^0 after stripping selection are presented in Fig. 5.2.

Selection of K_S^0

The different kinematical properties of long and downstream tracks result in different particle mass resolutions and the number of reconstructed tracks. Because of that, separate selection (Tab. 5.2) was applied for long (LL) tracks and downstream track (DD).

The efficiency of selection criteria calculated using simulated events is presented in Tab. 5.3.

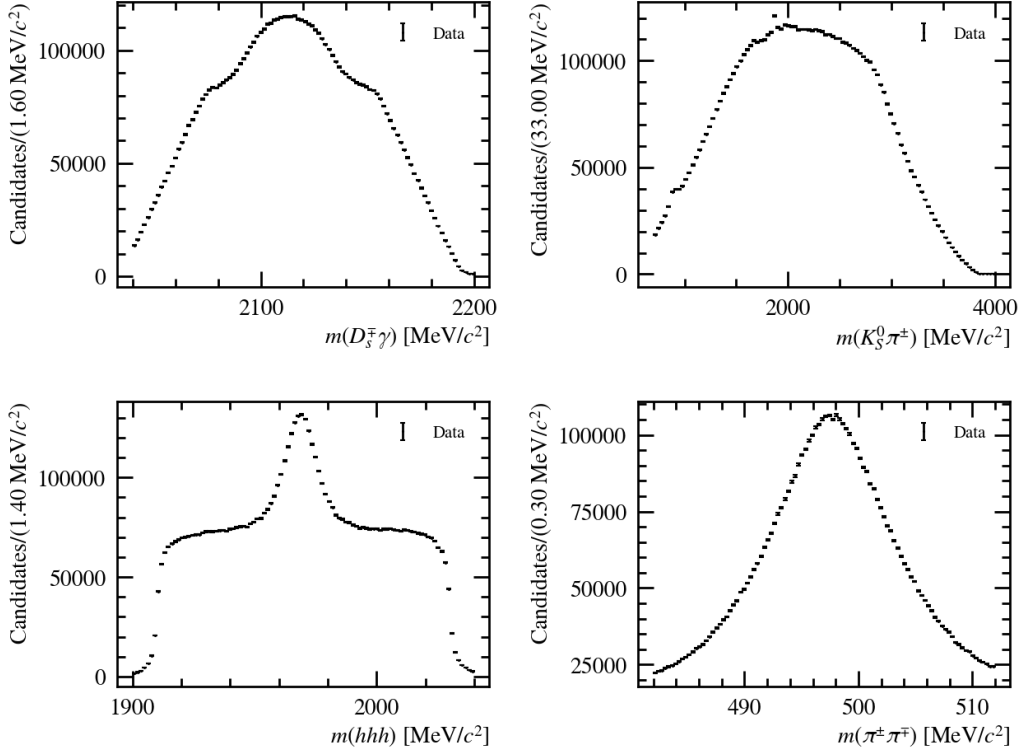


Figure 5.2: Invariant mass distribution of $D_s^{\mp}\gamma$ (top left), $K_S^0\pi^{\pm}$ (top right), hhh (where h stands for kaon or pion, bottom left) and $\pi^{\pm}\pi^{\mp}$ (bottom right).

	Variable	Cut	Justification
DD	$m(\pi\pi)$	$= m_{K_S^0(PDG)} \pm 20 \text{ MeV}/c^2$	Selection of K_S^0
	$K_S^0 FD_{sig}$	> 7	Removing random combinations
LL	$m(\pi\pi)$	$= m_{K_S^0(PDG)} \pm 15 \text{ MeV}/c^2$	Selection of K_S^0

Table 5.2: Offline selection requirements for K_S^0 candidates.

	Variable	Cut	Signal Efficiency (%)
DD	$m(\pi\pi)$	$= m_{K_S^0(PDG)} \pm 20 \text{ MeV}/c^2$	96.6
	$K_S^0 FD_{sig}$	> 7	92.7
LL	$m(\pi\pi)$	$= m_{K_S^0(PDG)} \pm 20 \text{ MeV}/c^2$	96.3

Table 5.3: Efficiency of cuts (K_S^0 candidates).

Selection of D_s^+

The D_s^+ is reconstructed in 3 decay modes: $D_s^+ \rightarrow K^+K^-\pi^+$, $D_s^+ \rightarrow K^+\pi^-\pi^+$ and $D_s^+ \rightarrow \pi^+\pi^-\pi^+$ (cc modes are also considered). The branching fraction for

$D_s^+ \rightarrow K^+ K^- \pi^+$ is around 5 and 10 times greater than for $K^+ \pi^- \pi^+$ and $\pi^+ \pi^- \pi^+$ combinations, respectively (Tab. 5.4, [2]) and all possible combinations are included in this analysis to increase the candidate statistics. Studies of selection criteria were performed without BDT cut at the current stage. 2015 data samples were used to show the procedure of selecting signal candidates and removing the physics background.

Mode	BR
$D_s^+ \rightarrow K^+ K^- \pi^+$	$(5.45 \pm 0.17) \%$
$D_s^+ \rightarrow K^+ \pi^- \pi^+$	$(0.66 \pm 0.04) \%$
$D_s^+ \rightarrow \pi^+ \pi^- \pi^+$	$(1.09 \pm 0.05) \%$

Table 5.4: Branching fraction of D_s^+ meson decay to $3h$ final states [2].

The mass distribution of $D_s^+ \rightarrow hhh$ candidates (h stands for kaon or pion) consists of the physical background originating from D^+ , and Λ_c^+ decays with wrongly identified kaon or pion or D^0 combined with a random kaon or pion. The possible contributions are detailed below:

1. $D^+ \rightarrow K^+ \pi^+ \pi^+$

Misidentification of kaon from $D_s^+ \rightarrow K^+ K^- \pi^+$ or $D_s^+ \rightarrow K^+ \pi^- \pi^+$ with pion from $D^+ \rightarrow K^- \pi^+ \pi^+$ or $D^+ \rightarrow \pi^- \pi^+ \pi^+$. It can be removed (vetoed) if the mass of combination with kaon under π hypothesis is within $m(D^+) \pm 20 \text{ MeV}/c^2$ mass window unless the mass of combination under default K hypothesis is within $m(D_s^+) \pm 20 \text{ MeV}/c^2$ mass window and kaon fulfil the stronger requirement of $\text{PID}(K)$ (Fig. 5.3);

2. $D^0 \rightarrow K^+ \pi^-$ or $D^0 \rightarrow K^+ K^-$

Combination of K and π form $D^0 \rightarrow K^+ K^-$ or $D^0 \rightarrow K^+ \pi^-$ with random K or π . Removed if a combination of $m(K^+ \pi^-)$ or $m(K^+ K^-) > 1850 \text{ MeV}/c^2$ (Fig. 5.4);

3. $\Lambda_c^+ \rightarrow K^+ p \pi^+$

Misidentification of kaon from $D_s^+ \rightarrow K^+ K^- \pi^+$ with a proton from $\Lambda_c^+ \rightarrow K^+ p \pi^+$. Removed if the mass of combination under proton hypothesis is within $m(\Lambda_c^+) \pm 20 \text{ MeV}/c^2$ mass window unless the mass of combination under default K hypothesis is within $m(D_s^+) \pm 20 \text{ MeV}/c^2$ mass window and kaon fulfil the stronger requirement of $\text{PID}(K)$ (Fig. 5.5).

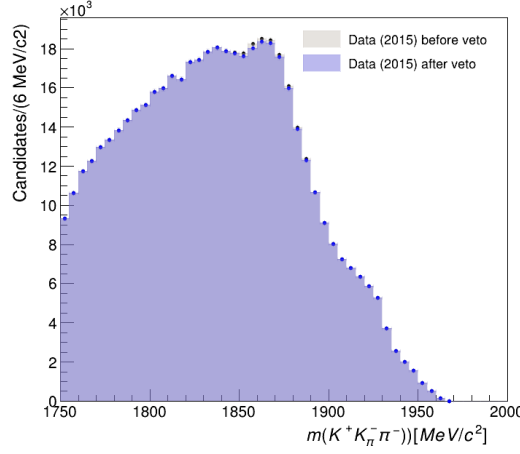


Figure 5.3: Invariant mass distribution of $K^+\pi^+\pi^+$ where the π is misidentified as K . The D_s^+ mass ($D_s^+ \rightarrow K^+K^-\pi^+$) is recalculated under the pion mass hypothesis, black dots and a grey area are the mass distributions before the veto, blue dots and area - after.

Fig. 5.3-5.5 present the result of applying veto on all types of physical background related to decay of D_s^+ meson. The distributions after applying veto (blue dots and area) prove that contributions from Λ_c^+ , D^0 meson were substantially removed. Because one of the stripping requirements limits the contribution from D^+ , there is no visible impact of veto on Fig. 5.3.

The efficiency of the above selection criteria is presented in Tab. 5.5. The uncertainties were limited by a number of simulated events.

Variable	Cut	Signal Efficiency (%)
$m(K^+K^-\pi^+)$	$= m_{D_s^+} \pm 25 \text{ MeV}/c^2$	83.9 ± 4
$\text{hasRich}(K/\pi)$	$= 1$	99.1 ± 4
$\text{isMuon}(K/\pi)$	$= 0$	96.3 ± 4
$D_s^+ FD_{sig}$	> 0	92.7 ± 4

Table 5.5: Efficiency of cuts (D_s^+ candidates).

Selection of $D_s^{*\mp}$

The selection of $D_s^{*\mp} \rightarrow D_s^\mp \gamma$ consists of a cut-based selection of D_s^+ and an additional Δ_M cut. The selection of γ is included in BDT described in Sec. 5.7. The Δ_M variable describes the mass difference between $D_s^{*\mp}$ and D_s^+ mesons, which should be around 144

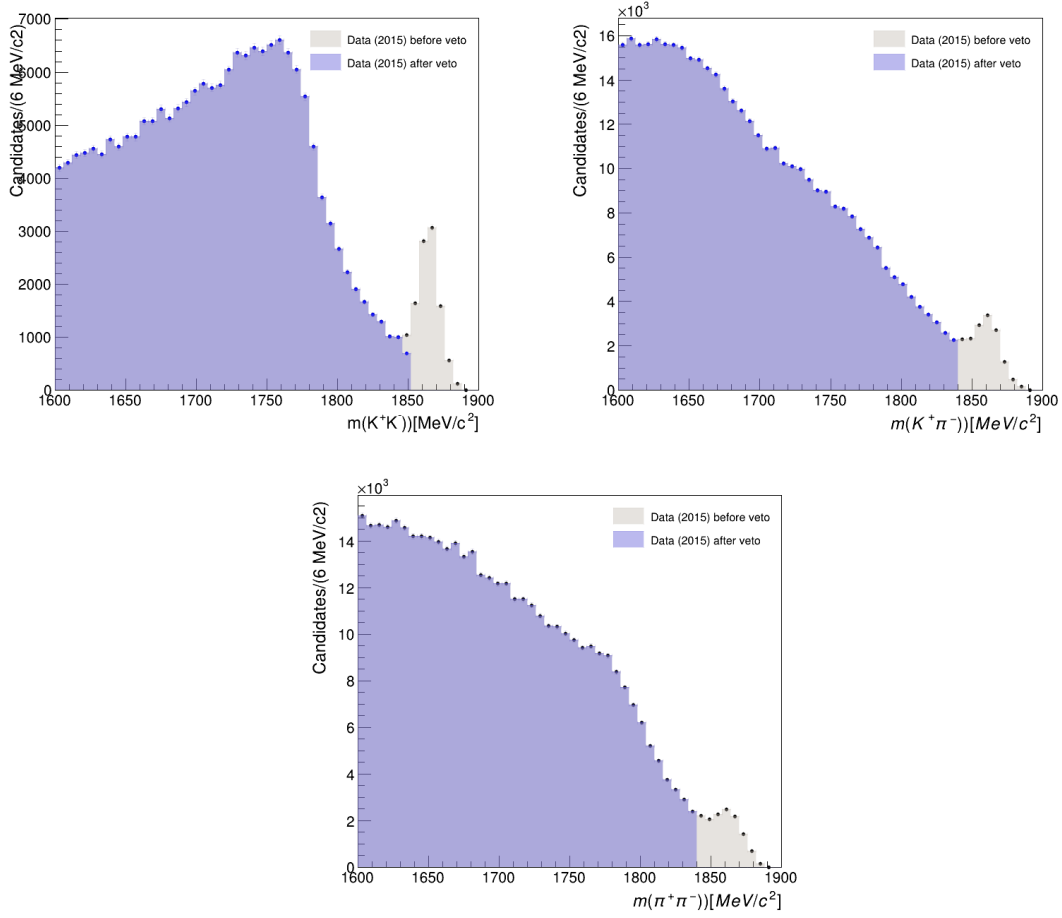


Figure 5.4: Invariant mass distributions of $K\pi$ and KK from $D_s^+ \rightarrow K^+K^-\pi^+$ (left), $D_s^+ \rightarrow K^+\pi^-\pi^+$ (middle) and $D_s^+ \rightarrow \pi^+\pi^-\pi^+$ (right) before (black dots and a grey area) and after the veto (blue dots and area).

MeV/c^2 . This is observed in simulated events, see Fig. 5.6. The significant amount of simulated events fulfils the $\Delta_M \in (124, 164) \text{ MeV}/c^2$ requirement, so these values were applied to the selection (Tab. 5.7).

	Description	Requirement
$D_s^{*\mp}$	Δ_M	$\in (124, 164)$

Table 5.6: Offline selection requirements for $D_s^{*\mp}$ candidates.

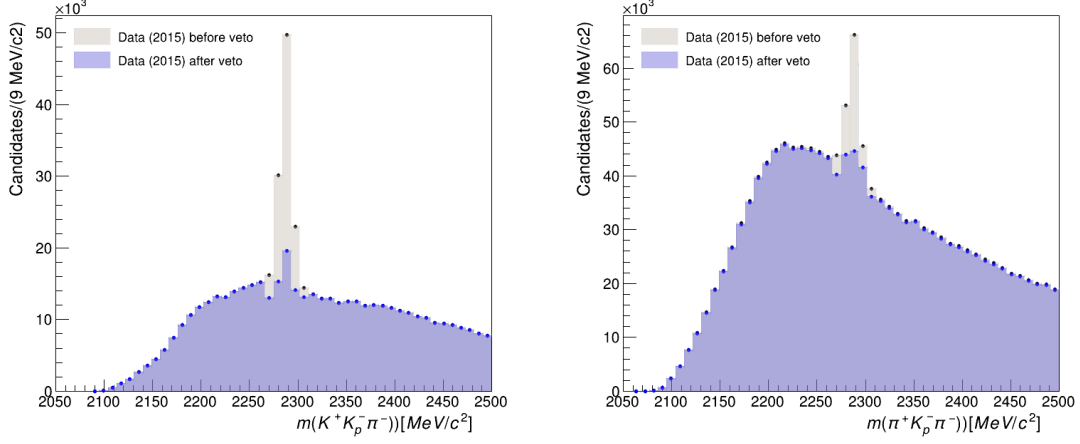


Figure 5.5: Invariant mass distributions of $K^+ p \pi^+$ where the p is misidentified as K . The D_s^+ mass ($D_s^+ \rightarrow K^+ K^- \pi^+$ (left), $D_s^+ \rightarrow K^+ \pi^- \pi^+$ (right)) is recalculated under the proton mass hypothesis; black dots and grey area are the mass distributions before the veto, blue dots and area - after.

Variable	Cut	Signal Efficiency (%)
Δ_M	$\in (124, 164)$	82.6

Table 5.7: Efficiency of cuts ($D_s^{*\mp}$ candidates).

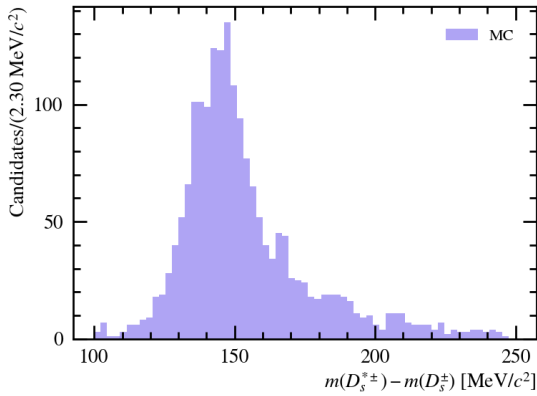


Figure 5.6: Δ_M distribution for simulated events.

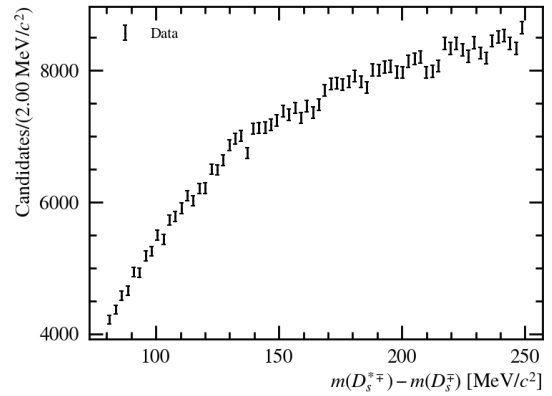


Figure 5.7: Δ_M distribution for sub-sample of 2016 data.

	Description	Requirement
$D_s^+ \rightarrow K^+ K^- \pi^+$	$m(K^+ K^- \pi^+)$	$= m_{D_s^+} \pm 25 \text{ MeV}/c^2$
	PID(K)	> 0
	PID(π)	< 0
	hasRich(K/π)	$= 1$
	isMuon(K/π)	$= 0$
	FD_{sig}	> 0
	D^0 veto	$m(K^+ K^-)$
$m(K^+ \pi^-)$		$< 1850 \text{ MeV}/c^2$
Λ_c^+ veto	$m(K^+ K^- \pi^+)$	$\neq m(\Lambda_c^+) \pm 40 \text{ MeV}/c^2 \parallel \text{PID}(K)\text{-PIDp}(K) > 5$
D^+ veto	$m(K^+ K^- \pi^+)$	$\neq m(D^+) \pm 20 \text{ MeV}/c^2 \parallel \text{PID}(K) > 7$
$D_s^+ \rightarrow K^+ \pi^- \pi^+$	$m(K^+ \pi^- \pi^+)$	$= m_{D_s^+} \pm 25 \text{ MeV}/c^2$
	PID(K)	> 0
	PID(π)	< 0
	hasRich(K/π)	$= 1$
	isMuon(K/π)	$= 0$
	FD_{sig}	> 0
	D^0 veto	$m(K^+ \pi^-)$
$D_s^+ \rightarrow \pi^+ \pi^- \pi^+$	$m(\pi^+ \pi^- \pi^+)$	$= m_{D_s^+} \pm 25 \text{ MeV}/c^2$
	PID(π)	< 0
	hasRich(K/π)	$= 1$
	isMuon(K/π)	$= 0$
	FD_{sig}	> 0

Table 5.8: Offline selection requirements for D_s^+ candidates.

$K_S^0 \pi$ spectrum studies

Since the sum of the K_S^0 and π^+ masses is relatively small and at LHC they can be produced with large energy; therefore it is expected the $K_S^0 \pi^+$ mass spectrum should be populated with resonance states. Fig. 5.2-top right shows the $K_S^0 \pi^+$ spectrum in 700 - 2500 MeV/c^2 range. There are small peaks, later recognised as candidates for $K^{*+} \rightarrow K_S^0 \pi^+$ and $D^+ \rightarrow K_S^0 \pi^+$ around 892 MeV/c^2 and 1896 MeV/c^2 , respectively. The latter state is further investigated for the purpose of $B^0 \rightarrow D^- D_s^{*+}$ studies, detailed in Sec. 5.9.

Fig. 5.8 presents the invariant mass of $K_S^0 \pi^+$ candidates for simulated events. No special requirements were applied in the stripping lines to choose $K^{*\pm}$ and D^- in the $K_S^0 \pi^+$ spectrum, so the further selection of these processes is based on the cut on the invariant mass on $K_S^0 \pi^+$, detailed in Sec. 5.8. The only one selection criteria regarding of $K_S^0 \pi$ final state was PID cut on the accompanying pion (Tab. 5.9, Tab. 5.10).

	Description	Requirement
$K^{*\pm}$	PID(π)	< 0

Table 5.9: Offline selection requirements for $K^{*\pm}$ candidates.

Variable	Cut	Signal Efficiency (%)
PID(π)	< 0	86.6

Table 5.10: Efficiency of cuts ($K^{*\pm}$ candidates).

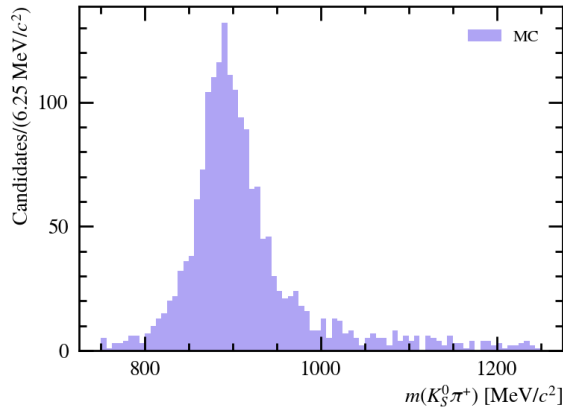


Figure 5.8: Invariant mass of $K_S^0 \pi^+$ candidates for simulated events.

5.7 Multivariate analysis

Accurate studies of particles produced in accelerators require simultaneous analysis of several kinematic and topological variables. Binary classifiers, which belong to multivariate analysis methods (MVA), are suitable to cope with this challenge. Due to their effectiveness, they have become an integral part of modern physics analyses.

5.7.1 Introduction to MVA methods

Multivariate analysis is based on the principle of multivariate statistics, which involves observing and analysing random variables, spanning the space R^N . The fundamental difference between MVA and other statistical methods is providing a bijective map, $M(\vec{x}) : \vec{x} \in R^N \rightarrow R$, between the event features and real, one-dimensional function. The function $M(x)$ is evaluated using intelligent models trained on specially prepared data sets. In a sense, one can understand this procedure as moving from applying many cuts in a linear, sequential way to a single cut on a one-dimensional variable combining all the information, about a given event, in a non-linear manner. The latter usually results in a significantly better signal-to-background ratio. There are several applications of MVA methods; however, most regard classification and regression.

Intelligent algorithms exploited by the MVA approach attempt to approximate an unknown multidimensional parent probability function describing the physics events using a small set of *training* events with a known class (or label) during the procedure called the training. A properly trained intelligent model can then evaluate the $M(\vec{x})$ map, called the model response, which is interpreted as the probability of a given event belonging to one of the classes (signal or background). Usually, an additional constrain, called external heuristic⁵ is used to work out the best working point of the model. In this way, one can use just a single cut applied to the model response function to assign the class of the event.

One of the main problems related to the training of the MVA algorithm is overfitting. Overfitting in data science occurs when an intelligent model fits its training data very accurately, reproducing local data statistical fluctuations as data set features. This results, in turn, in the algorithm being unable to classify properly different unseen data, defeating its purpose. Generalising a model to new data allows using machine learning algorithms

⁵For instance, one can use the signal over background ratio to tune the model response. This variable is not used during the training; thus, the name external.

to classify data.

The model response function, $M(\vec{x})$, is often called a *classifier*. Thus, the following step is called the classification (or evaluation) of *test* events from the test sample (not used in the training procedure). This set is similar to training one; however, they are not the same events. Comparison of response obtained by the classifier with its true label allows estimating the classifier's efficiency and accuracy. One method for determining classifier performance, the *confusion matrix*, is described in this chapter.

The main methods of multivariate analysis include:

- Linear methods: involving the linear division of a set of variables into classes. A hyperplane in a multidimensional space is determined such that instances belonging to different categories are separated from each other on the projected plane. Popular linear methods include Fisher's linear classifier;
- Non-linear methods: include the naive Bayesian classifier and neural networks. A naive Bayesian classifier is built from probability distribution estimators for each variable and each class of events. A Neural Network (NN, [121]) is a method involving the construction of a function composed of a set of simpler functions, which usually is a component of another even *bigger* function. Such a construction resembles the network of neurons found in the brain. Another popular classifier is decision trees.

5.7.2 Boosted Decision Tree

Decision Trees are supervised learning⁶ technique that predicts values of responses by learning decision rules derived from features. They can be used in regression and classification problems; therefore, they are sometimes also referred to as Classification and Regression Trees. Decision trees divide the multivariate space of features (describing the properties of classified events, Fig. 5.9 - x_1, x_2) into several orthogonal areas (Fig. 5.9-right). The classifier assigns a value to each area (called *leaf*, Fig. 5.9 - K_1-K_5). In the sequential decision-making method, the available space is divided into two parts with each successive step (this division point is called *node*). A binary tree can represent this process graphically (Fig. 5.9-left).

⁶Supervised learning is a subcategory of machine learning. It is defined by its use of labeled datasets to train algorithms that classify data or predict outcomes.

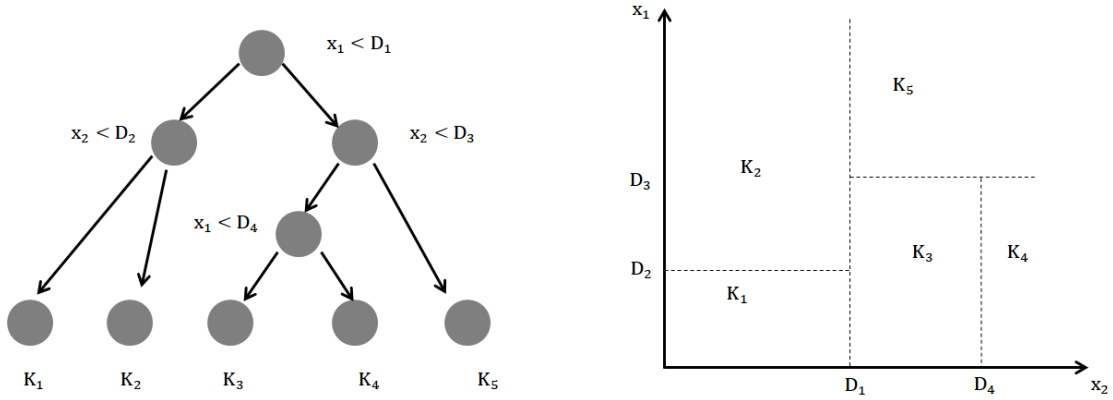


Figure 5.9: Example of classification decision tree (left) and the space division it generates (right). A black circle represents each node, and K1-K5 represent the leaf (classes).

There are several methods of optimisation of tree training. To avoid overtraining, it is necessary to stop adding new nodes at the right moment. A loss function (different for classification and regression problems) assesses whether a tree is already sufficiently expanded; however, other criteria like the number of instances assigned to a single leaf can also be used. Another method of optimisation is *tree pruning* which simplifies the tree with the least possible loss of mapping quality. This procedure mainly saves time and computational resources. The pruning algorithms include *Expected Error Pruning*, which recursively removes a node for which the error function of the preceding node is less than the sum of the errors of the node below, and *Cost Complexity Pruning* in which one compares the improvement in classification of the entire node against the classification efficiency of a single node at the exact location [122].

The effectiveness of classification by decision trees can be increased by combining a series of classifiers (even very weak ones) into one strong classifier. There are several techniques of combining classifiers, such as bagging or the random forest method. Boosting involves sequentially training individual models. Based on the results of the previous training, the loss function for the next model is determined [122].

5.7.3 Multivariate analysis in $B_s^0 \rightarrow D_s^{*\mp} K^{*\pm}$ studies

Because the downstream and long tracks have different properties, separate algorithms were trained for both types of tracks (DD and LL classifiers). During preliminary studies, several algorithms, including Neural Network and Boosted Decision Tree, were investigated

to choose the most effective one. Finally, the BDT algorithm with the gradient boosting (BDTG) from the XGBoost library [123] was chosen as the final model.

5.7.4 Configuration of the algorithm and studies of matrices

To reduce overfitting, the following hyperparameters of the classifier were adjusted (hyperparameters are parameters whose values control the learning process):

- Learning rate - η , after each boosting step (adding a new tree), shrinks the feature weights to make the boosting process more conservative;
- Maximum depth of a tree - higher maximum depth makes the model more complex and more likely to overfit;
- Minimum child weight - a minimum sum of instance weight needed in a leaf node. If the leaf node with the sum of instance weight is less than the minimum child weight, then the building process will give up further partitioning;
- A minimum loss reduction - γ required to make a further partition on a leaf node of the tree. The larger γ is, the more conservative the algorithm will be;
- Subsample - a ratio of the training sample - as a default is set to 0.5, which means that the algorithm would randomly sample half of the training data before growing trees. Subsampling occurs once in every boosting iteration;
- Number of estimators - a maximum number of trees in the classifier. The actual number of estimators depend on *early stopping*, which stops the training process if the loss does not decrease over a certain number of boosting iteration.

For BDT training, a simulated sample was employed with generator level cuts and true matching applied. The background sample was chosen using data events from the high mass side-band region of the B_s^0 mass (above 5600 MeV/ c^2) spectrum. Configuration used to increase the algorithm's efficiency was chosen using grid-search technique⁷ and is presented in Tab. 5.11.

All other parameters are used with their default value (default for XGBoost). The BDTs are trained using a total of 14 variables. Variables are listed in Tab. 5.12.

⁷Grid search is a tuning technique of exhaustive search of a combination of hyperparameters which results in the most efficient algorithm, e.g., the smallest classification error.

Hyperparameter	Value
learning rate	0.2
minimum child weight	5
gamma	0.5
subsample	0.5
max depth	4
n estimators	500

Table 5.11: Hyperparameter values selected for DD and LL classifier.

Particle	Variable	
D_s^+ and γ	D_s^+ flight distance significance	$D_s^+ FD_{sig}$
	χ^2 /ndf of the lifetime	$D_s^+ \tau \chi^2$ /ndf
	γ confidence level	γCL
	γ transverse momentum	γPT
$D_s^{*\mp}$ D_s^+ daughter	Δ_R distance	$\Delta_R(D_s^{*\mp})$
	minimum transverse momentum	$h_1 - h_3 \min(p_T)$
	minimum impact parameter χ^2	$h_1 - h_3 \min(IP\chi^2)$
K_S^0	maximum track ghost probability	$h_1 - h_3 \max(trk_{ghost})$
	transverse momentum (DD)	$K_S^0 PT$
B_s^0 meson	flight distance significance (LL)	$K_S^0 FD_{sig}$
	radial flight distance	RFD(Bs)
	impact parameter χ^2 w.r.t PV	$B_s^0 IP\chi^2$
$K^{*\pm}$	p_T asymmetry	I_{p_T}
	Δ_R distance	$\Delta_R(K^{*\pm})$
π^+	impact parameter χ^2 w.r.t PV	$\pi^+ IP\chi^2$

Table 5.12: Variables used for the BDT training of DD and LL classifiers.

The variable importance was estimated on the test sample extracted from the training sample during classifier training (Tab. 5.13).

No significant differences were observed between the BDT distributions for the training and test samples. Thus, one can presume that overtraining of the algorithm did not occur (Fig. 5.10).

Variable	Importance DD	Importance LL
$D_s^+ FD_{sig}$	0.032	0.044
$D_s^+ \tau \chi^2/ndf$	0.027	0.023
γCL	0.004	0.000
γp_T	0.019	0.034
$\Delta_R(D_s^{*\mp})$	0.034	0.059
$h_1 - h_3 \min(p_T)$	0.035	0.054
$h_1 - h_3 \min(IP\chi^2)$	0.126	0.123
$h_1 - h_3 \max(trk_{ghost})$	0.035	0.038
$K_S^0 p_T (K_S^0 FD_{sig})$	0.010	0.267
RFD(B_s^0)	0.021	0.054
$B_s^0 IP\chi^2$	0.060	0.188
I_{p_T}	0.068	0.037
$\Delta_R(K^{*\pm})$	0.512	0.086
$\pi^+ IP\chi^2$	0.022	0.008

Table 5.13: Variable importance for DD and LL classifier.

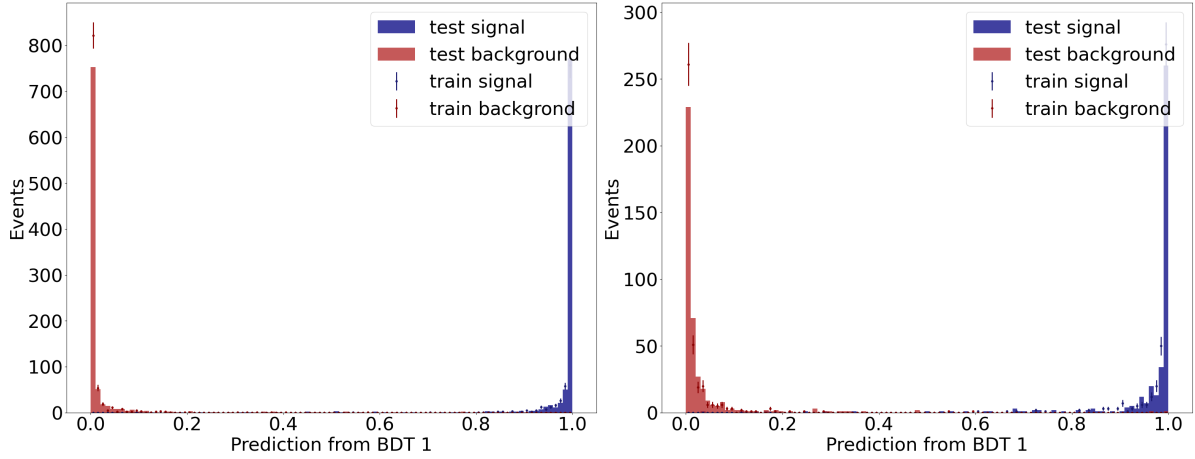


Figure 5.10: The BDT prediction for testing sample: DD classifier (left), LL classifier (right).

The correlation plots for signal and background are given in Fig. 5.12 and Fig. 5.14. Because correlations between variables can lead to an overly complicated model with lower efficiency of the classifier, the correlations between variables should remain below 60% unless the dependence between variables is well known.

A confusion matrix technique was used to test the performance of the classifier. A comparison was made between the predictions from the classifier and the actual labels for all testing events. Selected metrics were calculated explicitly. The true positive

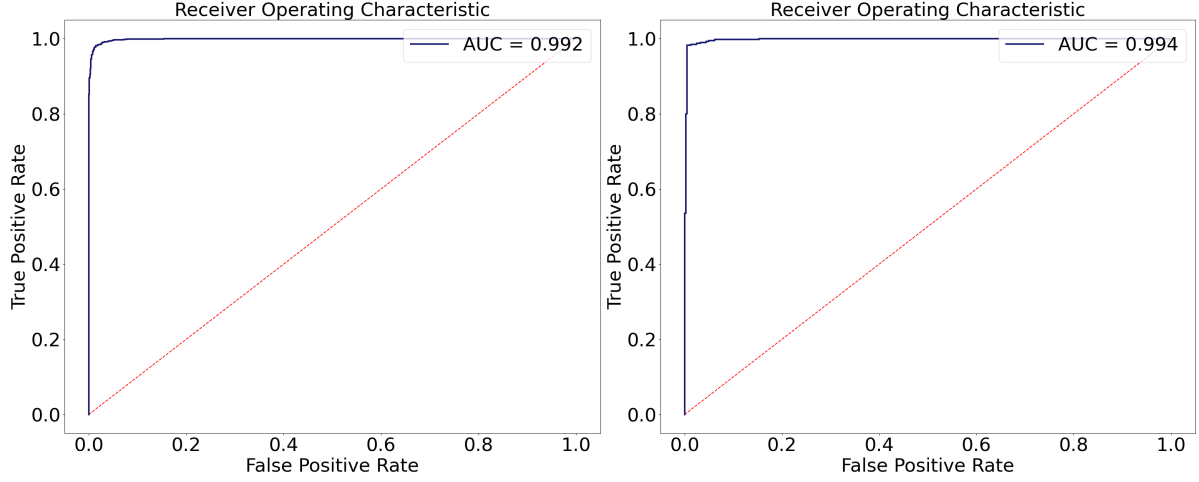


Figure 5.11: ROC curve: DD classifier (left), LL classifier (right).

(TP) and true negative (TN) events were correctly identified. Misclassification results in false positive (FP) and false negative (FN) events. *Accuracy* represents how often a classifier is correct. *Misclassification rate* defines how frequently the classifier is wrong and is equivalent to $1 - Accuracy$. *True Positive Rate* (TPR) describes how often the classifier predicts a signal for the event, which was a signal event and is also known as *Sensitivity* or *Recall*. *False Positive Rate* (FPR) describes how frequently the classifier predicts signal class in case of a background event. *True Negative Rate* - how often the classifier determines that a background event is a background and is equivalent to $1 - False Positive Rate$; also known as *Specificity*.

Fig. 5.11 presents the TPR to FPR curve for the classifier of downstream tracks and long tracks. This curve is called the ROC curve (*Receiver operating characteristic*). The area under the curve (AUC) for random classification is around 0.5. For perfect classification is equal to 1.

The final check was studies of classification loss (Fig. 5.13) and AUC (Fig. 5.15) in the function of numbers of trained trees during the training of classifiers for both classifiers. There is a visible reduction of classification loss and an increase in AUC with the evolution of the classifier. Because there is no overfitting effect, the result for the test sample is slightly worse than for the training samples, which is expected during classifier training.

The working point of the trained model was selected to be $BDT > 0.9$, which is another criterion of data selection, was estimated using a comparison of BDT response for signal and background training sample (Fig. 5.10).

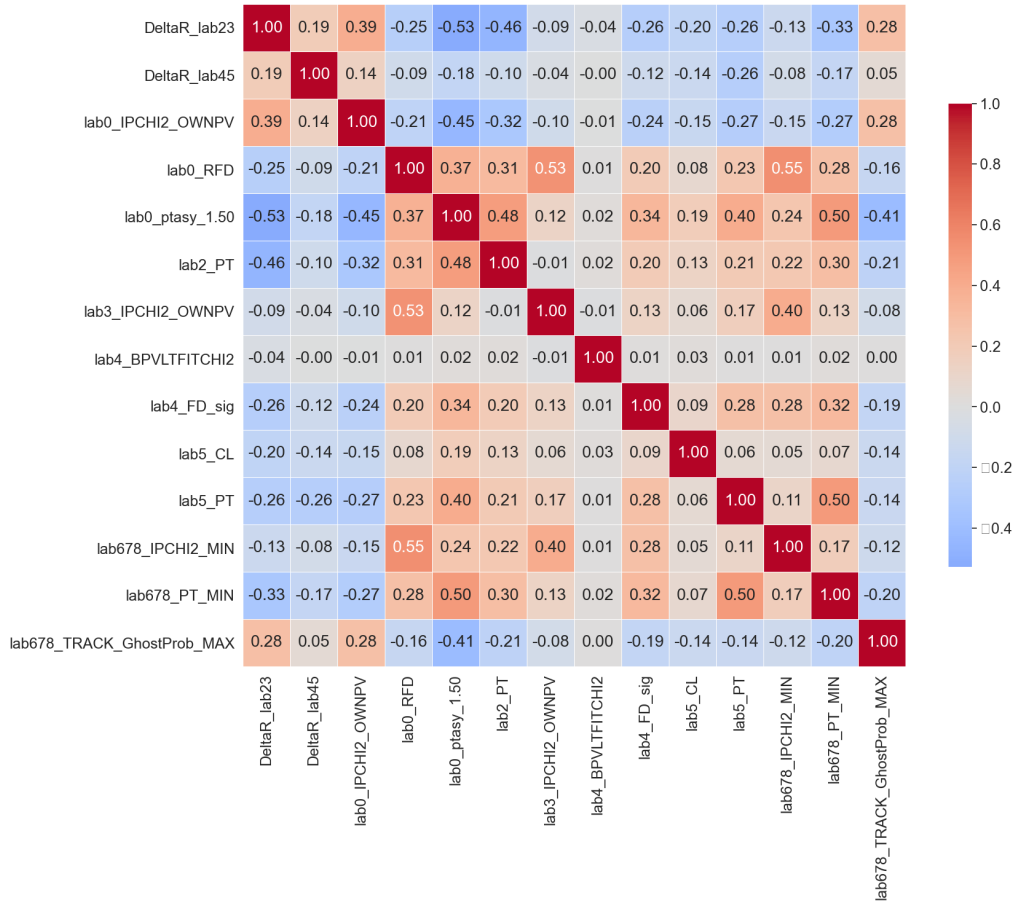


Figure 5.12: Correlation matrix for DD classifier.

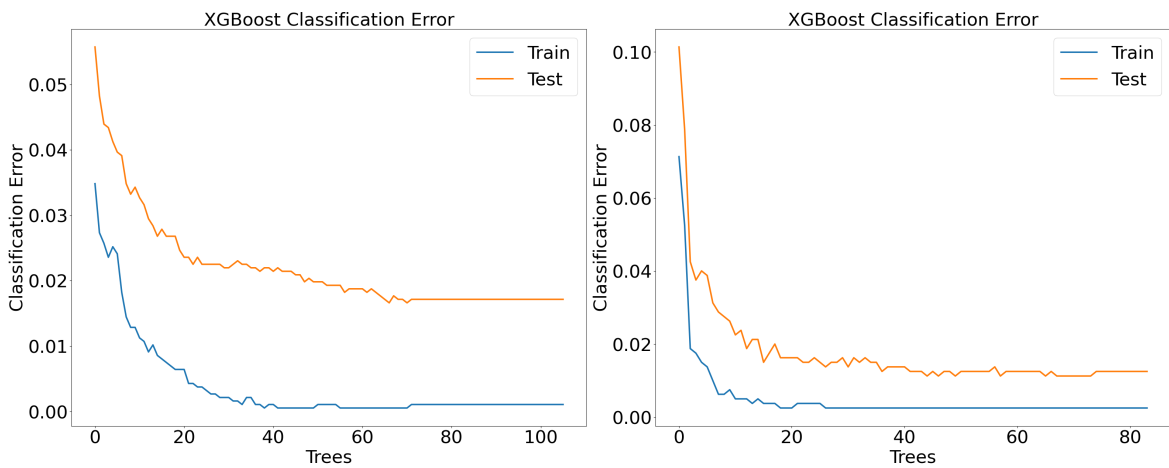


Figure 5.13: Classification error in the function of trained trees: DD classifier (left), LL classifier (right).

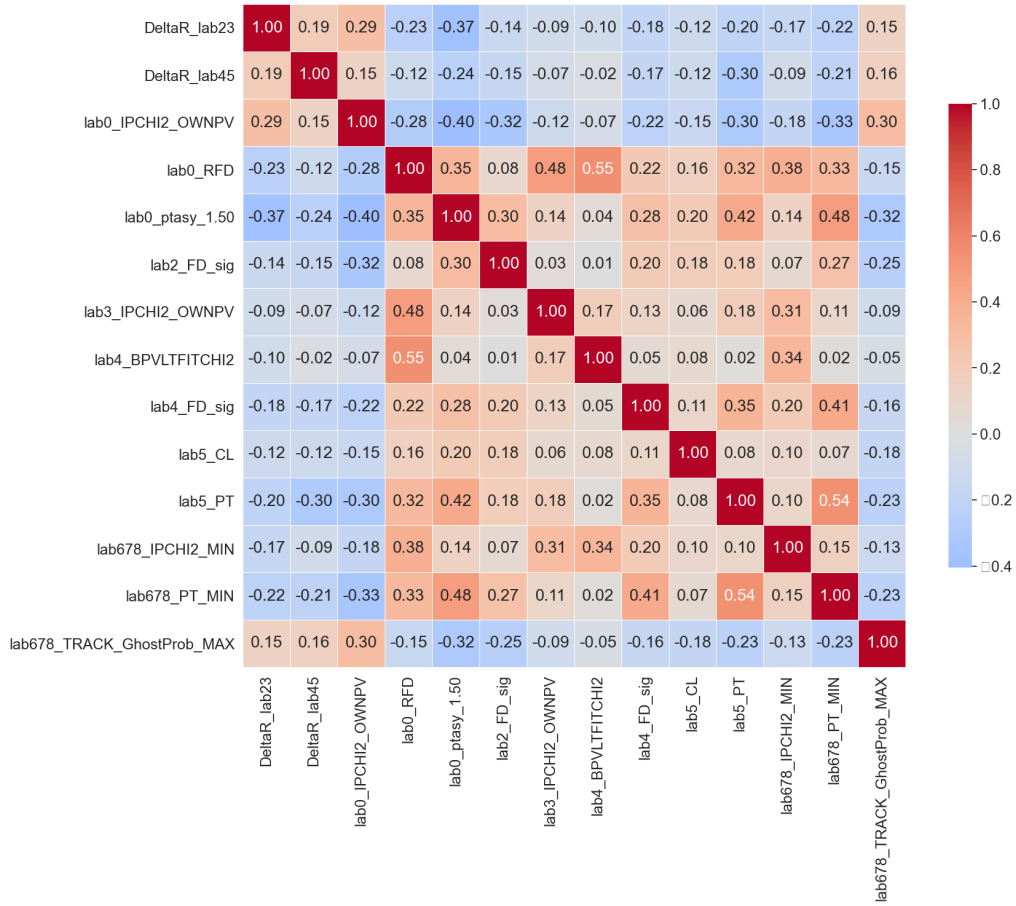


Figure 5.14: Correlation matrix for LL classifier.

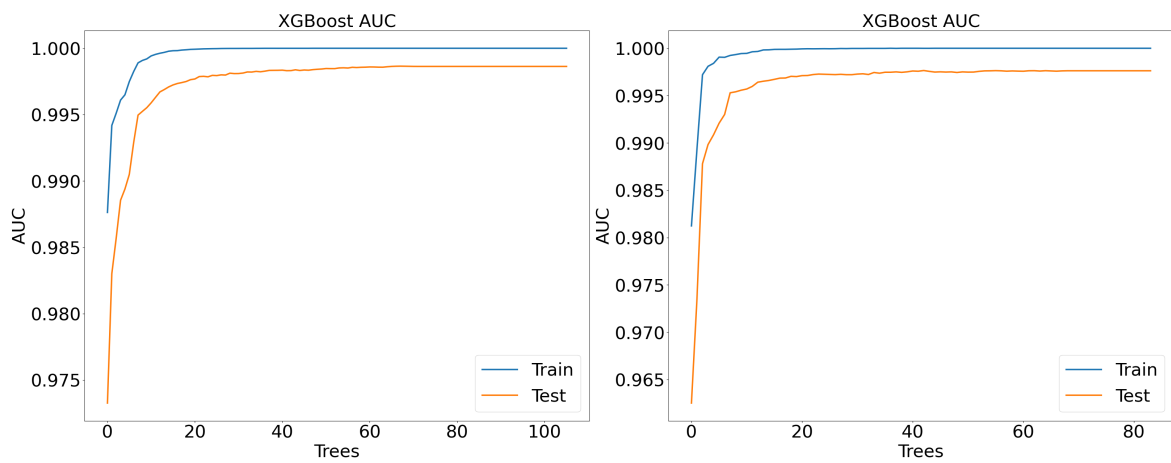


Figure 5.15: AUC in the function of trained trees: DD classifier (left), LL classifier (right).

5.8 Post-BDT studies

The post-BDT selection consists of the application of the BDT and more tight identification cuts on D_s^+ final states. These requirements allow for the final reduction of combinatorial background. The ProbNN variable is described in Sec. 5.4 allows for further suppression of wrongly reconstructed D_s^+ .

	Description	Requirement	Modes
	BDT	> 0.9	all
D_s^+	ProbNNK(K)	> 0.15	all
	ProbNNpi(π)	> 0.15	all
$K^{*\pm}$	$m(K_S^0 \pi^\pm) - m_{PDG}(K^{*\pm})$	$< 75 \text{ MeV}/c^2$	$B_s^0 \rightarrow D_s^{*\mp} K^{*\pm}$ $B^0 \rightarrow D_s^{*\mp} K^{*\pm}$
D^-	$m(K_S^0 \pi^\pm) - m_{PDG}(D^-)$	$< 30 \text{ MeV}/c^2$	$B^0 \rightarrow D^- D_s^\pm$

Table 5.14: Post-BDT selection.

During further studies, no additional requirements were imposed apart from mass windows for selection of $K^{*\pm}$ or D^- , detailed in the Sec. 5.9. Results presented in this and the following chapter are based on the data set after full offline selection, including the BDT cut.

Several cross-checks were performed to ensure that selected candidates are suitable for the further part of the analysis, including fit to mass distribution of candidates. These cross-checks comprised, among others, the comparison of simulated events and data and studies of resonance and were divided into these related to $D_s^{*\mp}$ ($D_s^{*\mp} \rightarrow D_s^\mp \gamma$) and $K^{*\pm}$ ($K^{*\pm} \rightarrow K_S^0 \pi^\pm$).

5.8.1 Studies of $D_s^{*\mp}$ and D_s^+

The study of the radiative decay of $D_s^{*\mp}$ to D_s^+ meson and its decay to three hadrons showed intermediate resonances like $\phi(1020)$ with $D_s^+ \rightarrow (\phi \rightarrow K^+ K^-) \pi^+$ and $K^*(892)^0$ with $D_s^+ \rightarrow (K^*(892)^0 \rightarrow K^- \pi^+) K^+$.

Fig. 5.16 (top) shows the $K^+ K^-$ mass distribution with a Gaussian peak which confirms the clear signal from $\phi(1020) \rightarrow K^+ K^-$. Mass of $K^- \pi^+$ system with a fit showing $K^*(892)^0 \rightarrow K^- \pi^+$ contribution is depicted in Fig. 5.16 (bottom). The mean values taken from the fits to mass distributions of $\phi(1020)$ and $K^*(892)^0$: 1019.60 ± 0.046 and 892.35 ± 0.42 agree with mass of $\phi(1020)$ and $K^*(892)^0$ taken from PDG [2]

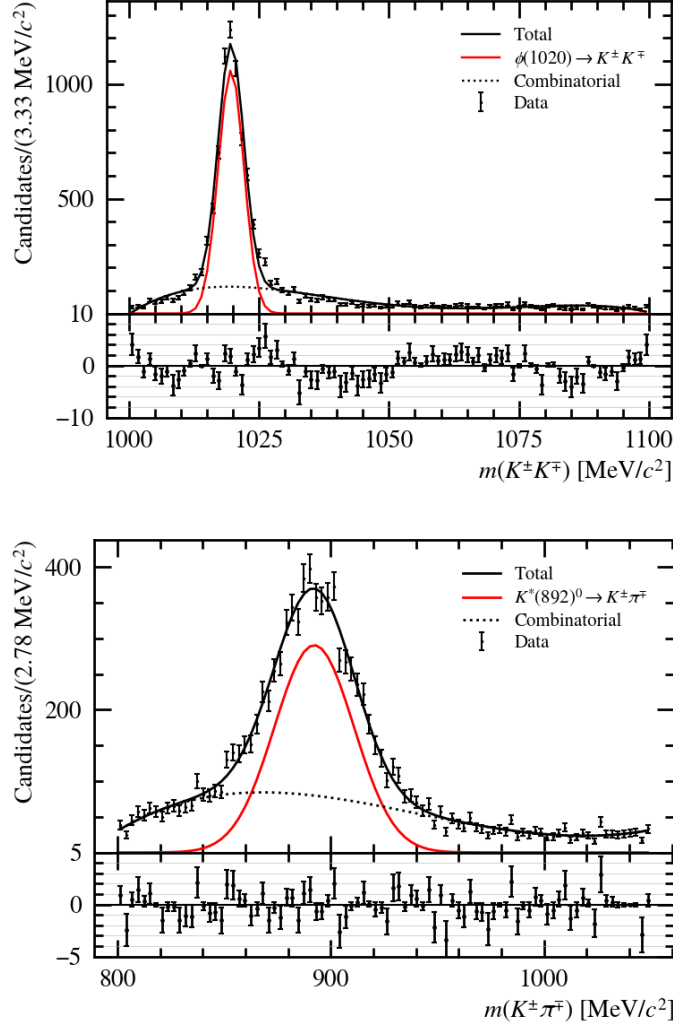


Figure 5.16: Invariant mass distribution of K^+K^- candidates from $D_s^+ \rightarrow K^+K^-\pi^-$ with visible contribution from $\phi(1020)$ with Gaussian fit (top), invariant mass distribution of $K^+\pi^-$ candidates from $D_s^+ \rightarrow K^+K^-\pi^+$ with visible contribution from K^{*0} and the fit (bottom).

within uncertainties (Tab. 5.15).

The invariant mass distribution of $K^+K^-\pi^+$ and $D_s^\mp\gamma$ have been inspected to ensure that they comprise only D_s^\mp and $D_s^{*\mp}$ contribution without a significant amount of combinatorial background (Fig. 5.17). There is sufficient agreement between fits that consist of a Gaussian distribution only and data, which presumes that events in the data sample contain mostly physical D_s^\mp and D_s^+ . The mean values taken from the fits to invariant mass distributions of $K^+K^-\pi^+$ and $D_s^\mp\gamma$: 1968.88 ± 0.19 and 2112.97 ± 0.21 agree with mass of D_s^\mp and D_s^+ taken from PDG [2] within uncertainties (Tab. 5.15).

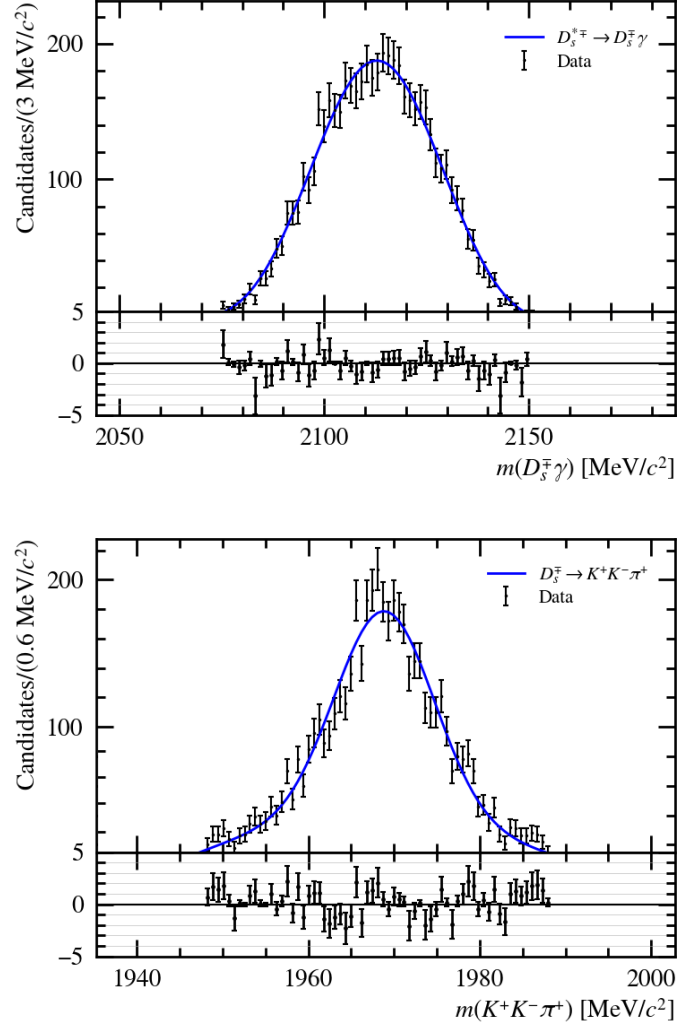


Figure 5.17: Mass distribution of $D_s^+ \rightarrow K^+ \pi^- \pi^-$ candidates with a Gaussian fit (top), mass distribution of $D_s^{*\mp} \rightarrow D_s^\mp \gamma$ candidates with a Gaussian fit (bottom).

Fig. 5.16, Fig. 5.17, as well as other histograms which include fit to invariant mass distribution, contain histograms which describe the difference between model and data points normalised to the uncertainty of the data points (so-called *pull histogram*):

$$pull(i) = \frac{N_i^{Data} - N_i^{Fit}}{\sigma(i)}, \quad (5.5)$$

$$\sigma(i) = \sqrt{N_i^{Data}} \quad (5.6)$$

where i is a bin in the histogram, this distribution describes the fit's quality and how well it models data.

5.8.2 Studies of $K^{*\pm}$

The invariant mass of $K_S^0\pi^+$ system was investigated in a range of 700-1100 MeV/c^2 and 1800-1950 MeV/c^2 (these ranges were chosen after preliminary studies of this spectrum during the development of selection criteria in Sec. 5.6), which apparently included contributions of $K^{*\pm}$ and D^- (Fig. 5.18) visible after the BDT cut. The invariant mass of $K_S^0\pi^+$ in these ranges was fitted with a model, which included a signal modelled by a Gaussian distribution and combinatorial background described by polynomial function or convolution of a polynomial function and Gaussian distribution.

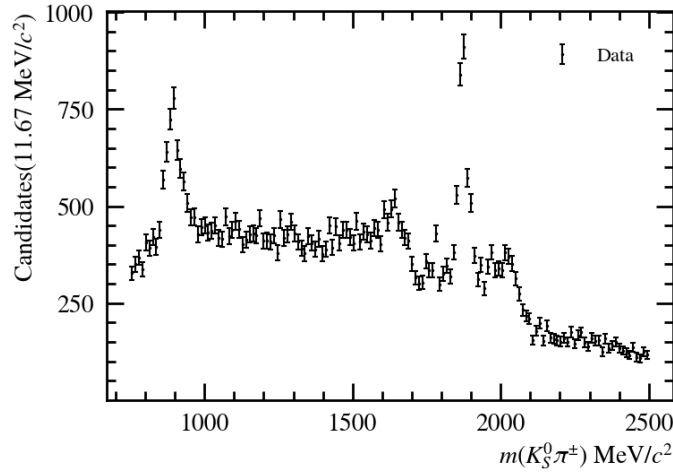


Figure 5.18: Invariant mass of $K_S^0\pi^+$ candidates after full selection.

Fig. 5.19 shows that contribution from $K^{*\pm}$ is visible. The parameters of signal fit - Gaussian distribution (width and mean value) were taken from the distribution of $K^{*\pm}$ candidates for simulated events. There is a sufficient agreement between fit and invariant mass distribution $K_S^0\pi^+$ in a range of 700-1100 MeV/c^2 .

Similarly, Fig. 5.20 shows that visible contribution from D^- , which was investigated for $B^0 \rightarrow D^- D_s^{*+}$ studies. The significance of D^- signal is better than for $K^{*\pm}$. Again, further studies will require a non-resonance $K_S^0\pi^+$ sample.

The mean values taken from the fits to mass distributions of $K^{*\pm}$ and D^- : 891.51 ± 0.16 and 1870.75 ± 0.51 agree with mass of $K^{*\pm}$ and D^- taken from PDG [2] within uncertainties (Tab. 5.15).

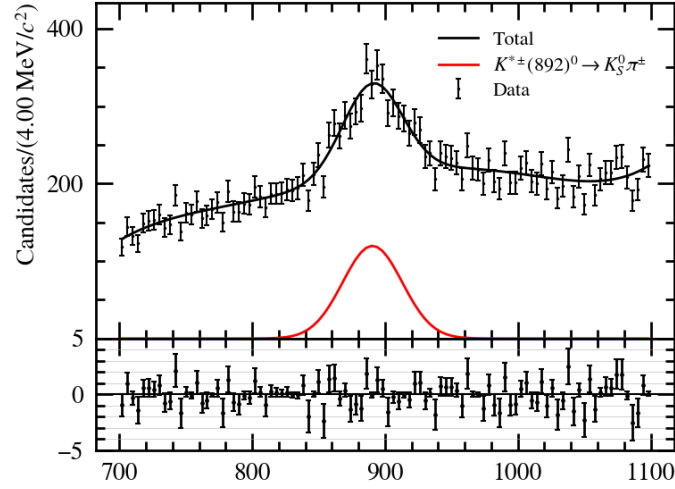


Figure 5.19: Invariant mass distribution of $K_S^0 \pi^+$ candidates in a range of 700-1100 MeV/c^2 with the fit.

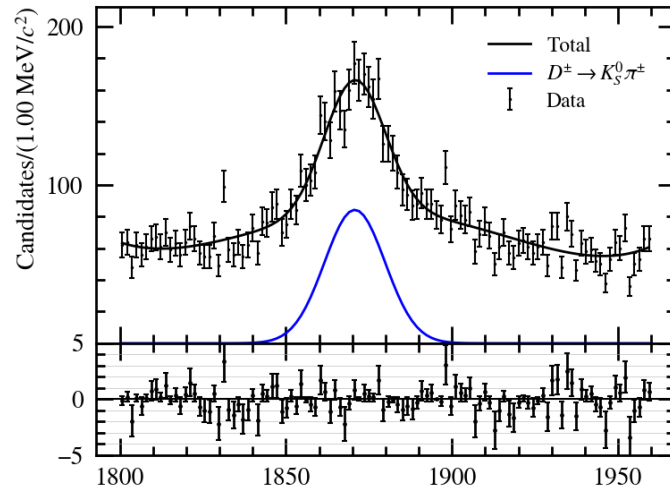


Figure 5.20: Invariant mass distribution of $K_S^0 \pi^+$ candidates in a range of 1800-1950 MeV/c^2 with the fit.

Particle	Mass (Fit) [MeV/ c^2]	Mass (PDG) [MeV/ c^2]	Width (Fit) [MeV/ c^2]
D_s^+	1968.88 ± 0.19	1968.35 ± 0.07	5.77 ± 0.24
$D_s^{*\mp}$	2112.97 ± 0.21	2112.20 ± 0.04	17.41 ± 0.21
$K^{*\pm}$	891.51 ± 0.16	891.66 ± 0.26	22.43 ± 2.03
D^-	1870.75 ± 0.51	1869.55 ± 0.05	9.12 ± 0.68
$K^*(892)^0$	892.35 ± 0.42	895.81 ± 0.18	18.68 ± 0.51
$\phi(1020)$	1019.60 ± 0.046	1019.46 ± 0.02	2.46 ± 0.05

Table 5.15: Comparison of mean value and width taken from fit to invariant mass distribution with the mass of particles taken from PDG [2] (resonances and intermediate states).

5.9 Towards branching fraction measurement

The direct measurement of any exclusive decay like $B \rightarrow DK$ on a proton-proton accelerator requires detailed studies of efficiency and knowledge of total proton-proton and B meson production cross-section. This procedure is usually very complicated; therefore, it is more efficient to evaluate the branching fraction of signal mode (usually small), with respect to another process (called *control channel*) which has a measured branching fraction and similar topology with the signal process. The most useful control channels differ in one particle from the discussed signal process, like $(K-\pi)$ or type of B meson ($B^0-B_s^0$), but other modes which have the similar topology of decay and the final state as a signal mode can be considered. In this study, several control channels were investigated:

- $B^0 \rightarrow D_s^{*\mp} K^{*\pm}$ ($D_s^{*\mp} \rightarrow D_s^{\mp} \gamma$, $D_s^{\mp} \rightarrow hhh$, $K^{*\pm} \rightarrow K_S^0 \pi^{\pm}$)
- $B_s^0 \rightarrow D_s^{*\mp} \pi^{\pm}$ ($D_s^{*\mp} \rightarrow D_s^{\mp} \gamma$, $D_s^{\mp} \rightarrow hhh$)
- $B^0 \rightarrow D^- D_s^{*+}$ ($D_s^{*\mp} \rightarrow D_s^{\mp} \gamma$, $D_s^{\mp} \rightarrow hhh$, $D^- \rightarrow K_S^0 \pi^{\pm}$)

where h stands for charged K or π .

The branching fractions for control channel decays are presented in Tab. 5.16. These modes were chosen due to their similarity to the signal $B_s^0 \rightarrow D_s^{*\mp} K^{*\pm}$ decay.

Mode	BR	Comment
$B^0 \rightarrow D_s^{*\mp} K^{*\pm}$	$(3.5 \pm 1.0) \times 10^{-5}$ [124]	The same final state
$B^0 \rightarrow D^- D_s^{*+}$	$(7.4 \pm 1.6) \times 10^{-3}$ [125]	The same final state
$B_s^0 \rightarrow D_s^{*\mp} \pi^{\pm}$	$(3.2_{-1.5}^{+1.3}) \times 10^{-5}$ [126]	Similar final state

Table 5.16: Branching fractions of candidates for control channel [2].

The first process $B^0 \rightarrow D_s^{*\mp} K^{*\pm}$ was measured by the BaBar collaboration using a sample of 381 million $\Upsilon(4S)$ decays into $B\bar{B}$ pairs collected at the PEP-II asymmetric-energy e^+e^- storage ring [124]. The advantage of this mode is that $B_s^0 \rightarrow D_s^{*\mp} K^{*\pm}$ and $B^0 \rightarrow D_s^{*\mp} K^{*\pm}$ have the same final states; however, the branching fraction of $B^0 \rightarrow D_s^{*\mp} K^{*\pm}$ decay ($(3.5 \pm 1.0) \times 10^{-5}$) is relatively small which may make it difficult to observe it using data sample collected so far by LHCb collaboration.

Fig. 5.21 shows fit to invariant mass distribution of $D_s^{*\mp} K^{*\pm}$ candidates after full selection. The signal region of $B_s^0 \rightarrow D_s^{*\mp} K^{*\pm}$ is blinded due to ongoing analysis, but

the contribution of $B^0 \rightarrow D_s^{*\mp} K^{*\pm}$ is visible. The fit to this distribution consists of Gaussian distribution, which models the signal contribution and polynomial function, which describes the combinatorial background. From the fit to signal contribution, the total number of 26 $B^0 \rightarrow D_s^{*\mp} K^{*\pm}$ decays was obtained.

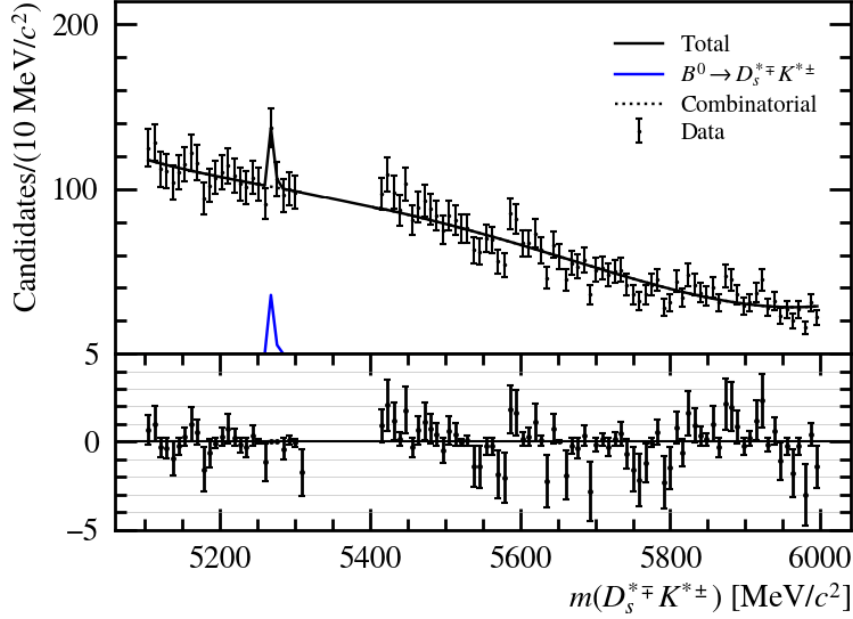


Figure 5.21: Invariant mass distribution of $D_s^{*\mp} K^{*\pm}$ candidates after full selection with the fit. The signal region of $B_s^0 \rightarrow D_s^{*\mp} K^{*\pm}$ is blinded due to ongoing analysis. The lower part of each figure shows the residual of the data points with respect to the fit, normalised to the uncertainty of the data points.

Another promising candidate for the control channel is $B_s^0 \rightarrow D_s^{*\mp} \pi^\pm$ which decays to the same final state as $B_s^0 \rightarrow D_s^{*\mp} K^{*\pm}$ except the presence of K_S^0 . Lack of K_S^0 in the reconstruction procedure results in higher efficiency, and even if the BF is similar to the control channel, the number of expected candidates is much higher. Full LHCb Run 1 and Run 2 data sample was investigated using the same selection procedure as for $B_s^0 \rightarrow D_s^{*\mp} K^{*\pm}$ (excluding cuts concerning K_S^0). The BDT classifier was trained using a sample of $B_s^0 \rightarrow D_s^{*\mp} \pi^\pm$ simulated events and data. Invariant mass distribution of $D_s^{*\mp} \pi^\pm$ candidates with fit is shown in Fig. 5.22. The composition of the mass fit is similar to the one for $B_s^0 \rightarrow D_s^{*\mp} K^{*\pm}$. The studies of $B_s^0 \rightarrow D_s^{*\mp} \pi^\pm$ allow obtaining a total number of 50973 events calculated from fit to mass distribution of $B_s^0 \rightarrow D_s^{*\mp} \pi^\pm$ candidates.

The next candidate for the control channel is $B^0 \rightarrow D^- D_s^{*+}$. Candidates for this

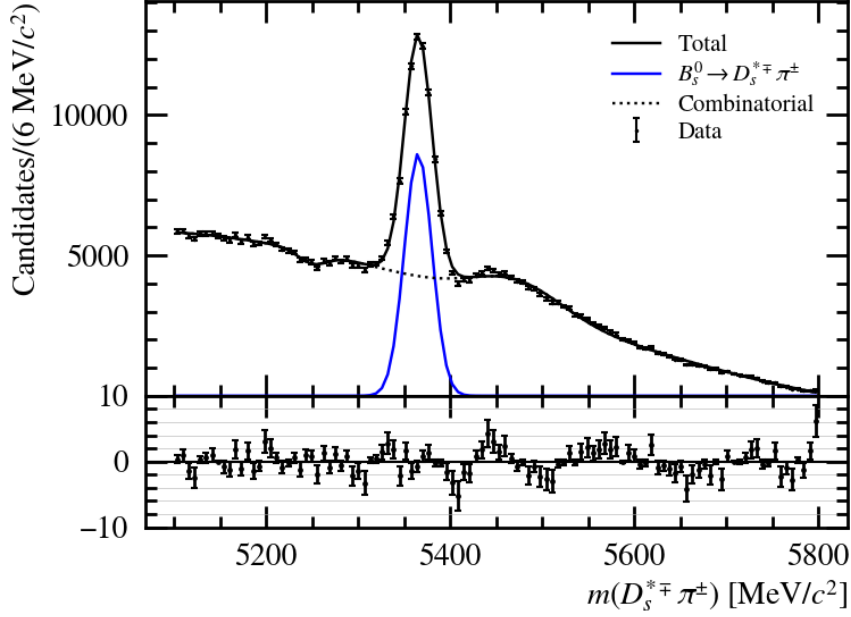


Figure 5.22: Invariant mass distribution of $D_s^{*+}\pi$ candidates after full selection with the fit of the background and signal of $B_s^0 \rightarrow D_s^{*\mp}\pi^\pm$ decay. The lower part of each figure shows the residual of the data points with respect to the fit, normalised to the uncertainty of the data points.

process was chosen by application of $m(K_S^0\pi^\pm) - m_{PDG}(D^-) < 30 \text{ MeV}/c^2$ cut (30 MeV/c^2 D^- mass windows). The invariant mass distribution of $D^-D_s^{*+}$ candidates with the fit is presented in Fig. 5.22. There is a visible $B^0 \rightarrow D^-D_s^{*+}$ contribution with the combinatorial background. Again, the fit to mass distribution consists of Gaussian distribution (signal) and polynomial function (background). The total number of $B^0 \rightarrow D^-D_s^{*+}$ candidates estimated from the fit is 310.

In Fig. 5.21-5.23 histograms showing difference between model and data points normalised to the uncertainty of the data points are also depicted. A visible increase in pull for bins corresponding to higher mass (above $5700 \text{ MeV}/c^2$) is a result of a smaller number of candidates. Higher pulls in the signal region show that a model for the mass fit has to be revised. Currently, it cannot be done because of the lack of appropriate MC samples.

The mean values taken from the fits to mass distributions of control channels agree with the mass of B_s^0 and B^0 taken from PDG [2] (Tab. 5.17).

The main aim of this study was to prove the feasibility of the observation of the $B_s^0 \rightarrow D_s^{*\mp} K^{*\pm}$ in the LHCb experiment. Therefore the selection was done on the control

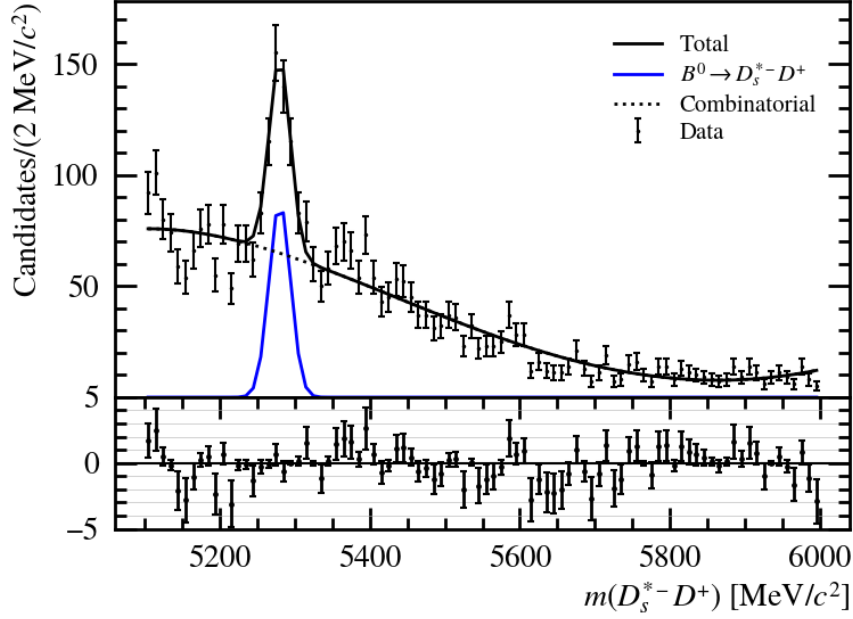


Figure 5.23: Invariant mass distribution of $D^- D_s^{*+}$ candidates after full selection with the fit. Fit shows $B^0 \rightarrow D^- D_s^{*+}$ candidates and background. The lower part of each figure shows the residual of the data points with respect to the fit, normalised to the uncertainty of the data points.

channels to test, whereas the whole procedure leads to a proper observation.

The last step of this analysis is to show the agreement between several parameters describing data and MC for selected candidates in the case of the control channel $B_s^0 \rightarrow D_s^{*+} \pi^-$ (signal region for $B_s^0 \rightarrow D_s^{*\mp} K^{*\pm}$ is blinded). Selected variables refer to the kinematic and topological properties of the decay. Sufficient agreement obtained between the data (blue points) and simulated events (blue bars) is evidence of the effectiveness of the selection. The comparison is presented in Fig. 5.24. Similar studies will be performed for signal mode after unblinding of the signal region.

Particle	Mass (Fit) [MeV/ c^2]	Mass (PDG) [MeV/ c^2]	Width (Fit) [MeV/ c^2]
$B^0 (D_s^{*\mp} K^{*\pm})$	5279.00 ± 4.65	5279.66 ± 0.12	3.67 ± 4.75
$B_s^0 (D_s^{*\mp} \pi^\pm)$	5365.32 ± 0.14	5366.92 ± 0.10	1.5 ± 0.15
$B^0 (D^- D_s^{*+})$	5280.32 ± 1.20	5279.66 ± 0.12	14.28 ± 1.30

Table 5.17: Comparison of mean value and width taken from fit to invariant mass distribution with the mass of particles taken from PDG [2] (control channels).

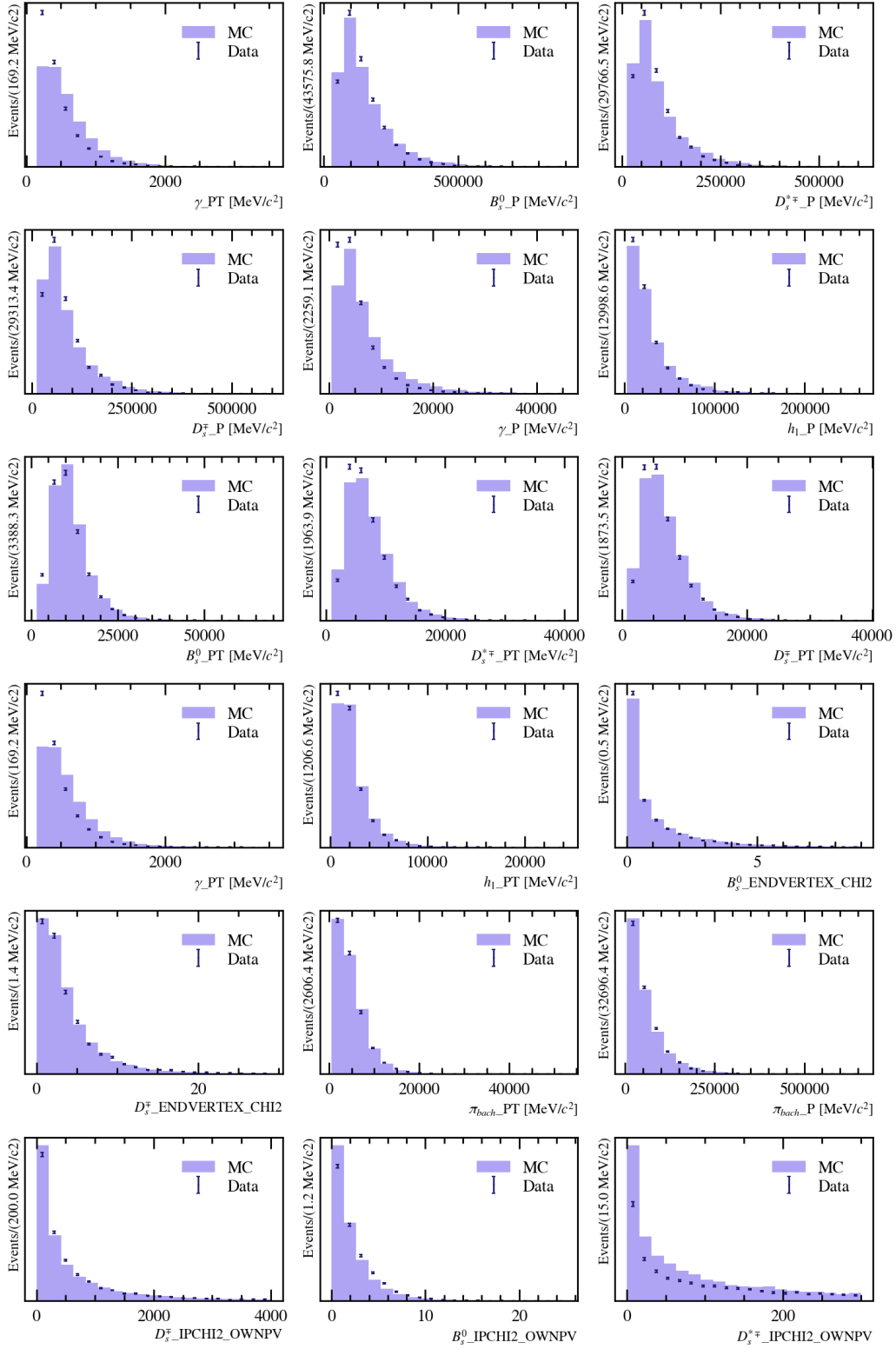


Figure 5.24: Comparison of simulated events (blue bars) and data after selection (blue points) for $B_s^0 \rightarrow D_s^{*\mp} \pi^\pm$ channel. Definitions of the variables can be found in Sec. 5.6.

Chapter 6

Conclusions

The final chapter provides a discussion about the results presented in this thesis, as well as the prospects for further studies.

6.1 Summary

In this thesis, the full Run 1 and Run 2 data sample from the LHCb experiment corresponding to the total integrated luminosity 6.0 fb^{-1} was investigated to develop the analysis for the first observation of the $B_s^0 \rightarrow D_s^{*\mp} K^{*\pm}$ decay. The core part of the analysis is a selection algorithm based on the topological and kinematic properties of the mother and daughter particles. The effectiveness of the selection was verified by studies of mass distribution of chosen control channels, resonance states $K^{*\pm}$ and $D_s^{*\mp}$, comparison of simulated events and data for selected variables and studies of the efficiency of selection criteria using simulated events. It also comprises analysis of decays of D_s^+ mesons through resonance states $\phi(1020)$ and $K^*(892)^0$ and elements of multivariate analysis - selection of candidates using boosted decision trees. Its effectiveness was proven by, among others, studies of the confusion matrix and ROC curve. No overfitting effect was observed. Fit to mass distribution of resonance ($\phi(1020)$, $K^*(892)^0$, $D_s^{*\mp}$, $K^{*\pm}$) and intermediate states (D_s^+ , D^- , K_S^0) allowed for the extraction of physical variables like the mass of particles which were compared with theoretical value and agree within uncertainties. Several decay modes: $B^0 \rightarrow D_s^{*\mp} K^{*\pm}$, $B_s^0 \rightarrow D_s^{*\mp} \pi^\pm$, and $B^0 \rightarrow D^- D_s^{*+}$ were investigated to check their capacity to be control channels for $B_s^0 \rightarrow D_s^{*\mp} K^{*\pm}$ measurement. In each case, obtained results provided compelling evidence for using decay in branching fraction measurement.

Working on detector software during the commissioning of the LHCb spectrometer

provides a unique possibility for the development of a new software environment which has to include different aspects of the detector's performance and meet the challenges related to the upcoming data-taking period. The Titania-UT interface software, initially developed by the VELO group, was adjusted to provide monitoring plots for UT, including monitor of all plains at once. Vetra, designed to handle full DSP chain for many ASICs at once, has demonstrated its effectiveness during tests on data from UT test staves by successive decoding of raw data and calculating test sensor parameters like noise or pedestals. The platform has also been adapted to cover special runs like trimDAC. In effect the Author became a key software expert during the commissioning of the UT detector.

6.2 Future outlook

The studies of control channel candidates, especially $B^0 \rightarrow D_s^{*\mp} K^{*\pm}$ provide convincing evidence for the possibility of observation of $B_s^0 \rightarrow D_s^{*\mp} K^{*\pm}$ decay. Further studies are ongoing, including the selection of a control channel, unblinding of the signal region, PID corrections [127], calculation of total efficiency and branching ratio measurement. Imminent start of Run 3 for the LHC provide opportunities for more precise time-dependent CKM angle γ measurement in LHCb like [128], [129], [130] and new one using new decay mode like $B_s^0 \rightarrow D_s^{*\mp} K^{*\pm}$.

In the UT detector software area, ongoing commissioning provides early data from the operational UT sensors, which will soon include data from whole UT staves and different e-ports configurations. Full UT software's commissioning implies simultaneous analysis of the full calibration data sample, including all UT sensors at once. The new data set will allow debugging and testing the performance of software for UT and verifying the detector's performance. Futures plans, including developing the algorithm for preparing SALT's configuration file and UT database. The next objective is to continue working on an algorithm that autonomously makes detector calibration decisions. Until now, two different algorithms were tested. The first is Principal Component Analysis (PCA, [131]), and the other is Variational Autoencoders (VAE, [132]). Preliminary tests provided promising results. As mentioned in Sec. 4.8, the UT group must provide monitoring plots to the LHCb central monitoring system. Because both applications, Titania and Monte, are written in Python, monitoring plots from Titania should be easily transferable to Monet.

Appendix A

Particle	Variable	Criteria
π or K	p_T	$> 100 \text{ MeV}/c^2$
	p	$> 1000 \text{ MeV}/c^2$
	min(IP)	> 4
	track ghost prob.	< 0.4
D_s^+	$\sum p_T$	$> 1800 \text{ MeV}/c^2$
	m	$\in (1910, 2030) \text{ MeV}/c^2$
	DOCA (1st (2nd) and 3rd daugh.)	$< 0.5 \text{ mm}$
	or has daughter:	is K_S^0 & BDVVDCHI2 > 1000
	BPVVDCHI2	> 36
	Vertex χ^2/ndf	< 10
	BDVDIRA	> 0
	not in tree:	$p(K)$ & PIDp(K) < -5
not in tree:	π & PID(K) > 10	
γ	p_T	$> 145 \text{ MeV}/c^2$
	CL	> 0.25
D_s^{*+}	$ \Delta_M $	$\in (80, 250) \text{ MeV}/c^2$
π (from B_s^0)	p_T	$> 500 \text{ MeV}/c^2$
	p	$> 5000 \text{ MeV}/c^2$
	min(IP)	> 4
	track ghost prob.	< 0.4
	PIDK(K)	< 20
B_s^0	track: χ^2/ndf	< 4
	DIRA	> 0.999
	τ	$> 0.2 \text{ ps}$
	IP χ^2	< 25
	Vertex χ^2/ndf	< 10
	m	$\in (5000, 6000) \text{ MeV}/c^2$
	has daughter	p $> 10000 \text{ MeV}/c^2$
		p_T $> 1700 \text{ MeV}/c^2$
		track: χ^2/ndf < 4
		min(IP) > 16
	has daughter	p $> 5000 \text{ MeV}/c^2$
		p_T $> 500 \text{ MeV}/c^2$
		track: χ^2/ndf < 4
or has daughter	p_T $> 500 \text{ MeV}/c^2$	
	p $> 5000 \text{ MeV}/c^2$	
	BPVVDCHI2 > 1000	
	track: χ^2/ndf < 4	
K_S^0 DD(LL)	p_T	$> 250 (> 0) \text{ MeV}/c^2$
	m	$\in (467, 527) \text{ MeV}/c^2$

Table A.1: Description of B02DsstKsPiDD(LL)Dsst2DGammaD2HHHBeauty2CharmLine line.

Bibliography

- [1] Matt Strassler, *Protons and neutrons: The massive pandemonium in matter*, <https://profmattstrassler.com/articles-and-posts/particle-physics-basics/the-structure-of-matter/protons-and-neutrons/>.
- [2] Particle Data Group, Zyla, P. A. and others, *Review of Particle Physics*, PTEP **2020** (2020), no. 8 083C01.
- [3] D. Gossman, *Measurement of the higgs boson transverse momentum and its sensitivity to new physics beyond the standard model*, Journal of Physics: Conference Series **645** (2015) 012010.
- [4] LHCb Collaboration, R. Aaij *et al.*, *Observation of CP violation in charm decays*, Phys. Rev. Lett. **122** (2019) 211803. 12 p, [arXiv:1903.08726](https://arxiv.org/abs/1903.08726).
- [5] LHCb collaboration, Meier, Frank, *CPV in beauty decays with LHCb*, PoS **LHCP2016** (2016) 074.
- [6] Padmanabhan, T, *Combining general relativity and quantum theory: points of conflict and contact*, Classical and Quantum Gravity **19** (2002) 3551–3566.
- [7] D. Boubaa, G. Faisel, and S. Khalil, *Beyond SM Physics and searches for SUSY at the LHC*, May, (2020). [arXiv:2005.08069](https://arxiv.org/abs/2005.08069).
- [8] H. E. Haber and L. Stephenson Haskins, *Supersymmetric Theory and Models*, in *Theoretical Advanced Study Institute in Elementary Particle Physics: Anticipating the Next Discoveries in Particle Physics*, pp. 355–499, WSP, 2018. [arXiv:1712.05926](https://arxiv.org/abs/1712.05926).
- [9] A. D. Sakharov, *Violation of CP Invariance, C asymmetry, and baryon asymmetry of the universe*, Pisma Zh. Eksp. Teor. Fiz. **5** (1967) 32.

-
- [10] LHCb collaboration, F. Meier, *CPV in beauty decays with LHCb*, PoS **LHCP2016** (2016) 074.
- [11] L. Wolfenstein, *Parametrization of the Kobayashi-Maskawa Matrix*, Phys. Rev. Lett. **51** (1983) (1945).
- [12] LHC collaborations, *LHC Top Working Group summary plots, single top quark production*, 101, (2017).
- [13] CMS collaboration, V. Khachatryan *et al.*, *Measurement of the ratio $\mathcal{B}(t \rightarrow Wb)/\mathcal{B}(t \rightarrow Wq)$ in pp collisions at $\sqrt{s} = 8$ TeV*, Phys. Lett. B **736** (2014) 33, arXiv:1404.2292.
- [14] LHCb Collaboration, R. Aaij *et al.*, *Simultaneous determination of CKM angle γ and charm mixing parameters*, Journal of High Energy Physics **2021** (2021) , arXiv:2110.02350.
- [15] *Current status of the standard model CKM fit and constraints on $\Delta F=2$ new physics*, vol. 91, American Physical Society (APS), Apr, 2015. doi: 10.1103/phys-revd.91.073007.
- [16] Brod, Joachim and Zupan, Jure, *The ultimate theoretical error on γ from $B \rightarrow DK$ decays*, Journal of High Energy Physics **2014** (2014) , arXiv:1308.566.
- [17] CKMfitter Group, Charles, J. *et al.*, *CKMfitter Group - updated results and plots*, Eur. Phys. J. C41, 1-131 (2005) **C41**.
- [18] *On determining a weak phase from charged B decay asymmetries*, vol. 265, (1991). doi: 10.1007/jhep01(2014)051.
- [19] *Improved methods for observing CP violation in $B^\pm KD$ and measuring the CKM phase γ* , no. 3, American Physical Society (APS), Jan, (2001). doi: 10.1103/phys-revd.63.036005.
- [20] *Determining γ using $B^\pm \rightarrow DK^\pm$ with multibody D decays*, vol. 68, American Physical Society (APS), Sep, (2003). doi: 10.1103/physrevd.68.054018.
- [21] LHCb, D. Fazzini, *Flavour Tagging in the LHCb experiment*, PoS **LHCP2018** (2018) 230. 7 p.

- [22] LHCb collaboration, R. Aaij *et al.*, *Measurement of the CKM angle γ from a combination of $B^\pm \rightarrow Dh^\pm$ analyses*, Phys. Lett. **B726** (2013) 151 CERN-PH-EP-2013-079, LHCb-PAPER-2013-020, arXiv:1305.2050.
- [23] *New strategies to obtain insights into CP violation through B decays*, vol. 671, Elsevier BV, Nov, (2003). doi: 10.1016/j.nuclphysb.2003.08.010.
- [24] LHCb Collaboration, R. Aaij *et al.*, *Physics case for an LHCb Upgrade II - Opportunities in flavour physics, and beyond, in the HL-LHC era*, arXiv:1808.08865, ISBN 978-92-9083-494-6.
- [25] Wikipedia contributors, *CERN - Wikipedia, the free encyclopedia*, <https://en.wikipedia.org/w/index.php?title=CERN&oldid=996487645>, 2020.
- [26] CERN, *CERN - our history*, <https://home.cern/about/who-we-are/our-history>, (2020).
- [27] CERN, *CERN - our people*, <https://home.cern/about/who-we-are/our-people>, (2020).
- [28] Politechnika Warszawska, *LHC complex*, <http://www.if.pw.edu.pl/~eksperyment/cernemilka/cern/str6.html>.
- [29] L. R. Evans and P. Bryant, *LHC Machine*, JINST **3** (2008) S08001. 164 p.
- [30] L. Rossi, *The LHC superconducting magnets*, Conf. Proc. C **030512** (2003) 141.
- [31] CERN, *Taking a closer look at LHC*, https://www.lhc-closer.es/taking_a_closer_look_at_lhc/1.lhc_parameters.
- [32] A. M. Lombardi, *CERN Linac Upgrade Activities*, Proceedings of LINAC08 **030512** (2008) 353.
- [33] K. Hanke, *Past and present operation of the CERN PS Booster*, Int. J. Mod. Phys. A **28** (2013) 1330019.
- [34] Burnet, J. *et al.*, *Fifty years of the CERN Proton Synchrotron: Volume 1*, 2011. doi: 10.5170/CERN-2011-004.
- [35] *The CERN Super Proton Synchrotron as a tool to study high energy density physics*, vol. 10, 07, (2018). doi: 10.1088/1367-2630/10/7/073028.

-
- [36] J. M. Jowett and M. Schaumann, *Overview of Heavy Ions in LHC Run 2*, in *9th LHC Operations Evian Workshop*, pp. 15–25, 2019.
- [37] O. S. Brüning *et al.*, *LHC Design Report*, tech. rep., Geneva, 2004. doi: 10.5170/CERN-2004-003-V-1.
- [38] A. Piucci, *The LHCb upgrade*, Journal of Physics: Conference Series **878** (2017) 012012.
- [39] S. Dailier, *Cross section of LHC dipole. Dipole LHC: coupe transversale.*, AC Collection. Legacy of AC. Pictures from 1992 to 2002, Apr, 1999.
- [40] LHCb collaboration, *LHCb detector scheme*, <https://lhcb-public.web.cern.ch/en/lhcb-outreach/multimedia/>.
- [41] ATLAS collaboration, *ATLAS detector scheme*, https://physicsmasterclasses.org/exercises/hands-on-cern/hoc_v21en/main_frame/de_atlas1.html.
- [42] CERN, *CMS detector scheme*, <https://home.cern/news/news/experiments/whats-store-cms-detector-over-next-two-years>.
- [43] Wikipedia contributors, *ALICE detector scheme*, https://en.wikipedia.org/wiki/ALICE_experiment.
- [44] ATLAS collaboration, G. Aad *et al.*, *The ATLAS Experiment at the CERN Large Hadron Collider*, JINST **3** (2008) S08003.
- [45] CMS collaboration, S. Chatrchyan *et al.*, *The CMS Experiment at the CERN LHC*, JINST **3** (2008) S08004.
- [46] ALICE collaboration, P. Giubellino, *The ALICE detector at LHC*, vol. 344, 1994. doi: [https://doi.org/10.1016/0168-9002\(94\)90647-5](https://doi.org/10.1016/0168-9002(94)90647-5).
- [47] LHCb Collaboration, Bediaga, I. , *Framework TDR for the LHCb Upgrade: Technical Design Report*, tech. rep., CERN, Geneva, Apr, 2012.
- [48] LHCb collaboration, J. Alves, A. Augusto *et al.*, *The LHCb Detector at the LHC*, JINST **3** (2008) S08005.
- [49] The TOTEM Collaboration, *The TOTEM Experiment at the CERN Large Hadron Collider*, vol. 3, IOP Publishing, Aug, 2008. doi: 10.1088/1748-0221/3/08/s08007.

- [50] Pinfeld, James, *The MoEDAL Experiment at the LHC*, EPJ Web of Conferences **71** (2014) 00111.
- [51] LHCf Collaboration, Adriani, O. *et al.*, *The LHCf detector at the CERN Large Hadron Collider*, aug, 2008. doi: 10.1088/1748-0221/3/08/s08006.
- [52] FASER Collaboration, *FASER: ForwArd Search ExpeRiment at the LHC*, 2019.
- [53] LHCb collaboration, F. Filthaut, *The LHCb Physics Programme*, in *34th Rencontres de Moriond: QCD and Hadronic interactions*, (Hanoi), pp. 409–414, The Gioi, 2001.
- [54] LHCb collaboration, *LHCb VELO (VERtex LOcator): Technical Design Report*, CERN-LHCC-2001-011.
- [55] LHCb collaboration, *LHCb inner tracker: Technical Design Report*, CERN-LHCC-2002-029.
- [56] LHCb collaboration, *LHCb outer tracker: Technical Design Report*, CERN-LHCC-2001-024.
- [57] LHCb collaboration, *LHCb RICH: Technical Design Report*, CERN-LHCC-2000-037.
- [58] LHCb collaboration, *LHCb calorimeters: Technical Design Report*, CERN-LHCC-2000-036.
- [59] LHCb collaboration, *LHCb muon system: Technical Design Report*, CERN-LHCC-2001-010.
- [60] LHCb collaboration, (*LHCb public materials - $b\bar{b}$ production angles*, https://lhcb.web.cern.ch/speakersbureau/html/bb_ProductionAngles.html).
- [61] W. Herr and B. Muratori, *Concept of luminosity*, 2006. doi: 10.5170/CERN-2006-002.361.
- [62] LHCb collaboration, R. Aaij *et al.*, *Precision luminosity measurements at LHCb*, JINST **9** (2014) P12005 LHCb-PAPER-2014-047, CERN-PH-EP-2014-221, arXiv:1410.0149.
- [63] LHCb collaboration, *LHCb public page*, <http://lhcb-public.web.cern.ch/>.

-
- [64] J. J. van Hunen, *The LHCb tracking system*, Nuclear Instruments and Methods in Physics Research Section A: Accelerators, Spectrometers, Detectors and Associated Equipment **572** (2007), no. 1 149, Frontier Detectors for Frontier Physics.
- [65] S. Löchner and M. Schmelling, *The Beetle Reference Manual - chip version 1.3, 1.4 and 1.5*, tech. rep., CERN, Geneva, Nov, 2006.
- [66] C. Parkes *et al.*, *First LHC beam induced tracks reconstructed in the lhcb velo*, Nuclear Instruments and Methods in Physics Research Section A: Accelerators, Spectrometers, Detectors and Associated Equipment **604** (2009), no. 1 1 , PSD8.
- [67] R. Aaij *et al.*, *Performance of the LHCb Vertex Locator*, JINST **9** (2014) P09007, arXiv:1405.7808.
- [68] LHCb collaboration, *LHCb public materials, detectors - trackers*, <https://lhcb-public.web.cern.ch/en/Detector/Trackers2-en.html>.
- [69] J. Andre *et al.*, *Status of the LHCb magnet system*, vol. 12, 04, 2002. doi: 10.1109/TASC.2002.1018421.
- [70] LHCb, *LHCb magnet*, <https://lhcb-magnet.web.cern.ch/>.
- [71] LHCb RICH group, M. Adinolfi *et al.*, *Performance of the LHCb RICH detector at the LHC*, Eur. Phys. J. C **73** (2012) 2431. 25 p, arXiv:1211.6759.
- [72] LHCb collaboration, I. Machikhiliyan, *Current status and performance of the LHCb electromagnetic and hadron calorimeters*, J. Phys. Conf. Ser. **293** (2011) 012052.
- [73] LHCb collaboration, E. Picatoste Olloqui, *LHCb preshower(PS) and scintillating pad detector (SPD): Commissioning, calibration, and monitoring*, J. Phys. Conf. Ser. **160** (2009) 012046.
- [74] A. A. Alves *et al.*, *Performance of the LHCb muon system*, JINST **8** (2013) P02022, arXiv:1211.1346.
- [75] LHCb collaboration, B. Sciascia, *LHCb Run 2 trigger performance*, PoS **BEAUTY2016** (2016) 029.
- [76] R. M. Van der Eijk, *Track reconstruction in the LHCb experiment*, (2002). Presented on 13 Sep (2002).

- [77] W. D. Hulsbergen, *Decay chain fitting with a kalman filter*, Nuclear Instruments and Methods in Physics Research Section A: Accelerators, Spectrometers, Detectors and Associated Equipment **552** (2005) 566.
- [78] F. De Lorenzi, *Parton Distribution Function Studies and a Measurement of Drell-Yan Produced Muon Pairs at LHCb*, 2011. Presented 21 Mar 2011.
- [79] LHCb, *Moore documentantation*, <https://www.physi.uni-heidelberg.de/~mstahl/moore/>.
- [80] LHCb, *Brunel gitlab repository*, <https://gitlab.cern.ch/lhcb/Brunel>.
- [81] LHC collaborations, *The Stripping Project*, <http://lhcbdoc.web.cern.ch/lhcbdoc/stripping/>.
- [82] LHCb, *The LHCb data flow*, <https://lhcb.github.io/starterkit-lessons/first-analysis-steps/dataflow.html>.
- [83] C. Bierlich *et al.*, *A comprehensive guide to the physics and usage of PYTHIA 8.3*, 2022. doi: 10.48550/ARXIV.2203.11601.
- [84] S. Agostinelli *et al.*, *Geant4—a simulation toolkit*, Nuclear Instruments and Methods in Physics Research Section A: Accelerators, Spectrometers, Detectors and Associated Equipment **506** (2003), no. 3 250.
- [85] LHCb collaboration, R. Aaij *et al.*, *Search for the rare decays $B_s^0 \rightarrow \mu^+\mu^-$ and $B^0 \rightarrow \mu^+\mu^-$* , Phys. Lett. B **708** (2012) 55, arXiv:1112.1600.
- [86] LHCb MUON group, N. Bondar, D. Ilin, and O. Maev, *Proposal on application of the multi-wire proportional chambers of the LHCb MUON Detector at very high rates for the future upgrades*, JINST **15** (2020) C07001. 12 p, arXiv:2007.03058.
- [87] R. Quagliani, *Novel real-time alignment and calibration of lhcb detector for Run 2 and tracking for the upgrade.*, Journal of Physics: Conference Series **762** (2016) 012046.
- [88] LHCb collaboration, *LHCb Trigger and Online Technical Design Report*, CERN-LHCC-2014-016.

-
- [89] LHCb collaboration, *LHCb VELO Upgrade Technical Design Report*, CERN-LHCC-2013-021.
- [90] LHCb collaboration, *LHCb Tracker Upgrade Technical Design Report*, CERN-LHCC-2014-001.
- [91] L. Collaboration, *LHCb Tracker Upgrade Technical Design Report*, tech. rep., Feb, (2014).
- [92] C. A. Beteta *et al.*, *The SALT—Readout ASIC for Silicon Strip Sensors of Upstream Tracker in the Upgraded LHCb Experiment*, *Sensors* **22** (2021), no. 1 107.
- [93] LHCb UT, S. Coelli, *Development and test of the CO₂ evaporative cooling system for the LHCb UT Tracker Upgrade*, *JINST* **12** (2017), no. 03 C03087.
- [94] V. A. J. Van Lint, *The physics of radiation damage in particle detectors*, vol. 253, pp. 453–459, 1987. doi: [https://doi.org/10.1016/0168-9002\(87\)90532-8](https://doi.org/10.1016/0168-9002(87)90532-8).
- [95] A. M. Obłąkowska-Mucha, *Radiation damage in the LHCb Vertex Locator : first observation of $B_s^0 \rightarrow D_s^\pm K^{*\mp}$ decay*, JAK, Kraków, (2018).
- [96] E. Fretwurst, G. Lindstrom, I. Pintilie, and J. Stahl, *Radiation damage in silicon detectors caused by hadronic and electromagnetic irradiation*, (2002). doi: 10.48550/arxiv.physics/0211118.
- [97] C. Leroy and P. G. Rancoita, *Particle interaction and displacement damage in silicon devices operated in radiation environments*, *Reports on Progress in Physics* **70** (2007) 493.
- [98] P. Mato, *GAUDI-Architecture design document*, tech. rep., CERN, Geneva, Nov, (1998).
- [99] G. Corti *et al.*, *Software for the LHCb experiment*, *IEEE Trans. Nucl. Sci.* **53** (2006) 1323.
- [100] S. Roiser and C. B. and, *The LHCb software and computing upgrade towards LHC Run 3*, *Journal of Physics: Conference Series* **1085** (2018) 032049.
- [101] S. Roiser, *Event Data Modelling for the LHCb Experiment at CERN*, (2003). Presented on 30 Sep 2003.

- [102] T. Szumlak, *Calibration software platform for LHCb upgrade silicon detectors: STORCK and TITANIA*, tech. rep., CERN, Geneva, Jul, (2021).
- [103] T. Szumlak and C. Parkes, *Description of the Vetra Project and its Application for the VELO Detector*, tech. rep., CERN, Geneva, May, (2008).
- [104] F. Legger, A. Bay, G. Haefeli, and L. Locatelli, *TELL1: development of a common readout board for LHCb. TELL1. a common readout board for LHCb*, tech. rep., CERN, Geneva, Nov, 2004. doi: 10.1016/j.nima.2004.07.282.
- [105] Alessio, F and Jacobsson, R and Guzik, Z, *A 40 MHz Trigger-free Readout Architecture for the LHCb Experiment*, (2009). doi: 10.5170/CERN-2009-006.514.
- [106] P. Moreira *et al.*, *The GBTX Project*, (2009). doi: 10.5170/CERN-2009-006.342.
- [107] LHCb, *Vetra - gitlab repository*, <https://gitlab.cern.ch/lhcb/Vetra>, (2022).
- [108] M. Adinolfi *et al.*, *LHCb data quality monitoring*, J. Phys. : Conf. Ser. **898** (2017) 092027. 5 p.
- [109] LHCb, *Brunel gitlab repository*, <https://lbwebmonet.cern.ch/>. Access restricted for CERN users.
- [110] LHCb collaboration, *PyQt5*, <https://pypi.org/project/PyQt5/>.
- [111] EDUCBA, *XML file format*, <https://www.educba.com/xml-file-format/>.
- [112] I. Antcheva *et al.*, *ROOT — A C++ framework for petabyte data storage, statistical analysis and visualization*, Computer Physics Communications **180** (2009), no. 12 2499, 40 YEARS OF CPC: A celebratory issue focused on quality software for high performance, grid and novel computing architectures.
- [113] LHCb collaboration, R. Aaij *et al.*, *Measurement of CP asymmetry in $B_s^0 \rightarrow D_s^\mp K^\pm$ decays*, JHEP **03** (2018) 059 LHCb-PAPER-2017-047, CERN-EP-2017-315, arXiv:1712.07428.
- [114] LHCb collaboration, R. Aaij *et al.*, *Measurement of CP violation in $B^0 \rightarrow D^\pm \pi^\mp$ decays*, JHEP **06** (2018) 084 LHCb-PAPER-2018-009, CERN-EP-2018-084, arXiv:1805.03448.

-
- [115] LHCb Collaboration, R. Aaij *et al.*, *Measurement of the CKM angle γ in $B^\pm \rightarrow DK^\pm$ and $B^\pm \rightarrow D\pi^\pm$ decays with $D \rightarrow K_S^0 h^\pm h^\mp$* , Geneva, Aug, (2020).
- [116] LHCb, *The LHCb facts*, <https://twiki.cern.ch/twiki/bin/view/Main/LHCb-Facts>.
- [117] M. Clemencic *et al.*, *The LHCb simulation application, gauss: Design, evolution and experience*, Journal of Physics: Conference Series **331** (2011) 032023.
- [118] LHC collaborations, *The GAUSS Project*, <http://lhcbdoc.web.cern.ch/lhcbdoc/ gauss/>.
- [119] S. Tolk, J. Albrecht, F. Dettori, and A. Pellegrino, *Data driven trigger efficiency determination at LHCb*, tech. rep., CERN, Geneva, May, 2014.
- [120] LHCb, *Loki's particle functions*, <https://twiki.cern.ch/twiki/bin/view/LHCb/LoKiParticleFunctions>.
- [121] B. Mehlig, *Machine Learning with Neural Networks*, Cambridge University Press, oct, 2021. doi: 10.1017/9781108860604.
- [122] H. Drucker and C. Cortes, *Boosting decision trees.*, vol. 8, pp. 479–485, 01, (1995).
- [123] T. Chen and C. Guestrin, *XGBoost*, in *Proceedings of the 22nd ACM SIGKDD International Conference on Knowledge Discovery and Data Mining*, ACM, aug, 2016. doi: 10.1145/2939672.2939785.
- [124] BaBar, B. Aubert *et al.*, *Measurement of the Branching Fractions of the Rare Decays $B^0 \rightarrow D_s^{(*)+} \pi^-$, $B^0 \rightarrow D_s^{(*)+} \rho^-$, and $B^0 \rightarrow D_s^{(*)-} K^{(*)+}$* , Phys. Rev. D **78** (2008) 032005, arXiv:0803.4296.
- [125] BaBar collaboration, B. Aubert *et al.*, *Study of $B \rightarrow D^{(*)} D^{(*)}$ decays and measurement of D_s^- and $D_{sJ}(2460)$ branching Fractions*, Phys. Rev. D **74** (2006) 031103, arXiv:hep-ex/0605036.
- [126] LHCb collaboration, R. Aaij *et al.*, *First observation and measurement of the branching fraction for the decay $B_s^0 \rightarrow D_s^{*\mp} K^\pm$* , JHEP **06** (2015) 130, arXiv:1503.09086.
- [127] L. Anderlini *et al.*, *Computing strategy for PID calibration samples for LHCb Run 2*, tech. rep., CERN, Geneva, Jul, (2016).

- [128] LHCb Collaboration, R. Aaij *et al.*, *Measurement of the CKM angle γ and B_s^0 - \bar{B}_s^0 mixing frequency with $B_s^0 \rightarrow D_s^\mp h^\pm \pi^\pm \pi^\mp$ decays*, JHEP **03** (2021) 137, [arXiv:2011.12041](#).
- [129] R. Aaij *et al.*, *Measurement of CP asymmetry in $B_s^0 \rightarrow D_s^\mp K^\pm$ decays*, no. 3, Springer Science and Business Media LLC, mar, 2018. doi: 10.1007/jhep03(2018)059.
- [130] R. Aaij *et al.*, *Measurement of CP violation in $B^0 \rightarrow D^\mp \pi^\pm$ decays*, vol. 2018, Springer Science and Business Media LLC, jun, 2018. doi: 10.1007/jhep06(2018)084.
- [131] K. Pothuganti, *Overview on principal component analysis algorithm in machine learning*, international research journal of science and technology (2020) 2582.
- [132] D. P. Kingma and M. Welling, *An introduction to variational autoencoders*, Foundations and Trends in Machine Learning **12** (2019), no. 4 307.